

https://dspace.org/

Structural and computational studies on the nature of Au (iii) ...Q interactions

Speirs, Daniel J

2018
https://hdl.handle.net/10539/27310

Downloaded from a DSpace repository. https://dspace.org/

Structural and Computational Studies on the Nature of Au(III)···Q Interactions

Submitted in the fulfilment of the requirements for the degree of

Master of Science

By

Daniel J. Speirs

BSc(Honours)(University of the Witwatersrand)



WITS
UNIVERSITY

February 2018

School of Chemistry

University of the Witwatersrand

Johannesburg

Declaration

I declare that this Dissertation is my own, unaided work. It is being submitted for the Degree of Master of Science at the University of the Witwatersrand, Johannesburg. It has not been submitted before for any degree or examination at any other University.

This Dissertation does not contain other persons' data, pictures, graphs or other information, unless specifically acknowledged as being sourced from other persons.

This Dissertation does not contain other persons' writing, unless specifically acknowledged as being sourced from other researchers. Where other written sources have been quoted, then:

a) Their words have been re-written but the general information attributed to them has been referenced.

b) Where their exact words have been used, then their writing has been placed in italics and inside quotation marks, and referenced.

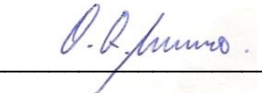
This Dissertation does not contain text, graphics or tables copied and pasted from the Internet, unless specifically acknowledged, and the source being detailed in the Dissertation and in the References section(s).

Signed: 

Daniel J. Speirs

On this __**11th**___day of __**June**___ 20__**18**__in__**The University of the Witwatersrand**__

I hereby certify that this is correct.

Signed: 

Prof. Ordé Q. Munro

(Supervisor)

Acknowledgements

This work is based on research supported by the South African Research Chairs Initiative of the Department of Science and Technology and National Research Foundation of South Africa (Grant No 64799). I would like to thank Dr. Cathryn Slabber, Mark Blow, Monika Nowakowska, Welni Duminy and Delbert Botes for their assistance with lab work. I would like to thank my supervisor Prof. Orde Munro, for his assistance and guidance on this project. He has helped me a huge amount and he has my sincerest gratitude. I would also like to thank Prof. Manuel Fernandes for his assistance with crystallography – get well soon.

Dedication

I would like to dedicate this dissertation to the people who I love. To my parents, I will always be in debt to both of you. Your support has been unwavering and I will always be grateful for what you have given me and I will do my best to pass it along. To my sister Kate, thank you for always being around and playing the role of the big sister so well. To my girlfriend Sammi, thank you for all the love and support you have given me during this stressful time in my life.

Abbreviations and Notes

ACN	Acetonitrile
AIM	Atoms in molecules (type of computational analysis)
AIMAII	Software package used to perform atoms in molecules analysis
BCP	Bond critical point
BO	Born-Oppenheimer (approximation)
Cisplatin	Diamminedichloroplatinum(II)
CSD	Cambridge structural database
DFT	Density functional theory
DNA	Deoxyribonucleic acid
FTIR	Fourier transform infrared
H-K	Hohenberg–Kohn (equation)
HOMO	Highest occupied molecular orbital
K-S	Kohn-Sham (equation)
LUMO	Lowest unoccupied molecular orbital
NBO	Natural bond orbital
NMR	Nuclear magnetic resonance (spectroscopy)
PES	Potential energy surface
SARC	Segmented all-electron relativistically contracted
Top1/Top2	Topoisomerase I/II (enzyme)
VCD	Vibrational circular dichroism
XRD	X-ray diffraction
ZORA	Zeroth-order regular approximation

Notes:

1. For crystal structures (unless otherwise stated), atom colours reflect the following elements: grey, C; blue, N; white, H; red, O.

Abstract

Pincer ligands derived from the reaction of one mole equivalent of pyridine-2,6-dicarbonyl dichloride with 2 moles of 2,4,6-trimethylaniline or cyclohexanamine were synthesized and characterized by ^{1}H NMR, ^{13}C NMR, FTIR, high resolution MS, UV-visible spectroscopy and single crystal X-ray diffraction. A dynamic NMR analysis was performed on the novel bis(cyclohexylamide) derivative to delineate its conformational preferences and to demonstrate that this class of ligands is pre-organized for metal ion chelation. Pd(II) and Au(III) derivatives of the bis(mesitylamide) ligand system were then synthesized and reacted with quinoline as a co-ligand, which gave four-coordinate derivatives with the quinoline bound to the metal ion within the pocket of the pincer chelate. These novel metal chelates were characterized by ^{1}H NMR, ^{13}C NMR, FTIR, high resolution MS, UV-visible spectroscopy and single crystal X-ray diffraction.

The Au(III), Pt(II), and Pd(II) chelates of the pincer ligands were used as experimental and *in silico* receptors for the binding of quinoline co-ligands bearing a range of substituent atoms at ring-position 8. This permitted investigation of the near-axial nonbonded interaction of the substituent atom at ring-position 8 with the metal ion. Density functional theory (DFT) calculations and atoms in molecules (AIM) analyses were performed on both the metal-free ligands and on a series of theoretical, quinoline-containing chelates of Pd(II), Pt(II), and Au(III). The atom at ring-position 8 on the quinoline (the Q atom) was systematically varied (H, F, Cl, Br, I) to delineate the electronic properties of the M···Q axial interaction. The DFT basis sets used were SDD, DGDZVP, 6-311G(d,p), and SARC-ZORA in conjunction with the HSEH1PBE functional. The computational analysis suggested that *partially* 5-coordinate Au(III) species can, in principle, form in a suitably constrained system such as that designed herein. A partial, axial dative covalent bond with substantial ionic character may be formed with Au(III) because electron density is forced from the p- and s-orbitals of the interacting atom (Q) into the vacant $6p_z$ atomic orbital of the Au(III) ion. This study therefore challenges the long-held notion that Au(III) complexes will always be square planar.

List of Figures

Figure	Caption	Page
Figure 1.1	A diagram from a paper by Akerman *et al*. 2014 showing that cytotoxic Au(III) macrocycles act as catalytic inhibitors of human topoisomerase I (Top 1). This study showed that this mechanism of action may be traced to the existence of a crucial Au(III)---O=C interaction with the carbonyl group of thymine in the TA base pair targeted by the metallodrug.	**4**
Figure 1.2	Diagram of a Au(III) corrole, synthesized by Teo *et al*. This complex exhibiteds high cytotoxicity towards cisplatin-resistant cancer cells. In this case M = Au(III), but other suitable metals include: Fe, Mn, Al and Ga.	**4**
Figure 1.3	Diagram showing the structures of the Au(I) drugs Auranofin and $[Au(CN)_2]^-$.	**6**
Figure 1.4	Example of an output of an Atoms in molecules (AIM) analysis (performed using the AIMAII software package). The bond critical points have been rendered as green spheres. Solid lines indicate formal bonding, while the dotted lines denote an electrostatic interaction. The number adjacent to the bond critical points are the Laplacian to the electron density ($\nabla^2\rho$). However this is just one of the many bond critical point properties that were calculated during the analysis; significantly, the $\nabla^2\rho$ and the electron density (ρ) values are most relevant to this work.	**11**
Figure 1.5	a) Synthesis done by (Johnson *et al.* 2014). In This Work, the dipp group was substituted with phenyl, mesityl, and cyclohexyl groups. b) An example of a proposed synthesis (**Chapter 4**) that was based on the synthesis done in the literature method outlined in a).	**14**
Figure 1.6	a) Synthesis done by (Shimada *et al.* 2004). In this work aniline was used instead of N-methylaniline. b) The proposed synthesis for ligands in this dissertation. The synthesis was based on that of shown in a), as expounded in Chapter 3.	**15**
Figure 1.7	Diagram showing: (a) a generalised example of the Au(III)···Q interaction, where Q axially interacts with Au(III). (b) Specific illustration of a stabilizing Au(III)···O=C interaction.	**16**
Figure 3.1	Thermal ellipsoid plots (50% probability surfaces) for the low-temperature X-ray structures of 1 and 2. The atom numbering schemes are included. The structure of 2 comprises two independent molecules in the asymmetric unit (ASU); these are shown separately as 2a and 2b. Hydrogen atoms have been rendered as spheres of arbitrary radius.	**31**
Figure 3.2	Diagram highlighting how intermolecular non-bonded contacts impact the dihedral angles of the mesityl rings in structure **1**.	**32**
Figure 3.3	Packing diagram showing the intermolecular interactions between molecules of a dimer of **2**. Hydrogen bonds have been shown green.	**33**

	The distance of the $O_{(carbonyl)}\cdots N_{(amide)}$ interaction alternates between 2.229 Å to 2.231 Å with each subsequent addition to the one-dimensionally bonded sequence.	
Figure 3.4	A comparison between the DFT-calculated (yellow) and the X-ray crystal structure (blue) of compounds **1** and **2**. The crystallographically-independent molecules of **2** are shown separately as **2a** and **2b**. Hydrogen atoms excluded for visibility. SI values: **1:** 95.24 % **2a**: 91.61 % **2b**: 91.84 %	**34**
Figure 3.5	MOGUL search of the CSD (up to May 2017) mapping the range of N=C–C=O torsion angles (highlighted in green) in crystallographically characterized bis(amide)-pyridine pincer derivatives. Out of 3721 structures, only 6 have the highlighted torsion angle < 30°. The typical range is 140–180°, with the majority of structures exhibiting a torsion angle between 170–180°. The histogram has been constructed with a 5° bin width.	**36**
Figure 3.6	One of the independent molecules in the X-ray structure of MILHEV in which an *exo*|*exo* conformation for the bis(amide) system is stabilized by the two amide carbonyl oxygen atoms serving as H-bond acceptors to a water molecule.	**37**
Figure 3.7	Crystal structures of EQANOB and FEKYIE. These are examples of coordination complexes which exhibit an *exo*|*exo* conformation (with respect to amide group).	**38**
Figure 3.8	Crystal structures of ALOYIL and KERWIO. These are examples of literature pincer ligands, whose structure parameters closely match those of **1** and **2**.	**39**
Figure 3.9	(a) DFT-calculated molecular orbital diagram for compound **1**. The HOMO-LUMO gap is 3.70 eV. (b) DFT-calculated molecular orbital diagram for compound **2**. The HOMO-LUMO gap is 4.59 eV.	**41**
Figure 3.10	a) Three-dimensional plot showing the variation in the relative heat of formation, ΔE, of **1** as a function of the torsion angles ϕ1 and ϕ2. The angular coordinates locating the crystal structure are shown as a yellow sphere (ϕ1 = −91.8°, ϕ2 = −104.9°, ΔE = 8.8 kJ/mol).	**43**
Figure 3.11	a) Three-dimensional plot showing the variation in the relative heat of formation, ΔE, of **2** as a function of the torsion angles ϕ1 and ϕ2. The angular coordinates locating the crystal structure are shown as a yellow sphere (ϕ1 = 42.9°, ϕ2 = 40.1°, ΔE = 0.1 kJ/mol).	**43**
Figure 3.12	a) Three-dimensional plot showing the variation in the relative heat of formation, ΔE, of **1** as a function of the torsion angles ϕ1 and ϕ2. The angular coordinates locating the crystal structure are shown as a yellow sphere (ϕ1 = -178.0°, ϕ2 = 173.0°, ΔE = -0.8 kJ/mol).	**46**
Figure 3.13	a) Three-dimensional plot showing the variation in the relative heat of formation, ΔE, of **2** as a function of the torsion angles ϕ1 and ϕ2. The angular coordinates locating the crystal structure are shown as a yellow sphere (ϕ1 = 170.6°, ϕ2 = -171.2°, ΔE = 1.7 kJ/mol).	**46**
Figure 3.14	Crystal structures of TOYREG, TOYQUV and SOPCEH. TOYREG and TOYQUV are Ni(II) chelates of **1** and SOPCEH is a Au(III) chelate of **1**. The locations of the conformations of these structures on the surfaces shown in Figures 3.10 and 3.11 are indicated.	**49**
Figure 3.15	Conformational comparison between the global energy minimum conformer E (Scan 1, Figure 3.10), and the crystal structure of **1**, and the Conformational comparison between the global energy minimum conformer B (Scan 1, Figure 3.11) and the crystal structure of **2**.	**49**
Figure 3.16	a) Three-dimensional plot showing the variation in the relative heat of formation, ΔE, of **1** as a function of the torsion angles ϕ1 and ϕ2. The	**51**

	angular coordinates locating the crystal structure are shown as a yellow sphere (ϕ1 = -83.7°, ϕ2 = -86.4°, ΔE = -0.8 kJ/mol).	
Figure 3.17	Variable temperature ^{1}H NMR spectra, taken at a constant concentration of 0.0228 M. The plot shows the downfield shift of the N-Hamide peak. The temperature range for the experiment was 298.15 K to 388.15 K, with spectra recorded at 10 K intervals.	**53**
Figure 3.18	Variable concentration ^{1}H NMR spectra, taken at a constant temperature of 293.15 K. The plot shows the downfield shift of the N-H amide peak with increasing concentration.	**53**
Figure 3.19	Plots of temperature vs ^{3}J(HCNH), linewide and shift value for the variable temperature ^{1}H NMR experiment. This study was performed at a constant concentration of 0.0228 M.	**53**
Figure 3.20	Variable temperature 1H NMR spectra, taken at a constant concentration of 0.0228 M. The temperature range for the experiment was 288.15 K to 213.15 K, with spectra recorded at -10 K intervals. The plot shows the downfield shift of the N-Hamide peak.	**54**
Figure 3.21	Variable temperature ^{1}H NMR spectra, taken at a constant concentration of 0.0228 M. This is a stacked view of the data presented in previous Figure 3.20. The temperature range for the experiment was 288.15 K to 213.15 K, with spectra recorded at -10 K intervals. The plot shows the downfield shift of the N-Hamide peak. N-H peaks have been labelled (i) to (viii).	**54**
Figure 3.22	Low energy DFT calculated structure of **2**. At the slow exchange limit (213.15 K) this is likely the only conformer that will be adopted by the system.	**56**

Figure 4.1	Diagram showing (a) a generalised example of the Au(III)···Q interaction, where Q axially interacts with Au(III), and (b) the stabilizing Au(III)···O=C interaction.	**63**
Figure 4.2	Diagram showing examples of structures obtained from the CSD, where the Au(III) ion is associated with non-coordinating, electron-rich groups. Hydrogen atoms have been omitted for visibility. Crystal structures of DODXID (i), NURYAB (ii), TEMMED (iii), and TUBBOH (iv) are shown.	**64**
Figure 4.3	Diagram showing an example of the Au(III)···Q interaction that would occur in our proposed metal-quinoline system.	**65**
Figure 4.4	Thermal ellipsoid plot (30% probability surfaces) of the [Au(L1)(Quinoline)][PF_6]·(CH_3CN) crystal structure showing selected atom labels from the crystallographic numbering scheme. Hydrogen atoms have been rendered as spheres of arbitrary radius.	**69**
Figure 4.5	Diagram illustrating the least-squares planes between the metal-chelating 11-atom pincer ligand and the 10-atom quinoline ligand plane. The dihedral angle between the planes is 84.7°. The Au(III) ion and three N atoms of the pincer ligand lie approximately in the chelate plane (Au is displaced only 0.04 Å below the plane), while the quinoline N atom is displaced significantly below the plane (0.36 Å) giving it the appearance of a downward tilt.	**70**
Figure 4.6	Partly labelled diagram illustrating the packing between two [Au(L1)(Quinoline)]$^{+}$ cations. The quinoline ligand of the left structure [symmetry code: *x*, *y*, *z*] is π-stacked with the mesityl ring of the neighbouring molecule [symmetry code: –0.5+*x*, 0.5–*y*, *z*] in the lattice. Ring centroids are illustrated as coloured spheres; distances between selected centroids are in Å. H atoms have been omitted for	**72**

	clarity.	
Figure 4.7	Thermal ellipsoid plot (25% probability surfaces, 296 K) of the Pd(L1)(Quinoline) crystal structure showing selected atom labels from the crystallographic numbering scheme. Hydrogen atoms have been rendered as spheres of arbitrary radius. Solvent (acetonitrile) is associated with the structure, but due to disorder and diffuse electron density was omitted using solvent masking in OLEX2. Two voids (each corresponding to 967.6 $Å^3$; 368.6 electrons) exist in the asymmetric unit at (0.000, 0.000, –0.986) and (0.500, 0.500, –0.402).	**74**
Figure 4.8	Diagram illustrating the least-squares planes between the metal-chelating 11-atom pincer ligand and the 10-atom quinoline ligand plane for Pd(L1)(Quinoline). The dihedral angle between the planes is 68.5°. The Pd(II) ion and three N atoms of the pincer ligand lie approximately in the chelate plane (Pd is displaced only 0.08 Å below the plane), while the quinoline N atom is displaced significantly below the plane (0.41 Å) giving it the appearance of a downward tilt. H atoms have been omitted for clarity.	**76**
Figure 4.9	Diagram summarising the structures that were investigated, and the simplified naming convention that will be used throughout this dissertation.	**80**
Figure 4.10a	A comparison between the DFT-calculated (yellow) and X-ray crystal structure (blue) of $[Au(L1)(8\text{-H-Quin})]^+$. The DFT calculation was performed at the HSEH1PBE/SARC-ZORA/ 6-311G(d,p) level of theory. For the DFT calculation the SARC-ZORA basis set was used for the metal (Au) and the 6-311G(d,p) basis set was used for light atoms (H, C, N, O). SI: 85.96%. Hydrogen atoms have been excluded for visibility.	**81**
Figure 4.10b	A comparison between the DFT-calculated (yellow) and X-ray crystal structure (blue) of Pd(L1)(8-H-Quin). The DFT calculation was performed at the HSEH1PBE/SARC-ZORA/ 6-311G(d,p) level of theory. For the DFT calculation the SARC-ZORA basis set was used for the metal (Pd) and the 6-311G(d,p) basis set was used for light atoms (H, C, N, O). SI: 97.50%. Hydrogen atoms have been excluded for visibility.	**81**
Figure 4.11	Diagram showing the energy profile of quinoline rotamers for $[Au(L1)(8\text{-H-Quin})]^+$, $[Au(L2)(8\text{-H-Quin})]^+$, $[Au(Phenyl)(8\text{-H-Quin})]^+$. The relative energy (kJ mol^{-1}) of the conformer has been plotted against the quinoline ligand's torsion angle (°), *d* (see Figure 4.12 for torsion angle *d*). Torsion angles: (i), 94.13°; (ii), 204.13°; (iii), –12.68°; (iv), 47.32°; (v), 97.32°; (vi), 4.63°; (vii), 54.63°; (viii), 114.63°. Note conformers or rotamers (viii)′ and (iv)′ are slightly higher energy structures, but can essentially be seen as being degenerate to conformers (viii) and (iv), respectivley.	**83**
Figure 4.12	Diagram defining the main structural features that were systematically analysed for a series of Au(III) pincer complexes. The structure of $[Au(L2)(Quin)]^+$ has been used for illustration: (a) M···Q distance, *l*; (b) $M—N_{(Quin)}$ distance; (c) Inter-centroid distance; (d) Torsion angle defining the orientation of the quinoline ligand, *d.* The electron density at the bond critical point along *a*, ρ(M···Q), was obtained from AIMAII analysis of the final DFT-calculated geometry and electron density of the system; the location of the bond critical point (BCP) was structure-dependent.	**85**
Figure 4.13	A diagram showing a graphical representation of the volume of sphere overlap, β, which was calculated according to Weisstein. $\beta =$	**86**

	$\frac{\pi(X+Y-l)^2(l^2+2lY-3Y^2+2lX+6XY-3X^2)}{12l}$, where β is the overlap volume of two spheres of radii X (van der Waals radius of M) and Y (van der Waals radius of Q). *l* is the distance between the atom centers (i.e., the M···Q distance).	
Figure 4.14	Plots of selected data from Table 4.7. These plots are discussed further in Section 4.3.5.1.	**92**
Figure 4.15	AIMAII output of the calculated structure of $[Au(L2)(8\text{-H-Quin})]^+$. The green dots are bond critical points and the number adjacent to the dots is the ρ value (electron density) at that point. In this case, the ρ(M···Q) (where Q = H) value is 0.0121 au.	**94**
Figure 4.16	Diagram illustrating the orbital overlap present in the $[Au(Lx)(8\text{-H-Quin})]^+$ structure. As the degree of orbital overlap increases, the electron occupancy of the $6p_z$ orbital increases. Since the $6p_z$ orbital is vacant, the interaction is of the donor–acceptor type.	**95**
Figure 4.17	Diagram emphasising how M—$N_{(quin)}$ increases as M···Q increases. $N_{(pyridyl)}$—Au—$N_{(quinoline)}$ = 177.80° and $N_{(pyridyl)}$—Au—$N_{(8\text{-iodo-quinoline)}}$ = 164.62°. Some hydrogen atoms have been excluded for visibility.	**96**
Figure 4.18	Diagram showing the structural differences between 5-coordinate Au(III) structures in the literature (CDMPAU) and a Au(III) structure that was ananalysed as part of this study. Hydrogen atoms have been excluded for visibility. The ρ(Au···F) value for $[Au(L2)(8\text{-F-Quin})]^+$ is 0.202 au and the ρ(Au-N) value is 0.371 au.	**97**
Figure 4.19	An annotated graph of the relationship between the β and ρ(Au···Q) parameters.	**99**
Figure 4.20	Diagram showing the variation in the orientation of the quinoline substituent. This has been quantified by examining torsion angle *d* for the conformers of the Au(L1) and Au(L2) series. Similar quinoline orientation trends are seen for the Pd(II) and Pt(II) congeners. For Parts b) and d), the quinoline group has been displayed as wire for visibility. All hydrogen atoms have been omitted for visibility, with the exception of hydrogen atoms that interact with the metal. Note that when torsion angle *d* = 90°, the plane of the quinoline will be orthogonal to the AuN_4 square plane.	**100**
Figure 4.21	Image showing the output of an electron density analysis (AIM method; AIMAII software package) for $[Au(Phen)(8\text{-[OMe]-Quin})]^+$. The green dots denote selected bond critical points while the number (in atomic units, au) gives a measure of the predicted electron density of the bond or interaction.	**102**
Figure 4.22	Selected examples from the literature of nominally 5-coordinate Au(III), Pt(II) and Pd(II) crystal structures. Hydrogen atoms have been excluded for visibility. The key question here is whether the axial M—N interaction behaves merely as an electrostatic interaction enforced by geometrical constraints of the phenanthroline ligand, or if sufficient electron density resides at a bond critical point for the interaction to be treated as a dative covalent bond. Structures are re-drawn from CSD codes: CNPLPT, CDMPAU, and DAPZIF.	**103**
Figure 4.23	Examples of the output of AIM analysis on structures a) $[Au(L2)(8\text{-H-Quin})]^+$ and b) $[Au(L2)(8\text{-Cl-Quin})]^+$. Bond critical points are rendered as green spheres, with ρ data labels displayed over selected bond critical points.	**103**
Figure 4.24	Example of the output of an AIM analysis on the $[Au(L2)(8\text{-I-Quin})]^+$ structure. Bond critical points are rendered as green spheres, with $\nabla^2\rho$	**107**

	data labels displayed over selected bond critical points. All of the $\nabla^2\rho$ values are positive, showing that the bonds are ionic in nature.	
Figure 4.25	Diagram illustrating the nature of the side-on M···Br interaction in the $Au(Lx)(8\text{-}Br\text{-}Quin)]^+$ structure. Electron density is transferred from the diffuse 4s orbital of Br into the $6p_z$ orbital of Au(III).	**108**
Figure 4.26	Diagram illustrating the ionic Au···N interaction that is present in the CDMPAU structure. The 1,10-phenanthroline nitrogen is positioned so that the lone pair on the nitrogen is orientated into the $6p_z$ orbital of Au(III).	**109**
Figure 4.27	(a) Overlay of the DFT-calculated and crystal structure of CDMPAU. SI: 96.43%. Hydrogen atoms have been excluded for visibility. (b) DFT-calculated structure of CDMPAU with selected results of the AIM analysis. Selected bond critical points have been shown as green dots and their corresponding ρ values have been provided in Table 4.9.	**110**
Figure 5.1	**Figure 5.1.** Diagram showing the compounds that have been synthesised during this dissertation. (a) *N,N'*-bis(2,4,6-trimethylphenyl)-2,6-pyridinecarboxamidato(quinoline)Au(III), (b) *N,N'*-bis(2,4,6-trimethylphenyl)-2,6-pyridinecarboxamidato(quinoline)palladium(II), (c) *N*,*N*'-Bis(2,4,6-trimethylphenyl)-2,6-pyridinedicarboxamide (H_2L1) and (d) *N*,*N*'-Bis(cyclohexyl)-2,6-pyridinedicarboxamide (H_2L2).	**116**

List of Schemes

Scheme	Title	Page
Scheme 3.1.	Structures of *N*,*N*'-bis(2,4,6-trimethylphenyl)-2,6-pyridinedicarboxamide (**1**) and *N*,*N*'-bis(cyclohexyl)-2,6-pyridinedicarboxamide (**2**). Linkage isomers **I** to **III** result from rotations about ϕ1 and ϕ2 and resonance re-hybridization of the amide groups of the ligand. Linkage isomers are drawn for an arbitrary metal ion M with square planar geometry and a fourth ligand L.	**30**
Scheme 3.2.	Clarification of N-H hydrogen orientations and structures that were given as inputs for the CSD search.	**35**
Scheme 4.1.	The output of an AIM analysis performed on the BORSUY structure. Bond critical points are rendered as green spheres, with ρ data labels displayed over selected bond critical points. It was from this analysis that the ρ(M-O) values used in tables 4.9-4.11 were obtained.	**109**

List of Tables

Table	Title	Page
Table 3.1	Selected results of the search that was conducted; the input structure used in the search has been shown in Scheme 3.2.	**35**
Table 3.2	Outlier structures that were found during the the search of the CSD. These outliers exhibit exo|exo or exo|endo conformations, and their torsion angles have been listed.	**37**
Table 3.3	Selected bond lengths, bond angles and torsions angles for various	**39**

	structures of interest.	
Table 3.4	A series of metal cations, and their predicted ligand binding preferences. Absolute hardness values are according to Pearson.	**42**
Table 3.5	Structural details and parameters of the conformers shown in **Figure 3.10:**	**44**
Table 3.6	Structural details and parameters of the literature conformations shown in **Figure 3.10.**	**45**
Table 3.7	Structural details and parameters of the conformers shown in **Figure 3.11:**	**45**
Table 3.8	Structural details and parameters of the conformers shown in **3.12**	**47**
Table 3.9	Structural details and parameters of the literature conformations shown in Figure **3.13**	**47**
Table 3.10	Structural details and parameters of the conformers shown in **Figure 3.14**	**48**
Table 3.11	Structural details and parameters of the conformers shown in **3.15**	**50**

Table 4.1	Selected AuN_4-type structures that were found in the CSD. The identity of the axially interacting atom, and its distance from the Au(III) metal centre, have been included in the table.	**67**
Table 4.2	Selected Au/Pd/Pt-N_2Cl_3-type structures that were found in the CSD. The identity of the metal, the axially interacting atom, the M···Q distance and the interaction type have been included in the table.	**68**
Table 4.3	Selected geometrical and conformational parameters for the structure of [Au(L1)(Quinoline)][PF_6]·(CH_3CN).	**72**
Table 4.4	Selected metrical parameters for the X-ray structure of Pd(L1)(Quinoline).	**75**
Table 4.5	A list of the structures on which DFT and AIM analysis was performed. See Figure 4.9 for details on the naming convention used for the compounds.	**79**
T**able 4.6**	Observed correlation coefficients, R^2, for the monoatomic halide series of Au(III), Pt(II), and Pd(II) chelates of deprotonated ligands H_2L1 and H_2L2. Correlations were derived using the correlation function found in Excel's data analysis ToolPak plugin. Refer to Figures 4.11 and 4.12 for a graphical explanation of the structural features that were probed during the analysis.	**88**
Table 4.7	Selected DFT–calculated structural and electronic data (quinolines substituted by a single atom). M···R atomic overlaps (van der Waals radii) determined via trigonometric methods are included.	**90**
Table 4.8	Table of parameters for the halide series atoms and hydrogen.	**91**
Table 4.9	Selected electronic parameters for the monoatomic compound series (Au(III) complexes) that were obtained from AIMAII analysis of the DFT-calculated electron density. Two sample structures from the series have been given in Figure 4.22.	**104**
Table 4.10	Selected electronic parameters for the monoatomic compound series (Pd^{2+} complexes) that were obtained from AIMAII analysis of the DFT-calculated electron density.	**104**
Table 4.11	Selected electronic parameters for the monoatomic compound series (Pt^{2+} complexes) that were obtained from AIMAII analysis of the DFT-calculated electron density.	**105**
Table 4.12	Table showing the Laplacian of the electron density ($\nabla^2\rho$) at the bond critical point of the M···Q interaction for each of the molecules in the	**106**

	monoatomic compound series.	
Table 4.13	Comparison of bond lengths of the crystal vs the DFT-calculated structure of CDMPAU. Information on the key bond critical points is also provided in the table.	**110**

Contents

Declaration

Acknowledgements

Dedication

Abbreviations and Notes

Abstract

List of Figures

List of Schemes

List of Tables

Chapter 1: Introduction	
1.1 Dissertation Outline	**1**
1.2 Introduction	**2**
1.2.1 Introduction and background of Au(III) complexes	**2**
1.2.1.1 Au(III) catalysts and materials	**2**
1.2.1.2 Au(I) and Au(III) metallodrugs	**2**
1.3 Computational chemistry	**6**
1.3.1 Quantum mechanics in computational chemistry	**6**
1.3.2 Introduction and history of the computational methods used	**9**
1.3.2.1 Density functional theory	**9**
1.3.2.2 Atoms in molecules analysis	**10**
1.4 Project Aims	**13**
1.4.1 Problem statement	**13**
1.4.2 Purpose of the study	**13**
1.4.2.1 Synthetic	**13**
1.4.2.2 Computational and research based goals	**15**
1.5 References and notes	**17**

Chapter 2: Experimental Methods

2.1 Materials **19**

2.2 Synthesis of compounds **19**

2.2.1 Pyridine-bis(amide) pincer ligands **19**

2.2.2 Metal chelates of pincer ligands **21**

2.3 Single-crystal X-ray diffraction **23**

2.4 UV-Visible spectroscopy **23**

2.5 Fourier-transform infrared spectroscopy **24**

2.6 High resolution mass spectroscopy **24**

2.7 ^{1}H and ^{13}C NMR **24**

2.8 Gaussian09W and Gaussview **24**

2.8.1 Chapter 3 DFT calculations **25**

2.8.2 Chapter 4 DFT calculations **25**

2.9 AIM analysis **25**

2.10 NBO 3.1 **26**

2.11 Biovia Discovery Studio and Mercury **26**

2.12 CSD and ConQuest **26**

2.13 References and Notes **26**

Chapter 3: Structural, Spectroscopic, and DFT Studies on Tridentate Pincer Ligands

3.1 Introduction **28**

3.2 Results **31**

3.2.1 Crystallography **31**

3.2.2 Conformational studies and literature comparisons **35**

3.2.3 Molecular Simulations **39**

3.2.4 HOMO-LUMO gap energies **41**

3.2.5 3-D Conformational analysis **42**

3.2.6 Solution 1H NMR studies **52**

3.2.6.1 ^{1}H NMR study as a function of [2] **52**

3.2.6.2 Dynamic ^{1}H NMR study of 2 at T < 285.15 K **55**

3.3 Conclusions **58**

3.4 References and Notes **59**

Chapter 4: Structural and Theoretical Studies on Pincer Chelates of d^8 Metal Ions

4.1 Introduction **63**

4.1.1 Background and relevance of Au(III), Pd^{2+} and Pt^{2+} complexes **63**

4.1.2 Experimental design and aims for this chapter	**65**
4.1.3 Cambridge structural database (CSD) analysis	**66**
4.2 X-Ray Crystallography	**69**
4.2.1 Crystal and molecular structure of [Au(L1)(Quinoline)][PF_6]·(CH_3CN)	**69**
4.2.2 Crystal and molecular structure of Pd(L1)(Quinoline)·(CH_3CN)$_n$	**73**
4.3 Computational Chemistry	**77**
4.3.1 General comments and procedures	**77**
4.3.2 Objectives and purpose of analysis	**78**
4.3.3 Comparison between the crystal and DFT-calculated structures	**81**
4.3.4 DFT-calculated energy profiles: Au(III) conformers (quinoline rotamers)	**82**
4.3.5 Electronic structures: pincer chelates of d^8 metals with quinoline co-ligands	**86**
4.3.5.1 Electronic structure trends: pincer chelates of d^8 metals with quinoline co-ligands	**91**
4.3.5.2 AIMAII analysis of d8 metal chelates	**101**
4.3.5.3 Literature comparison	**109**
4.4 Conclusions	**111**
4.4 References and notes	**112**
Chapter 5: Concluding Chapter	
5.1 Summary and Conclusions	**115**
5.2 Future work and unanswered questions	**119**
Chapter 6: Compiled reference list	**121**

Appendices:

Appendix A: Supplementary information for the work performed in Chapter 3	**On CD**
Appendix B: Supplementary information for the work performed in Chapter 4	**On CD**
Electronic Appendix: Contains DFT and AIM input and output files and data spreadsheets	**On attached DVD**

CHAPTER 1

Introduction

1.1 Introduction

1.1.1 Introduction and background of Au(III) complexes

1.1.1.1 Au(III) catalysts and materials

Gold complexes find use in the fields of medicine, materials science and catalysis. Geory and co-workers[1] detail how Au(III) complexes can be used as catalysts to activate triple bonds for the addition of nucleophiles. Hoffmann-Röder and co-workers[2] used Au(III) chloride as a catalyst in the conversion of functionalized hydroxyallenes into corresponding 2,5-dihydrofurans. According to their findings Au(III) chloride can be used to catalyze alkyl- and alkenyl-substituted allenes. The catalysis can be done at room temperature and gives tri- and tetrasubstituted dihydrofurans in good yields and with complete axis to center chirality transfer.

In 2000 Hashmi and co-workers[3] reported on a series of Au(III)-catalyzed reactions that combined both C-O and C-C bond formation, these reactions required 1 mol% of a $AuCl_3$ catalyst. The reactions allowed for selective cross cycloisomerization or dimerization of terminal allenyl ketones and α,β-unsaturated ketones.[3] The catalysis was so effective, that in one particular case researchers highlighted that, a $AgNO_3$ catalyzed-reaction took over a week to complete, while the same reaction, catalyzed by $AuCl_3$, took only one minute.[3] Researchers noted that the Au(III) catalysts were extremely active and allowed for reactions to be conducted at room-temperature or below.[3]

Recently, Au(III) complexes have shown significant application in the field of materials science and have the potential to be used in the production of renewable energy. This is highlighted by recent work where Wong and co-workers synthesized a class of luminescent cyclometalated alkynyl Au(III) complexes.[4] These compounds have been patented for use in organic light emitting devices.[5] Lai and co-workers[6] concluded that it may be feasible to

create efficient organic solar cells based on organometallic Au(III) complexes which have accessible long-lived triplet excited states.

Au(III) complexes have been shown to have the potential to act as oxygen sensors, in much the same way that commonly used Pd(II) and Pt(II) complexes do.[7]

1.1.1.2 Au(I) and Au(III) metallodrugs

Cisplatin is very effective drug against testicular cancer; before its introduction the testicular cancer survival rate was 10% and rose to 85% after it was introduced as a treatment option.[8] Therefore if Au(III) metallodrugs have the potential to be even more cytotoxic than cisplatin this warrants further investigation and study given how effective cisplatin already is. Given that Au(III) complexes have a different mechanism of action than cisplatin, this opens up the opportunity to use them in conjunction with cisplatin in order to kill tumor cells that have become resistant to cisplatin treatment. An example of such a compound is a Au(III) corrole, synthesized by Teo *et al*.[9] The compound is shown in Figure 1.1. This Au(III) complex exhibited high cytotoxicity towards cisplatin-resistant cancer cells.[10] It was found that the compound binds very weakly to BSA, which is thought to contribute to the higher cytotoxicity exhibited by the compound as opposed to other complexes in the series.[9] In mouse model studies, cisplatin was shown to only be effective in suppressing cisplatin-sensitive tumors, while the Au(III) corrole was effective against both the cisplatin-sensitive and insensitive tumors.[10]

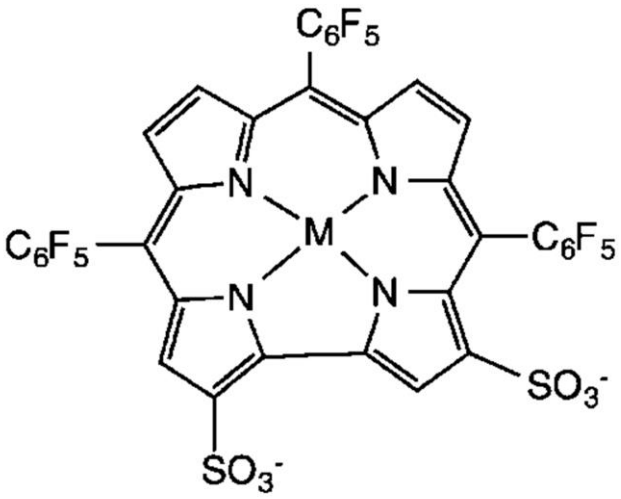


Figure 1.1. Diagram of a Au(III) corrole, synthesized by Teo *et al*.[9] This complex exhibited high cytotoxicity towards cisplatin-resistant cancer cells. In this case M = Au(III), but other suitable metals include: Fe, Mn, Al and Ga.

The cytotoxic Au(III) macrocycles made by Akerman and co-workers[11] (Figure 1.3) were shown to be topoisomerase 1 inhibitors. Topoisomerase inhibitors are validated anti-cancer drugs and they work by preventing either (i) the enzyme from binding its DNA target (catalytic inhibitor) or (ii) the enzyme from re-ligating the single cleaved strand of DNA present during turnover of the enzyme (poison). In this case the drug works by targeting the same DNA base sequence, a TA step, targeted by the enzyme for single strand scission. The properties of this interaction depen on how the thymine oxygen group and the metal center interact.

In this project we are focused on probing axial Au(III)···Q (where Q is any interacting heteroatom) interactions to obtain a better understanding of the properties of the interaction. This could yield new insight into the chemistry and reactivity of Au(III) complexes and could allow for advancements to be made that improve the turnover rate of Au(III) catalysts and improve the cytotoxicity towards tumour cells.

However, most of the current research available deals with Au(I) complexes and not with Au(III) complexes. Au(III) complexes have not been studied as extensively as Au(I) complexes. Possible reasons for this are due to the fact that Au(III) complexes are less stable and have a tendency to undergo reduction. Demetalation can occur via Au-L bond cleavage in Au(III) complexes.[12] Au(III) complexes as drugs readily undergo hydrolysis reactions and the chelates often precipitate as insoluble $AuCl_4$ or $AuCl_2$ salts.[13] Messori and co-workers highlight the differences between platinum(II) and gold(lll) complexes and explain that these differences are present due to the variation in physical properties between the two metals (where Au(III) compounds are kinetically more labile, with pronounced oxidising properties and are far more acidic when compared to platinum(II) compounds). [14]

Auranofin is an example of Au(I) complex that is of particular interest. Its efficacy is the subject of debate but the compound has been proven to inhibit the growth of certain cancer cells *in vitro*.[15] However, subsequent studies have suggested that it is only effective in mice models against the P388 leukemia cancer cell line.[16] Researchers noted that the drug inhibited the synthesis of DNA, RNA and protein but the drug showed no selectivity meaning that healthy tissues can also potentially be poisoned.[16]

Researchers have suggested a number of strategies to improve the efficacy of Au(I) and Au(III) complexes. Che *et al*.[15] suggest that increasing the Au(I)/(III)-metallodrug's stability towards thiols will improve their *in vivo* activities. The researchers suggest that making use of micro- or nano-carriers would improve the stability of the drug by safeguarding it against the reduction reactions that occur in the mammalian environment.[12, 15, 17]

The potential of gold metallodrugs is not limited to just the treatment of cancer. Certain $[Au(CN)_2]^-$ and Au(I) thiolates have been proven to be effective in the treatment of tuberculosis.[18] In addition $[Au(CN)_2]^-$ has also been shown to inhibit the proliferation of HIV in certain cultured cells, making it a potential anti-AIDS drug candidate.[19] Au(I) thiolates have extensively been used in the treatment of rheumatoid arthritis, with 10-20% of patients treated with such drugs undergoing complete remission of the illness.[20]

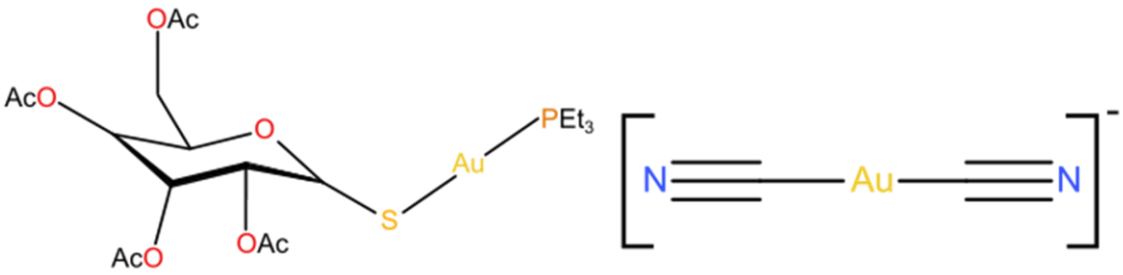


Figure 1.2. Diagram showing the structure of the Au(I) drugs Auranofin and $[Au(CN)_2]^-$.

Sun,[21] Akerman,[11] Wilson[22] and co-workers have shown that a relatively diverse group of Au(III) chelates are more cytotoxic towards certain cancer cell lines than cisplatin. This is significant because cisplatin is widely used today for the treatment of several types of tumours and can be seen as the *de facto* standard against which novel metallodrugs should be compared. Therefore this research shows that Au(III) complexes have great potential to be more effective than a commonly used cancer drug. Further exploring the applications of Au(III) complexes is also significant as this will likely increase overall drug diversity and can provide novel compounds to overcome cisplatin-resistant tumors. Akerman and co-workers

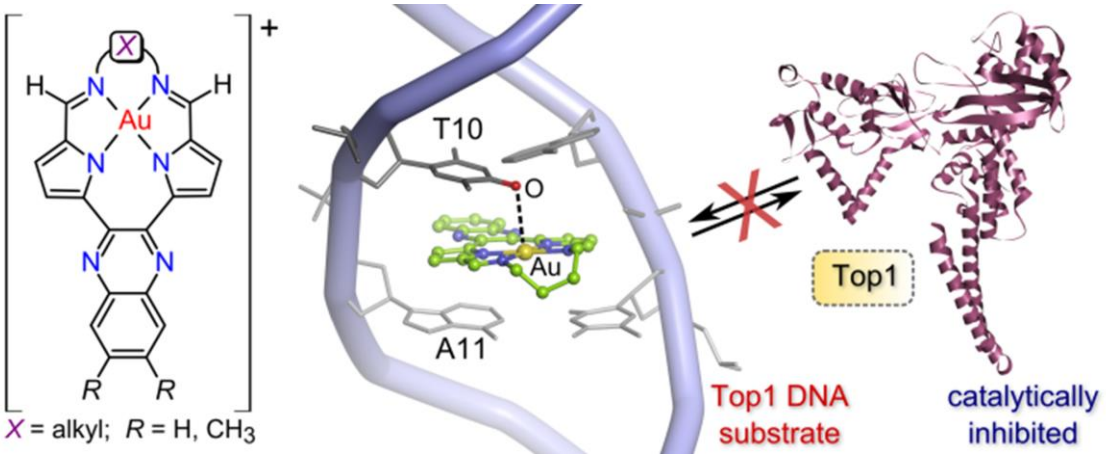


Figure 1.3. A diagram from a paper by Akerman *et al.*[11] showing that cytotoxic Au(III) macrocycles act as catalytic inhibitors of human topoisomerase I (Top 1). This study showed that this mechanism of action may be traced to the existence of a crucial Au(III)---O=C interaction with the carbonyl group of thymine in the TA base pair targeted by the metallodrug.

suggested that the mechanism of action of a novel bis(pyrrole) macrocyclic Au(III) complex was dependent on its axial Au(III)···O (presumably electrostatic) interaction with the thymine carbonyl O-atom of a DNA TA base pair and that it can only bind to their DNA target if the metal ion is Au(III), as depicted in Figure 1.3.[11] This observation shows that Au(III) complexes have a different mechanism of action to a compound like cisplatin where there is direct coordination to the nitrogen donor atom of guanine bases in dsDNA. It was also found that the complexes retained most of their cytotoxic properties when tested on a corresponding cisplatin-resistant tumor line, again indicating a different mechanism of action.[17] Although Messori and co-workers[17] were unable to report the exact mechanism of action, Gabbiani and co-workers[23] suggested that the anticancer activity of similar complexes could exhibit a mechanism of activation by reduction.

1.3 Computational chemistry

1.3.1 Quantum mechanics in computational chemistry

In this dissertation density functional theory (DFT) is used as the primary quantum chemical method of analysis. DFT has its roots in quantum mechanics and, consequently, a brief introduction to both of these topics has been given here.

The underlying theories behind the computational techniques that will be discussed in this section are based on established quantum mechanical principles. Thus it is important to introduce the computational techniques in the context of how they relate to quantum mechanical theory, in order to acquire a full understanding of the techniques involved. The equations and theory presented have been adapted from the work of Jensen.[24]

In general when an interaction occurs between two given particles, an equation describing the interaction is given in terms of force (*F*) and potential (*V*). In the following equation *r* describes the position of the particles:

$$F(r) = -\frac{\partial V}{\partial r}$$

1.3.1

At the atomic and molecular level the attraction between two given particles is described by the following equation:

$$V_{ij} = \frac{q_i q_j}{r_{ij}}$$

1.3.2

Where V_{ij} is the coulombic attraction, q_i and q_j are the charges of the interacting particles, with r_{ij} being the distance between particles i and j.

However, equation 1.3.2 alone is not sufficient; systems evolve over time and so a description of the dynamics of a system are also required. A good starting point is Newton's second law from classical mechanics:

$$F = ma = \frac{-dV}{dr}$$

1.3.3

where *F* is force, *m* is mass and *a* is acceleration.

Once again, equation 1.3.3 is not sufficient for describing electrons. This is because an electron is not classified as a classical object, due to its small size and ability to behave as both a wave and a particle (exhibits wave/particle duality). As a result in quantum mechanics the behaviour of an electron must be described using the wave function ψ. The wave function ψ is described using the time dependent Schrödinger equation:

$$H(r,t)\psi(r,t) = i\frac{\partial\psi(r,t)}{\partial t}$$

1.3.4

Note that atoms and molecules be described as classical particles. *H* is the Hamiltonian operator and ψ is the wave function. Equation 1.3.4 sufficiently describes wave/particle duality, with ψ^2 giving the probability of finding a particle at a certain position.

In the case that the Hamiltonian operator does not depend on time, equation 1.3.3 can be separated out as a phase factor, given by equation 1.3.5, where *h* is Plank's constant:

$$H(r,t) = H(r)$$

$$\psi(r,t) = \psi(r)e^{-iEt/(\frac{h}{2\pi})}$$

$$H(r)\psi(r) = E\psi(r)$$

1.3.5

The Born-Oppenheimer (BO) approximation is used to separate the time dependent Schrödinger equation out into two parts. The first part describes the electronic wavefunction of a fixed nuclear geometry, with the second part describing the electronic wave function. This approximation has a high level of accuracy where the maximum error that the approximation yields is of the order of 10^{-4} au. This approximation is described in equation 1.3.6, the electronic form of the Schrödinger equation.

$$H_{tot}\psi_{tot}(R,r) = E_{tot}\psi_{tot}(R,r)$$

$$H_{tot} = H_e + T_n$$

$$H_e = T_e + V_{ne} + V_{ee} + V_{nn}$$

$$\psi_{tot}(R,r) = \psi_n(R)\psi_e(R,r)$$

$$H_e\psi_e(R,r) = E_e(R)\psi_e(R,r)$$

$$(T_n + E_e(R))\psi_n(R) = E_{tot}\psi_n(R)$$

1.3.6

When the electronic Schrödinger equation is solved, it is possible to place the nuclei on a potential energy surface, where the global energy minimum will yield the lowest energy structure (corresponding to the geometry-optimized structure).[24] *R* denotes nuclear coordinates (subscript *n*) and *r* denotes electron coordinates (subscript *e*). *T* is the kinetic energy and *V* is the potential energy.

1.3.2 Introduction and history of the computational methods used

In this study two main computational methods have been used: Density functional theory (DFT) and Atoms in molecules analysis (AIM).

1.3.2.1 Density functional theory

Density functional theory (DFT) is currently the most successful and widely used computational method to calculate the structure and properties of atoms and molecules

(when measured by its prevalence in the literature of top journals, and the many thousands of citations per year).

DFT has the ability to calculate, with great accuracy, various physical and chemical features of a molecule. According to Cuevas, these properties include molecular structures, vibrational frequencies, atomization energies, ionization energies and electric and magnetic properties.[25]

Density functional theory is similar to another relevant computational method (that has fallen out of favour to an extent, with the rise in the popularity of DFT) known as Hartree-Fock theory (this method was simplified by Slater[26]). The two methods are similar but DFT results are more accurate and can be computed in a shorter amount of time, thus making it the more popular method of the two.[24]

A large number of researchers have refined and contributed to DFT theory, with the Thomas-Fermi model for the electronic structure of materials[24] often being credited as the first work that modern-day DFT theory is based on.

DFT was expanded upon through the work of Hohenberg and Kohn.[27] They developed two theorems, known as the Hohenberg–Kohn theorems (often abbreviated as H-K), that have proved to be of fundamental importance for the solidification of DFT theory. The first H-K theorem states, in part, that the ground state electronic energy is able to be completely determined by the electron density.[27] The second H-K theorem states that a correct ground state electron density will minimize the energy functional of the system, where the energy functional is a function of the function of the electron density.[24] These principles were further expanded upon through the work of Kohn and Sham in 1965, who produced the Kohn-Sham (or KS) equation.[28] The K-S equation is defined as the one electron Schrödinger equation of a fictitious system comprised of non-interacting electrons that generate the same density as any system of interacting particles.[28] This work essentially resulted in Walter Kohn being awarded the Nobel Prize in chemistry for “his development of the density-functional theory” in 1998. The award was shared with John Pople.[29]

A basis set is a set of functions (referred to as basis functions) that are used to represent unknown molecular orbitals or electron density in DFT calculations. These functions convert the partial differential equations of the model into algebraic equations which are able to be solved computationally.[30] The ideal basis set would be comprised of an infinite number of basis functions and as a result would be capable of perfectly describing a molecular orbital, for example. However, because such a basis set is impossible to create, only finite basis sets can exist and so only the components of the molecular orbital that can be represented

are the ones that are along coordinate axes that are described by the basis set. As a result, the smaller the basis set, the less accurate it is at describing the molecular orbital – leading to greater calculation error.[24] In this dissertation the following basis sets were used: SDD[31, 32] (Stuttgart-Dresden ECP basis set, D95[32] basis set used up to Ar), 6-311G(d,p) (6-311G basis for first-row atoms and the McLean-Chandler[33, 34] basis sets for second-row atoms) and DGDZVP[35, 36] (used for compounds containing iodine atoms). The HSEh1PBE[37-40] functional (known as the full Heyd-Scuseria-Ernzerhof functional) was used in all cases. A statistical analysis was performed to justify the use of HSEh1PBE basis set, the results of which have been included in **Appendix B**. In addition the SARC-ZORA basis set was used, which is an effective core potential basis set appropriate for heavy elements with relativistic effects. Effective core potential basis sets are used when a system contains one or more elements of large atomic number (and thus have a large number of core electrons). In such a case electron-electron repulsion effects can only be sufficiently described by using a large number of basis functions.[24] For the structures examined in this thesis, the use of SDD, 6-311G(d,p) and DGDZVP basis sets alone would not be able to describe the electron-electron repulsion effects for heavy elements like Au and Pt and so the SARC-ZORA basis set needs to be used for this purpose. When dealing with heavy d-block elements, relativistic effects can be very pronounced so it is of critical importance to use a basis set that is well suited to the chemistry of the compounds so that the simulated results can model the system as accurately as possible.[24]

1.3.2.2 Atoms in molecules analysis

Atoms in molecules (AIM) analysis is a widely used computational method and it is particularly useful in this study, where the method is used in the determining of the location of bond critical points, the electron density, and the Laplacian of the electron density at these points. The method was developed by Bader[41] and uses a topological analysis (analyses of the maxima, minima and saddle points) of the electron density to partition the physical space into atomic basins.[42] AIM analysis locates bond critical points, (BCP) which are defined as stationary points, located between two interacting or bonded atoms. Locating bond critical points is vital to this study because the electron density of a bond critical point correlates to the bond strength,[42] and so this method provides a quantitative measure of the strength of any given interaction in a structure. This is essential to our study, and to any study where probing molecular interactions is of great importance. The electron density of the interaction (ρ) as well as the second derivative of the electron density (known as the Laplacian of the electron density, $\nabla^2\rho$) of a bond critical point is able to be determined using the AIM method. The Laplacian of the electron density can be used to gauge where electron density has been

increased or decreased. At a bond critical point, the sign of the Laplacian is used to categorize the nature of the bond or interaction. $\nabla^2\rho > 0$ values are characteristic of ionic bonds and van der Waals interactions while $\nabla^2\rho < 0$ values are characteristic of covalent bonds.[42]

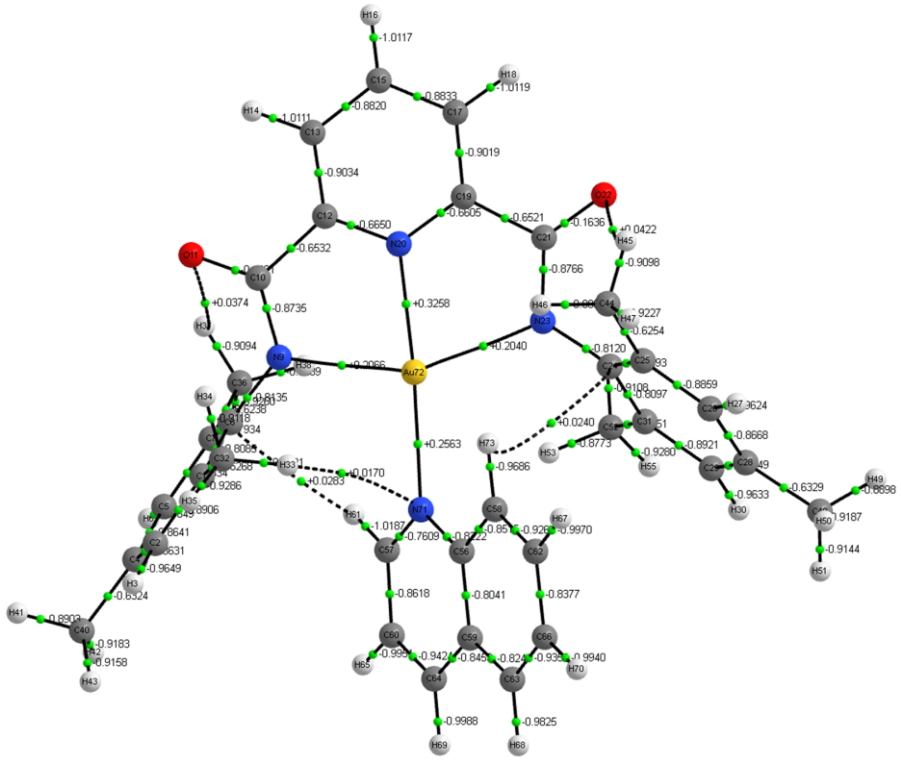


Figure 1.4. Example of an output of an Atoms in molecules (AIM) analysis (performed using the AIMAII software package). The bond critical points have been rendered as green spheres. Solid lines indicate formal bonding, while the dotted lines denote an electrostatic interaction. The numbers adjacent to the bond critical points are the Laplacian of the electron density ($\nabla^2\rho$). However this is just one of the many bond critical point properties that were calculated during the analysis; significantly, the $\nabla^2\rho$ and the electron density (ρ) values are most relevant to this work.

AIM computational analysis is often performed during preliminary or theoretical studies of novel systems and compounds. The following section presents examples of how AIM analysis has been used to answer important scientific questions and to verify certain scientific findings.

Poater and co-workers[43] made use of the AIM method in order to evaluate the electron delocalization in aromatic molecules. AIM methods were incredibly useful for this, because electron delocalization is not able to be observed, and so AIM was the method chosen to theoretically quantify the delocalization.[43]

Another paper by Poater *et al.*[44] shows a specific case where a hydrogen bonding interaction that was predicted by AIM analysis does not exist. In a paper by Matta *et al*.[45] the researchers claimed that hydrogen–hydrogen bonding between ortho-hydrogen atoms was possible. This claim was based on the result of an AIM analysis and the claim was in opposition to the currently accepted view which states that non-bonded steric repulsion between the ortho-hydrogen atoms is the reason that the planar geometry is of higher energy than the twisted geometry of biphenyl.[44] The researchers then proved that the classical, generally accepted case was the correct one by proving that hydrogen–hydrogen bonding was not occurring in the system.[44] This paper serves as a reminder that no computational chemistry method is free from error and that when tackling problems empirical data always holds more weight than computationally derived data.

In a paper by Koch *et al.*[46] researchers made use of AIM analysis to confirm the presence of C-H-O hydrogen bonds in the anti-AIDS drug Zidovudine (AZT). A paper by Grabowski[47] found that the results of an AIM analysis of the H···O-O bonding in a system strongly agreed with the empirical data and findings that were reported in three previous papers.[48-50] In a 2002 study by Quino *et al*.[51] the researchers made use of an AIM and DFT analysis to establish if anion···π Interactions do indeed exist. They found that the results of the AIM calculations were in agreement with the relevant crystallographic structures, and they were also able to conclude that the anion···π interactions in question were theoretically accounted for.[51]

In a 2014 paper, researchers[52] made use of Quantum Theory of Atoms in Molecules (QTAIM) to analyse C-H…Au and Au-Thione interactions and found that the QTAIM results were consistent with the experimentally derived data. In a 2015 paper by Gao *et al.*[53], researchers probed a number of Au…Halide interactions using AIM and used the analytical results to draw conclusions about the relative stability of selected Au-containing structures.

In 2008 paper by Nakanishi *et al.*[54] researchers used the results of AIM analysis to categorise a range of weak intermolecular interactions. These results have served as reference data for to assist researchers in classifying certain weak intermolecular interactions

Chernyshev *et al.*[55] made use of AIM analysis to report on interaction strengths and distances of various Au…Au interactions, and concluded that interatomic distance alone is not sufficient to measure the strength of aurophilic interactions; structural and computational data for the whole molecule also need to be taken into account. Jääskeläinen et al.[56] studied the nature of the interactions that exist in Au(III)-containing molecules. The researchers

performed a topological charge density investigation using the QTAIM method. The study provides a wealth of reference data that is based on both spectroscopic methods and DFT calculations.

1.4 Project Aims

1.4.1 Problem statement

In this dissertation we will be investigating the metal (M) to heteroatom (Q) interaction strength (M···Q) in a number of specifically designed transition metal complexes with a nominal d^8 electron configuration and probing the various structural and/or electronic features of the complexes which either affect, or are affected by the M···Q interaction strength.

1.4.2 Purpose of the study

1.4.2.1 Synthetic

To synthesize and fully characterize a number of pyridinedicarboxylic acid (PDA) and bis(amido)pyridine chelates of Au(III). These chelates will be preorganized to bind a quinoline co-ligand orthogonal to the plane of the Au(III) ion. The quinoline co-ligands will have the appropriate donor atoms present (Q groups) to experimentally investigate the Au(III)···Q interactions. This is a novel synthesis and as a result it is not guaranteed that such a synthesis will be possible. However, we hypothesize that the synthesis will be feasible because researchers such as Johnson *et al*.[12] and Shimada *et al*.[57] have produced structurally similar compounds. The synthetic procedures used by these two researchers have been illustrated in Figures 1.5 and 1.6. These figures also include the proposed synthetic scheme for the ligands and target metal chelates in this work.

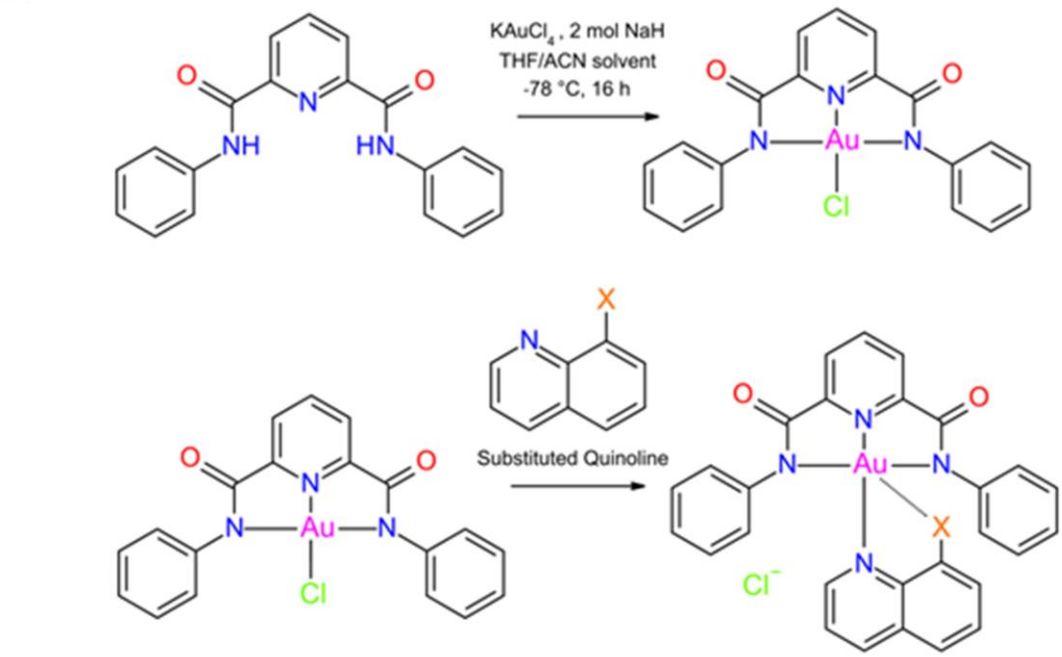


Figure 1.5. An example of a proposed synthesis (**Chapter 4**) that was based on the synthesis done in the literature method outlined by Johnson *et al.*[12]

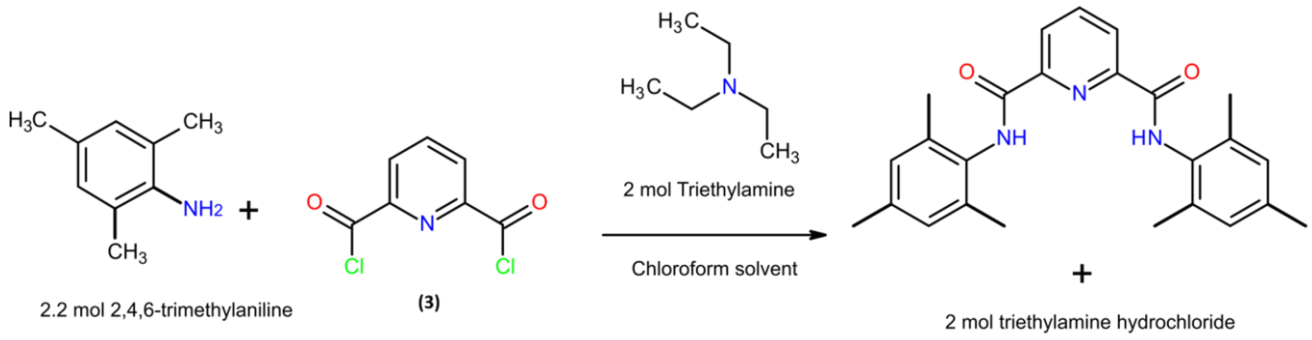


Figure 1.6. The proposed synthesis for ligands in this dissertation. The synthesis was based on the work of by Shimada *et al.*[57] as expounded in Chapter 3.

(3): 2,6-pyridinedicarbonyl dichloride

1.4.2.2 Computational and research based goals

Our first goal was to use the Cambridge Structural Database (CSD) to investigate previously reported Au(III)···Q interactions. The structures obtained would then serve as a good starting point for preliminary DFT analysis and also as a way to see what general statistical trends exist with compounds of this nature.

Our second goal follows the first; the specific objective being to investigate what range of axial interactions are possible for Au(III), Pt(II) and Pt(II) complexes. This will be achieved primarily through a search of the CSD and a subsequent analysis (along with categorization) of the search results. This will help to determine which electron donating groups are required in order to observe a significant M···Q interaction (Figure 1.7). For example: What are the relative strengths of typical axial Au(III)···F interactions? Are any variations seen when another metal is used, such as Pt(II)···F, and is the interaction more significant in the case of, for example, Au(III)···Br?

The third goal of the project is to establish how strong the interactions are. This will be done by comparing the M···Q interaction strength (where M is the relevant metal) to the strength of other types of interactions, such as hydrogen bonding or formal dative covalent bonds. This will be investigated through the use of density functional theory (DFT) simulations (using Gaussian 09W) as well as atoms in molecules (AIM) calculations. AIM analysis will be performed to calculate the electron density at the bond critical point of the interaction (in this

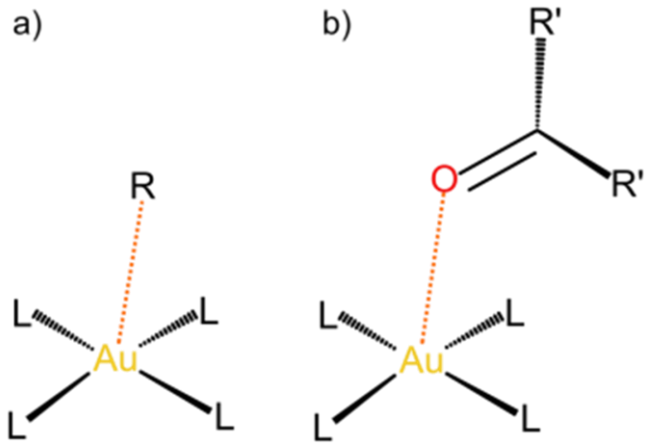


Figure 1.7. Diagram showing: (a) a generalised example of the Au(III)···Q interaction, where Q axially interacts with Au(III). (b) Specific illustration of a stabilizing Au(III)···O=C interaction.

case the M··· Q interaction) and thus give an objective measure of the interaction strength.

The fourth goal is to investigate the possible conformations and coordination geometries of Au(III), Pt(II) and Pd(II) complexes. Current molecular bonding models and molecular orbital theory predict that all Au(III), Pt(II) and Pd(II) complexes will be square planar. This reflects the invariant low-spin d^8 electron configuration of Au(III) that occurs due to the large ligand field splitting of the 5d metal ion. However, is it possible to create pseudo square pyramidal or pseudo octahedral Au(III), Pt(II) or Pd(II) complexes? Clearly as the axial M···Q interaction increases in strength the structure will tend towards a pseudo square pyramidal conformation (or a pseudo octahedral complex in the case where two axial heteroatoms interact – one above the AuN_4 plane and the other below). So this result, if observed, would contradict the commonly accepted and observed trends of molecular orbital theory.

1.5 References and Notes

1. M. Georgy, V. Boucard, O. Debleds, C. Dal Zotto and J.-M. Campagne, Tetrahedron, 2009, 65, 1758-1766.

2. A. Hoffmann-Röder and N. Krause, Organic letters, 2001, 3, 2537-2538.

3. A. S. K. Hashmi, L. Schwarz, J. H. Choi and T. M. Frost, Angewandte Chemie International Edition, 2000, 39, 2285-2288.

4. K. M.-C. Wong, L.-L. Hung, W. H. Lam, N. Zhu and V. W.-W. Yam, Journal of the American Chemical Society, 2007, 129, 4350-4365.

5. M. C. Tang, D. P. K. Tsang, M. M. Y. Chan, K. M. C. Wong and V. W. W. Yam, Angewandte Chemie, 2013, 125, 464-467.

6. S. L. Lai, L. Wang, C. Yang, M. Y. Chan, X. Guan, C. C. Kwok and C. M. Che, Advanced Functional Materials, 2014, 24, 4655-4665.

7. C. M. Lemon, D. C. Powers, P. J. Brothers and D. G. Nocera, Inorganic Chemistry, 2017, 56, 10991-10997.

8. L. H. Einhorn, Journal of Clinical Oncology, 1990, 8, 1777-1781.

9. R. D. Teo, H. B. Gray, P. Lim, J. Termini, E. Domeshek and Z. Gross, Chemical Communications, 2014, 50, 13789-13792.

10. C. T. Lum, R. W.-Y. Sun, T. Zou and C.-M. Che, Chemical Science, 2014, 5, 1579-1584.

11. K. J. Akerman, A. M. Fagenson, V. Cyril, M. Taylor, M. T. Muller, M. P. Akerman and O. Q. Munro, Journal of the American Chemical Society, 2014, 136, 5670-5682.

12. M. W. Johnson, A. G. DiPasquale, R. G. Bergman and F. D. Toste, Organometallics, 2014, 33, 4169-4172.

13. M. P. Akerman, O. Q. Munro, M. Mongane, J. A. Staden, W. I. Rae, C. J. Bester, B. Marjanovic-Painter, Z. Szucs and J. R. Zeevaart, Journal of Labelled Compounds and Radiopharmaceuticals, 2013, 56, 530-535.

14. L. Messori, G. Marcon, A. Innocenti, E. Gallori, M. Franchi and P. Orioli, Bioinorganic Chemistry and Applications, 2005, 3, 239-253.

15. T. Zou, C. T. Lum, C.-N. Lok, J.-J. Zhang and C.-M. Che, Chemical Society Reviews, 2015, 44, 8786-8801.

16. C. K. Mirabelli, R. K. Johnson, C. M. Sung, L. Faucette, K. Muirhead and S. T. Crooke, Cancer research, 1985, 45, 32-39.

17. L. Messori, F. Abbate, G. Marcon, P. Orioli, M. Fontani, E. Mini, T. Mazzei, S. Carotti, T. O'Connell and P. Zanello, Journal of Medicinal Chemistry, 2000, 43, 3541-3548.

18. C. F. Shaw, Chemical Reviews, 1999, 99, 2589-2600.

19. K. Tepperman, Y. Zhang, P. W. Roy, R. Floyd, Z. Zhao, J. G. Dorsey and R. Elder, Metal-Based Drugs, 1994, 1, 433-443.

20. G. S. Firestein, W. N. Kelley and R. C. Budd, Kelley's textbook of rheumatology, Elsevier Health Sciences, 2012.

21. R. W.-Y. Sun and C.-M. Che, Coordination Chemistry Reviews, 2009, 253, 1682-1691.

22. C. R. Wilson, A. M. Fagenson, W. Ruangpradit, M. T. Muller and O. Q. Munro, Inorganic chemistry, 2013, 52, 7889-7906.

23. C. Gabbiani, A. Casini, L. Messori, A. Guerri, M. A. Cinellu, G. Minghetti, M. Corsini, C. Rosani, P. Zanello and M. Arca, Inorganic chemistry, 2008, 47, 2368-2379.

24. F. Jensen, Introduction to computational chemistry, John Wiley & Sons, 2017.

25. J. C. Cuevas and E. Scheer, Molecular electronics: an introduction to theory and experiment, World Scientific, 2010.

26. J. C. Slater, Physical Review, 1951, 81, 385.

27. P. Hohenberg and W. Kohn, Physical review, 1964, 136, B864.

28. W. Kohn and L. J. Sham, Physical review, 1965, 140, A1133.

29. N. M. A. Web, "The Nobel Prize in Chemistry 1998" Nobelprize.org. , http://www.nobelprize.org/nobel_prizes/chemistry/laureates/1998/).

30. F. Jensen, Wiley Interdisciplinary Reviews: Computational Molecular Science, 2013, 3, 273-295.

31. P. Fuentealba, H. Preuss, H. Stoll and L. Von Szentpály, Chemical Physics Letters, 1982, 89, 418-422.

32. T. H. Dunning Jr. and P. J. Hay, in Modern Theoretical Chemistry, Ed. H. F. Schaefer III, Vol. 3 (Plenum, New York, 1977) 1-28.

33. A. McLean and G. Chandler, The Journal of Chemical Physics, 1980, 72, 5639-5648.

34. R. Krishnan, J. S. Binkley, R. Seeger and J. A. Pople, The Journal of Chemical Physics, 1980, 72, 650-654.

35. N. Godbout, D. R. Salahub, J. Andzelm and E. Wimmer, Canadian Journal of Chemistry, 1992, 70, 560-571.

36. C. Sosa, J. Andzelm, B. C. Elkin, E. Wimmer, K. D. Dobbs and D. A. Dixon, The Journal of Physical Chemistry, 1992, 96, 6630-6636.

37. J. Heyd, G. E. Scuseria and M. Ernzerhof, The Journal of Chemical Physics, 2003, 118, 8207-8215.

38. J. Heyd and G. E. Scuseria, The Journal of Chemical Physics, 2004, 121, 1187-1192.

39. J. Heyd and G. E. Scuseria, The Journal of Chemical Physics, 2004, 120, 7274-7280.

40. J. Heyd, J. E. Peralta, G. E. Scuseria and R. L. Martin, The Journal of chemical physics, 2005, 123, 174101.

41. R. F. Bader, Atoms in molecules, Wiley Online Library, 1990.

42. F. Jensen, West Sussex, England: John Wiley & Sons Ltd, 30-34.

43. J. Poater, M. Duran, M. Sola and B. Silvi, Chemical reviews, 2005, 105, 3911-3947.

44. J. Poater, M. Solà and F. M. Bickelhaupt, Chemistry-A European Journal, 2006, 12, 2889-2895.

45. C. F. Matta, J. Hernández-Trujillo, T. H. Tang and R. F. Bader, Chemistry-A European Journal, 2003, 9, 1940-1951.

46. U. Koch and P. L. Popelier, The Journal of Physical Chemistry, 1995, 99, 9747-9754.

47. S. Grabowski, Journal of Molecular Structure, 2001, 562, 137-143.

48. C. J. Smallwood and M. A. McAllister, Journal of the American Chemical Society, 1997, 119, 11277-11281.

49. S. J. Grabowski, Tetrahedron, 1998, 54, 10153-10160.

50. S. Grabowski, Journal of Molecular Structure, 2000, 552, 153-157.

51. D. Quiñonero, C. Garau, C. Rotger, A. Frontera, P. Ballester, A. Costa and P. M. Deyà, Angewandte Chemie, 2002, 114, 3539-3542.

52. L. Koskinen, S. Jääskeläinen, E. Kalenius, P. Hirva and M. Haukka, Crystal Growth & Design, 2014, 14, 1989-1997.

53. M. Gao, Q. Li, H.-B. Li, W. Li and J. Cheng, RSC Advances, 2015, 5, 12488-12497.

54. W. Nakanishi, S. Hayashi and K. Narahara, The Journal of Physical Chemistry A, 2008, 112, 13593-13599.

55. A. N. Chernyshev, M. V. Chernysheva, P. Hirva, V. Y. Kukushkin and M. Haukka, Dalton Transactions, 2015, 44, 14523-14531.

56. S. Jääskeläinen, L. Koskinen, M. Kultamaa, M. Haukka and P. Hirva, Solid State Sciences, 2017, 67, 37-45.

57. A. Shimada, T. Yaita, H. Narita, S. Tachimori and K. Okuno, Solvent Extraction and Ion Exchange, 2004, 22, 147-161.

CHAPTER 2

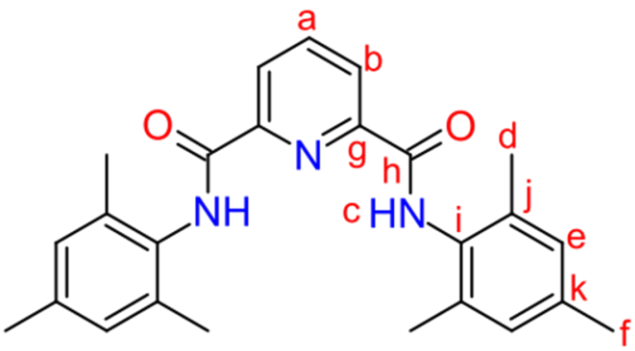
Experimental Methods

2.1 Materials

All reagents were purchased and used as received from Sigma-Aldrich. All solvents were dried with activated molecular sieves prior to use.

2.2 Synthesis of compounds

2.2.1 Pyridine-bis(amide) pincer ligands

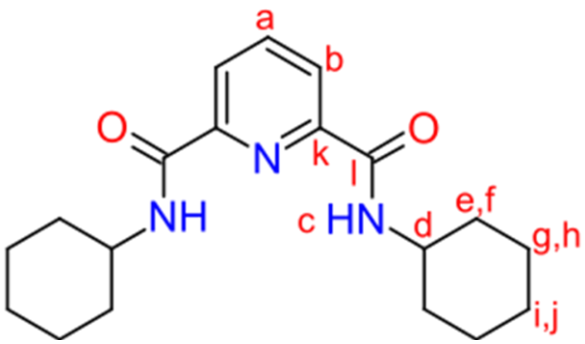


***N*,*N*'-Bis(2,4,6-trimethylphenyl)-2,6-pyridinedicarboxamide, compound 1.**

This compound was synthesized according to the procedure of Shimada *et al*.[57] The product was recovered as a crystalline white powder (88% yield). ^{1}H NMR: (300 MHz, DMSO-d_6) δ (ppm) 10.72 (s, c, 2H), 8.32 (t, a, 1H), 8.29 (d, b, 2H), 6.97 (s, e, 4H), 2.27 (s, f, 6H), 2.18 (s, d, 12H). ^{13}C (75.47 MHz, DMSO-d_6) δ (ppm) 161.5 (h), 148.6 (g), 139.9 (a), 135.9 (k), 135.2 (i), 131.9 (e), 128.3 (j), 124.6 (b), 20.5 (f), 18.0 (d). FTIR: ν_{max} (cm^{-1}): 3320 (N-H), 2925 (C-H), 1660 (C=O), 1501 (N-H), 1444, 1234, 1057, 997, 849, 648. UV–Vis (DMSO): λ_{max} (nm) [ε (M^{-1} cm^{-1})] 252 [3.61 × 10^3]; 256 [4.87 × 10^3]; 265 [9.54 × 10^3]. HRMS: (m/z) calculated for [$C_{34}H_{32}N_3O_2$]: 401.50 [M+H$^+$] found: 402.1767 [M+H$^+$].

Crystal Data for 1. $C_{19}H_{27}N_3O_2$ (*M* =329.43 g mol^{-1}): triclinic, space group P-1 (no. 2), *a* = 8.3574(2) Å, *b* = 8.3564(2) Å, *c* = 25.9552(7) Å, *α* = 81.439(2)°, *β* = 81.4460(10)°, *γ* =

89.9650(10)°, V = 1772.09(8) Å^3, Z = 4, T = 173.15 K, μ(MoKα) = 0.081 mm^{-1}, D_{calc} = 1.235 g cm^{-3}, 25733 reflections measured (3.21° ≤ 2Θ ≤ 55.994°), 8417 unique (R_{int} = 0.0676, R_{sigma} = 0.0643) which were used in all calculations. The final R_1 was 0.0896 (I > 2σ(I)) and wR_2 was 0.2243 (all data).

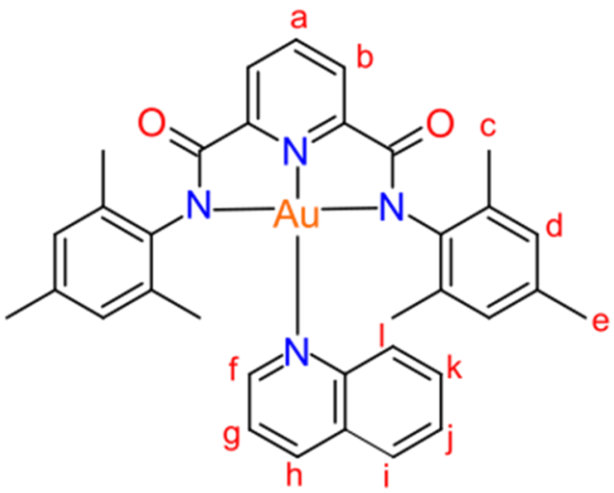


***N*,*N*'-Bis(cyclohexyl)-2,6-pyridinedicarboxamide, compound 2.**

2,6-pyridine dicarbonyl dichloride (2.9998 g 14.70 mmol) was added to chloroform (30 mL). A mixture of cyclohexylamine (3.2095 g 32.35 mmol) and triethylamine (2.9715 g 29.40 mmol) was added dropwise to the solution at which point HCl vapour was released and the temperature of the solution increased. The resulting solution was refluxed at 62 °C for approximately 2 hours. The solution was then washed with two 30 mL aliquots of NaOH (10%). The product was isolated as a white powder by suction filtration (4.5682 g, 13.87 mmol, 94% yield). ^{1}H NMR (300 MHz, $CDCl_3$) δ (ppm) 8.31 (dd, b, 2H), 7.99 (t, a, 1H), 7.52 (d, c, 2H), 3.99 (tt, d, 2H), 2.03 (m, ef, 8H), 1.61 (m, gh, 8H), 1.38 (m, ij, 8H). ^{13}C NMR (300 MHz, $CDCl_3$) δ (ppm) 162.5 (l), 149.1 (k), 138.9 (a), 124.9 (b), 48.3 (d), 32.9 (e), 25.5 (i), 24.8(j). FTIR: ν_{max} (cm^{-1}): 3277 (N-H), 2927, 2851, 1638 (C=O), 1537, 1444, 1323, 1250, 1174, 1087, 999, 888, 839, 752, 724, 668. UV–Vis (DMSO): λ_{max} (nm) [ε (M^{-1} cm^{-1})] 251 [1.33 x 10^2]; 261 [3.35 x 10^2]. HRMS: (m/z) calculated for [$C_{34}H_{32}N_3O_2$]: 329.44, found: 330.1832.

Crystal Data for: $C_{19}H_{27}N_3O_2$ (M =329.43 g mol^{-1}): triclinic, space group P-1 (no. 2), a = 8.3574(2) Å, b = 8.3564(2) Å, c = 25.9552(7) Å, α = 81.439(2)°, β = 81.4460(10)°, γ = 89.9650(10)°, V = 1772.09(8) Å^3, Z = 4, T = 173.15 K, μ(MoKα) = 0.081 mm^{-1}, D_{calc} = 1.235 g cm^{-3}, 25657 reflections measured (3.21° ≤ 2Θ ≤ 55.994°), 8413 unique (R_{int} = 0.0515, R_{sigma} = 0.0589) which were used in all calculations. The final R_1 was 0.0940 (I > 2σ(I)) and wR_2 was 0.2427 (all data).

2.2.2 Metal chelates of pincer ligands

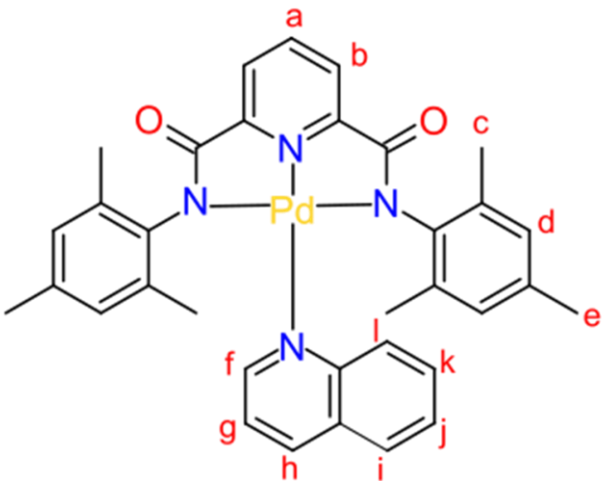


***N,N'*-Bis(2,4,6-trimethylphenyl)-2,6-pyridinecarboxamidato(quinoline)Au(III)**

***N,N'*-Bis(2,4,6-trimethylphenyl)-2,6-pyridinedicarboxamide** (0.2125 g, 0.053 mmol) was dissolved in acetonitrile (25 mL). To this solution NaH (in a mineral oil dispersion 0.0457 g, 0.106 mmol) was added and the resulting mixture was stirred at room temperature for approximately 1 hour. A solution of $KAuCl_4$ (0.200 g, 0.053 mmol), $AgPF_6$ (0.401 g, 0.159 mmol) and acetonitrile (10 mL) was slowly added, the mixture was heated to reflux for 2 hours at 82 °C. At this point, a solution of quinoline (0.0683 g, 0.053 mmol), $AgPF_6$ (0.1338 g, 0.053 mmol) and acetonitrile (5 mL) was added and the mixture was refluxed for 2 days at 82 °C. Red-orange powder and crystals were obtained after slow evaporation from acetonitrile (0.2233 g, 58.50% yield). ^{1}H NMR (300 MHz, DMSO-d_6) δ (ppm) 8.92 (d, 1H, f), 8.66 (m, 1H, l), 8.32 (t, 1H, a), 8.29 (d, 2H, b), 8.16 (t, 1H, h), 8.02 (t, 1H, i), 7.78 (t, 1H, j), 7.62 (t, 1H, k), 7.55 (m, 1H, g), 6.89 (s, 4H, d), 2.27 (s, 6H, e), 2.18 (s, 12H, c). Results of ^{13}C NMR analysis were hampered by poor solubility and poor yields, as a result signals were of very low intensity and could not be accounted for, but have been included in **appendix A**. FTIR: ν_{max} (cm^{-1}): 3639, 2922, 1645 (C=O), 1570, 1368, 1056, 828. UV–Vis (DMSO): λ_{max} (nm) [ε (M^{-1} cm^{-1})] 267 [5.21 x 10^3]; 370 [1.23 x 10^3]. HRMS: (m/z) calculated for [$AuC_{34}H_{32}N_4O_2$]: 725.609, found: 725.219.

Crystal data for: $AuC_{34}H_{32}N_4O_2(C_2H_3N)(PF_6)$ (M = 911.62 g mol^{-1}): orthorhombic, space group *Pna*21 (no. 33), a = 14.4091(11) Å, b = 15.3724(12) Å, c = 16.0382(13) Å. α, *β* and *γ* = 90°, V = 3552.5(5) Å^3, *Z* = 4, *T* = 173.15 K, μ(MoKα) = 4.258 mm^{-1}, D_{calc} = 1.704 g cm^{-3}, 61859 reflections measured (5.814° ≤ 2Θ ≤ 54.556°), 7887 unique (R_{int} = 0.0663, R_{sigma} =

0.0449) which were used in all calculations. The final R_1 was 0.0492 ($I > 2\sigma(I)$) and wR_2 was 0.1296 (all data).



***N,N'*-Bis(2,4,6-trimethylphenyl)-2,6-pyridinecarboxamidato(quinoline)palladium(II)**

***N,N'*-Bis(2,4,6-trimethylphenyl)-2,6-pyridinedicarboxamide** (0.1144 g, 0.029 mmol) was dissolved in acetonitrile (25 mL). To this solution NaH (in a mineral oil dispersion 0.0243 g 0. 056 mmol) was added and the resulting mixture was stirred at room temperature for approximately 1 hour. A solution of $PdCl_2$ (0.0506 g, 0.029 mmol) and acetonitrile (10 mL) was slowly added; the mixture was then refluxed for 2 hours at 82 °C. At this point, a solution of quinoline (0.0122 g, 0.094 mmol) and acetonitrile (5 mL) was added and the mixture was refluxed for 3 days at 82 °C. Yellow powder and crystals were obtained after slow evaporation from acetonitrile (0.0851 g, 79.31% yield). ^{1}H NMR (300 MHz, $CDCl_3$) δ (ppm) 8.90 (m, 1H, f), 8.44 (d, 1H, l), 8.19 (m, 2H, b), 8.09 (m, 1H, a), 7.94 (m, 1H, h), 7.84 (m, 1H, i), 7.64 (m, 1H, j), 7.50 (m, 1H, k), 7.36 (m, 1H, g), 6.32 and 6.11 (s, 4H, d), 2.26 (s, 12H, c), 1.95 (s, 6H, e). Results of ^{13}C NMR analysis were hampered by poor solubility and poor yields, in addition to some impurities; signals could not be accounted for, but have been included in **Appendix A**. FTIR: vmax(cm^{-1}): 2962, 2250, 1584 (C=O), 1478, 1378, 1259, 1015, 796, 679, 558. UV–Vis (DMSO): λ_{max} (nm) [ε (M^{-1} cm^{-1})] 330 [4.72 x 10^3]; 360 [3.01 x 10^3]. HRMS: (m/z) calculated for [$PdC_{34}H_{32}N_4O_2$]: 635.065, found: 635.230.

Crystal Data for: $PdC_{34}H_{32}N_4O_2$ (M = 635.03 g mol^{-1}): orthorhombic, space group *Pbc*n (no. 60), a = 33.3299(15) Å, b = 13.9723(6) Å, c = 15.3608(6) Å. α, *β and* γ = 90°, V = 7153.5(5) $Å^3$, Z = 8, T = 296.15 K, μ(MoKα) = 0.550 mm^{-1}, D_{calc} = 1.179 g cm^{-3}, 60135 reflections measured (2.444° ≤ 2Θ ≤ 56.782°), 8818 unique (R_{int} = 0.0614, R_{sigma} = 0.0505)

which were used in all calculations. The final R_1 was 0.1412 ($I > 2\sigma(I)$) and wR_2 was 0.4496 (all data).

It should be noted that no complexed forms of ligand **2** were able to be synthesised. It is possible that the established techniques used in the synthesis of *N,N'*-Bis(2,4,6-trimethylphenyl)-2,6-pyridinecarboxamidato(quinoline)palladium(II) and *N,N'*-Bis(2,4,6-trimethylphenyl)-2,6-pyridinecarboxamidato(quinoline)Au(III) are not suitable for the synthesis of ligand **2** derivatives. This is an area that requires further investigation before any meaningful conclusions can be made.

CHN analysis was not performed because not enough pure product was able to be synthesised and isolated and the proton spectrum reflected sufficient bulk sample purity. These points coupled to the fact that the Chemistry Department at the University of Witwatersrand does not have a CHN instrument, lead to such an analysis not being performed.

2.3 Single-crystal X-ray diffraction

In all cases a suitable single crystal was selected and mounted in Paratone® oil within a polymer microloop (MiTeGen) on a Bruker APEX-II CCD diffractometer or a Bruker D8 Venture CMOS diffractometer. The crystal was kept at 173.15 K during data collection. Using Olex2,[58] the structure was solved with the ShelXS[59] structure solution program using direct Methods and refined with the ShelXL.[59]

Intensity data were collected at −100 °C using a Bruker APEX II CCD area detector diffractometer with graphite monochromated Mo Kα radiation (50 kV, 30 mA). APEX2 was used to control data collection; unit cell refinement and data reduction were effected with SAINT.[60] The crystal structures were solved by direct methods using SHELXS[59] and subsequently refined with SHELXL[59]. Non-hydrogen atoms were first refined isotropically followed by anisotropic refinement employing full matrix least-squares calculations based on F^2. H atoms were refined isotropically in calculated positions with the standard riding model of SHELXL.[59]

Single crystals of $C_{19}H_{27}N_3O_2$, **2**, were isolated as colourless needles. A suitable crystal was selected and mounted in Paratone® oil within a polymer microloop (MiTeGen) on a Bruker APEX-II CCD diffractometer. The crystal was kept at 173.15 K during data collection. Using Olex2,[58] the structure was solved with the ShelXS structure solution program using direct methods and refined with the ShelXL[59] refinement package using Least Squares minimization. The crystal was twinned and refined using the twin law [1 -1 0] to account for

the intensity data. The twin fraction was 0.46. Residual electron density peaks in the plane of each pyridine ring for the two independent molecules in the asymmetric unit (final model) indicated possible further (yet unresolvable) disorder, twinning, or co-crystallization of unreacted 2,6-pyridinedicarboxylic acid. Attempts to deal with the additional residual electron density were unsuccessful. The model was, however, of a suitable quality to ignore the minor contribution from the unassigned electron density peaks (none exceeded 1.5 e $Å^{-3}$).

Full tables summarizing the X-ray data of each of the structures has been included in **Appendices A** and **B**.

2.4 UV-Visible spectroscopy

Electronic spectra were recorded with an Analytik Jena Specord210 Plus double-beam spectrometer at ambient temperature. This was done using increasing concentrations in order to determine extinction coefficients of the compounds and to characterize them. All experiments were performed at 20 °C, using DMSO as a solvent. Quartz crystal cells were used and the cell pathlength was 1 cm.

2.5 Fourier-transform infrared spectroscopy

FTIR spectra were recorded with a Bruker Alpha FTIR spectrometer (0.8 cm^{-1} resolution; 32 scans) fitted with a Platinum® diamond ATR sample accessory on dry, polycrystalline samples.

2.6 High resolution mass spectroscopy

HRMS analysis for all samples was performed on a Bruker Compact Q-TOF high resolution mass spectrophotometer. 10 µL samples were injected into the UHPLC and eluted isocratically for 1 min, starting at 50% solvent A (consisting of 0.1% formic acid /H_2O (v/v)) and 50% solvent B (consisting of 0.1 % formic acid acid/Acetonitrile (v/v)). Samples used in this analysis were dissolved in an HPLC-grade acetonitrile to a concentration of approximately 10 ppm.

2.7 ^{1}H and ^{13}C NMR

^{1}H NMR and ^{13}C NMR data were recorded on a Bruker Advance 300 NMR spectrometer operating at 300 MHz and 75.47 MHz, respectively. Chemical shifts are reported in parts per million (δ) and were referenced against 0.03% tetramethylsilane (TMS) as an internal standard. The NMR data were analysed using the MestReNova 9 software suite.[61] NMR analysis was performed on the samples in order to characterize them and to check for purity.

2.8 Gaussian09W and Gaussview

Density functional theory calculations were performed using the Gaussian09W (revision D.01) software package. The package was used to obtain the geometry optimized structures of the various ligands and gold complexes that were examined in this dissertation. In addition, conformational energy analyses were performed by single- and dual-dihedral angle scans to map the accessible regions of conformational space for selected ligands and complexes. Calculations were performed at varying levels of theory, which were appropriate to the specific compound being investigated. The following parameters were given as inputs: Job Type was set as an optimization and frequency calculation with the VCD (vibrational circular dichroism) being calculated (keyword opt freq=vcd). In all cases the method was set to ground state DFT with default spin at the HSEH1PBE level of theory, with either SDD or GEN keyword for basis set (keyword: hseh1pbe/sdd (or gen)/auto). For the population analysis NPA was chosen (keyword pop=npa). The solvation model was set as none, except in two cases were DMSO was selected as the solvent (keyword: scrf=(solvent=dmso)). In all cases the “geom=connectivity” keyword was used. In cases where torsion coordinate scans were performed the “opt freq=vcd” keywords were replaced with “opt=modredundant”. Gaussview was used to edit .mol2 files so that they could be given as inputs into Gaussian09W.

2.8.1 Chapter 3 DFT calculations

N,*N*'-Bis(2,4,6-trimethylphenyl)-2,6-pyridinedicarboxamide (compound 1 or H_2L1) **and** *N*,*N*'-Bis(cyclohexyl)-2,6-pyridinedicarboxamide (compound 2 or H_2L2): Both geometry optimization calculations and torsion angle drive scans were performed (*in vacuo*) at the HSEH1PBE/SDD level of theory.The specific details of the scans have been illustrated in Chapter 3.

2.8.2 Chapter 4 DFT calculations

Both geometry optimization calculations and torsion angle drive scans were performed (*in vacuo*) at the HSEH1PBE/SARC-ZORA/6-311G(d,p)/DGDZVP level of theory (the basis set used depended on the particular compound; see Chapter 4 for compound-specific details)**.** The specific details of the scans have been illustrated in Chapter 4.

2.9 AIM analysis

Atoms in molecules analysis was performed using the AIMAII (AIMQB professional) software package.[62] This package was primarily used to calculate the electron density of the bond

critical point of the M···Q interaction. However other parameters were also obtained in the analysis, such as the Laplacian of the electron density. The AIMQB professional software package was used to perform the analysis and formatted Gaussian09W checkpoint files were used as the input wavefunction file for analysis. The connectivity and integration of all atoms in the compound was considered. The basin integration method was set to Auto/Fine IAS Mesh/Auto Capture. The basin quadrature and maximum integration radius were both set to Auto. CP (critical point) connectivity search was set to complex. Magnetic response properties and atomic Ehrenfest forces were not calculated. The atomic Laplacian of critical points was calculated, energy components were set as T(A), Vne(A), Ven(A), Vnn(A). The information obtained as a result of the AIM analysis was used to investigate the relative strength of the M···Q the interaction and compare it to the strength of covalent M-X bonds.

2.10 NBO 3.1

The NBO 3.1 software package (running in Gaussian09W) was used to analyse the many-electron molecular wavefunction in terms of localized electron-pair bonding' units.[63] For our analysis natural population analysis (NPA) only was calculated (keyword pop=npa in Gaussian09W). The program uses the results from the determination of natural atomic orbitals (NAOs), natural hybrid orbitals (NHOs), natural bond orbitals (NBOs) and natural localized molecular orbitals (NLMOs) to perform the NPA analysis.[63]

2.11 Biovia Discovery Studio and Mercury

In this work similarity index (SI) values were obtained by superimposing the crystal structure and the DFT-calculated output structure of the same compound. The SI values that are reported in this work were computed using the Discovery Studio (version 4.5) software package. The Mercury (version 3.9) software package was used for viewing and analysing compounds that were found in the CSD.

2.12 CSD and ConQuest

CSD (Cambridge Structural Database) is a database that contains published single-crystal data for small molecules. The CSD version 5.38 November 2016 update was used. The database was accessed using ConQuest 1.19. We made use of the database by searching to find all available experimental Au(III) structures that exhibited the off-axial interaction (with respect to the plane of the AuX_4 square planar interactions). This was done in an effort to get an idea of the frequency with which this interaction occurred, and also allowed for us to obtain published structures with which to analyse together with our proposed series of Au,

Pd and Pt structures. In particular the CSD was used to see what general statistical trends exist with compounds of this nature and to see what range of axial interactions are possible, how much lateral displacement occurs (from orthogonality to the square planer plane of AuX_4), and what types of electron donating groups are required in order to observe a significant Au···Qinteraction.

2.13 References and Notes

58. O. V. Dolomanov, L. J. Bourhis, R. J. Gildea, J. A. Howard and H. Puschmann, Journal of Applied Crystallography, 2009, 42, 339-341.

59. G. M. Sheldrick, Acta Crystallographica Section C: Structural Chemistry, 2015, 71, 3-8.

60. Bruker (2012). SAINT. Bruker AXS Inc., Madison, Wisconsin, USA

61. Mnova 09, Mestrelab Research, 2014.

62. AIMAll (Version 17.11.14), Todd A. Keith, TK Gristmill Software, Overland Park KS, USA, 2017 (aim.tkgristmill.com)

63. E. D. Glendening, A. E. Reed, J. E. Carpenter, F. Weinhold. NBO Version 3.1

CHAPTER 3

Structural, Spectroscopic, and DFT Studies on Tridentate Pincer Ligands

3.1 Introduction

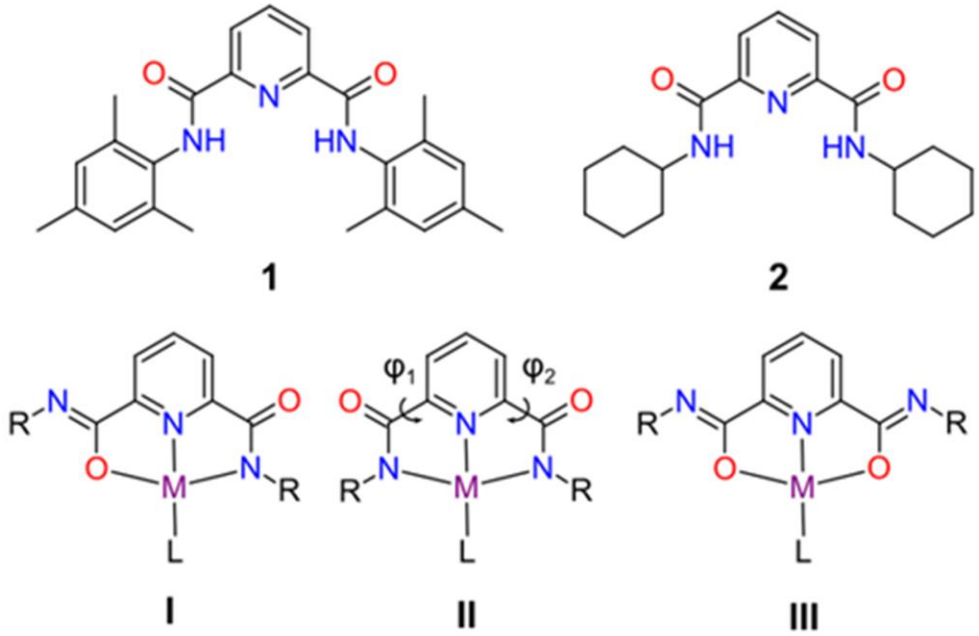
Tridentate bis(amide) pincer ligands comprising a central pyridine ring are synthetically tractable and well-suited to tight chelation of a range of transition metal ions, especially the deprotonated dianionic species, N^-–N_{py}–N^- (N_{py} denotes the pyridyl nitrogen atom). These attributes, combined with generally low-cost syntheses, underpin favourable applications of generic NNN pincer-type complexes in a number of important fields, including catalysis,[64-67] chemical mustard molecular recognition,[68] nitric oxide scavenging,[69] C–H bond activation,[70] CO_2 fixation,[71] and medicinal chemistry (e.g. anticancer agents).[72] The tridentate bis(amide) ligand system may be used practically to add thermodynamic stability and rigidity to a range of chelated metal ions.[73-76] Thus, various metal complexes of bis(amide) pincer ligands such as **1** and its analogues (Figure 3.1) have been readily crystallized and structurally elucidated. Several recent studies have focused on using the phenyl analogue of compound **1** (N^2,N^6-diphenylpyridine-2,6-dicarboxamide),[73, 74] while reports on applications of **1** are notably more prevalent, dating from as far back as 1997.[74-78]

Tridentate bis(amide)pyridyl pincer ligands have been successfully complexed to Ni(II),[73] Cu(III),[70, 79] Au(III), [74] Pd(II),[77] Co(III), [75], Fe(III),[75] U(VI),[78] and Ru(III).[76] A number of metal-to-ligand stoichiometries are observed, most commonly 1:1, but also 1:2 (M:L) in the case of metal ions such as Co(III), Fe(III), and Ru(III), which have a preference for octahedral coordination. In the case of U(VI), ancillary ligands (in conjunction with the single pincer ligand) complete the coordination group. Hirao and co-workers[80] were among the first to investigate the catalytic applications of metals complexed by tridentate bis(amide)pyridyl ligands. Specifically, the Fe(II) chelate of **1** was used in the catalytic epoxidation of 2-norbornene.

Metal complexes of bis(amide)pyridyl pincer ligands such as **1** and its structural analogues feature coordination by the doubly-deprotonated ligand. Most synthetic strategies for metalation thus include a step to first completely deprotonate the amide N-H groups prior to metal addition, ensuring higher reactivity from the dianionic form of the ligand. Previous researchers[74, 75] have highlighted how the anionic nature of the deprotonated amide nitrogen atoms of **1** are effective at stabilizing the trivalent oxidation state of metal ions, for instance Cu(III),[79] Au(III),[74] Co(III),[75] and Fe(III).[75] This is significant because a major barrier to the study of Au(III) complexes, including in vogue metallodrug candidates,[22] has been their tendency to readily decompose in the mammalian environment,[13, 17] or in solutions in the presence of reducing agents.[81, 82] Recently, Johnson and co-workers[74] synthesized and crystallized stable Au(III) complexes of **1**. This choice of ligand system provided additional thermodynamic stability to the complex, thereby expediting a route through which relatively stable Au(III) N^-–N_{py}–N^- pincer complexes might be exploited in modern metallodrug and catalyst designs.

Given the multi-faceted importance of bis(amide)pyridyl pincer ligands in coordination chemistry, we sought to gain a better understanding of how steric and electronic factors dictate the conformational architecture of this class of ligands. Notably, rotation about one or both N_{py}–C–C–O torsion angles (ϕ_1 and ϕ_2 in Scheme 3.1) can switch the ligand denticity from N^-–N_{py}–N^- to N^-–N_{py}–O^-, as seen in chelates of Ni(II),[65] Fe(III),[83] and Ru(II),[84] or, in the case of double-rotation and resonance re-hybridization, to O^-–N_{py}–O^- (observed for some Ru(II) complexes).[65, 69] Since the switch in ligand denticity (linkage isomerism) ostensibly originates from a conformational switch in the free ligand before chelation of the metal ion, key questions to answer include: (i) what conformational energy landscape exists for this class of ligands, (ii) what barriers to conformational interconversion link the most favourable minima on the potential energy (PE) surface, and (iii) how do known crystallographically characterized conformers of metal chelates and free ligands correlate with global and local minima on the PE surface.

Ultimately, our objective is to delineate to what extent conformational changes and linkage isomerism dictate the reactivity (and biological activity) of this class of NNN pincer complexes. The first step towards this end goal, however, is to understand the conformational space accessible to the free ligands. Herein we present the crystal structures and conformational analysis of two bis(amide) pincer ligands, namely *N*,*N*'-bis(2,4,6-trimethylphenyl)-2,6-pyridinedicarboxamide, **1**, and *N*,*N*'-bis(cyclohexyl)-2,6-pyridinedicarboxamide, **2**. Compound **2** is novel, while the crystal structures of both **1** and **2** are unprecedented; their intrinsically different levels of delocalization (amide groups and appended 6-membered rings) provide the necessary means to gauge the role of extended conjugation in the conformational energetics.



Scheme 3.1. Scheme depicting linkage isomers of *N*,*N*'-bis(2,4,6-trimethylphenyl)-2,6-pyridinedicarboxamide (**1**) and *N*,*N*'-bis(cyclohexyl)-2,6-pyridinedicarboxamide (**2**). Linkage isomers **I** to **III** result from rotations about ϕ1 and ϕ2 and resonance re-hybridization of the amide groups of the ligand. Linkage isomers are drawn for an arbitrary metal ion M with square planar geometry and a fourth ligand L.

3.2 Results

3.2.1 Crystallography

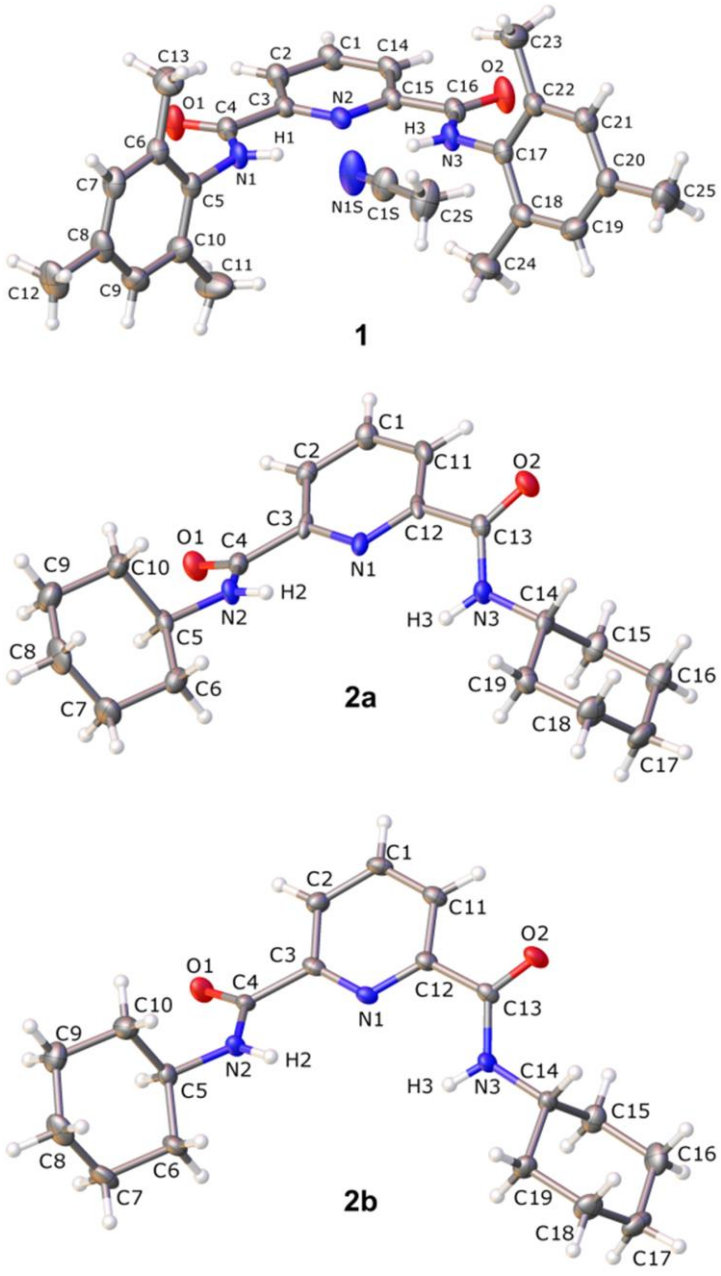


Figure 3.1: Thermal ellipsoid plots (50% probability surfaces) for the low-temperature X-ray structures of **1** and **2**. The atom numbering schemes are included. The structure of 2 comprises two independent molecules in the asymmetric unit (ASU); these are shown separately as **2a** and **2b**. Hydrogen atoms have been rendered as spheres of arbitrary radius.

The X-ray structures of **1** and **2** are shown in Figure 3.1.

From the crystal structure of **1** it is evident that, to minimise repulsion, the bulky methyl groups present in the ligand should be approximately 90° to the pyridine ring of the pincer donor atoms. However in the crystal structure, ϕ1 = 105.0° and ϕ2 = 91.6° meaning that both angles deviate slightly from perfect orthogonality (Figure 3.2). This deviation is probably due to twisting and a minor conformational adjustment to keep the acetonitrile solvent molecule locked in the hemi-cavity (binding pocket). The amide nitrogens are orientated in an endo/endo fashion, with both nitrogens orientated towards one another, which makes it possible for the acetonitrile solvent molecule to be electrostatically held in place.

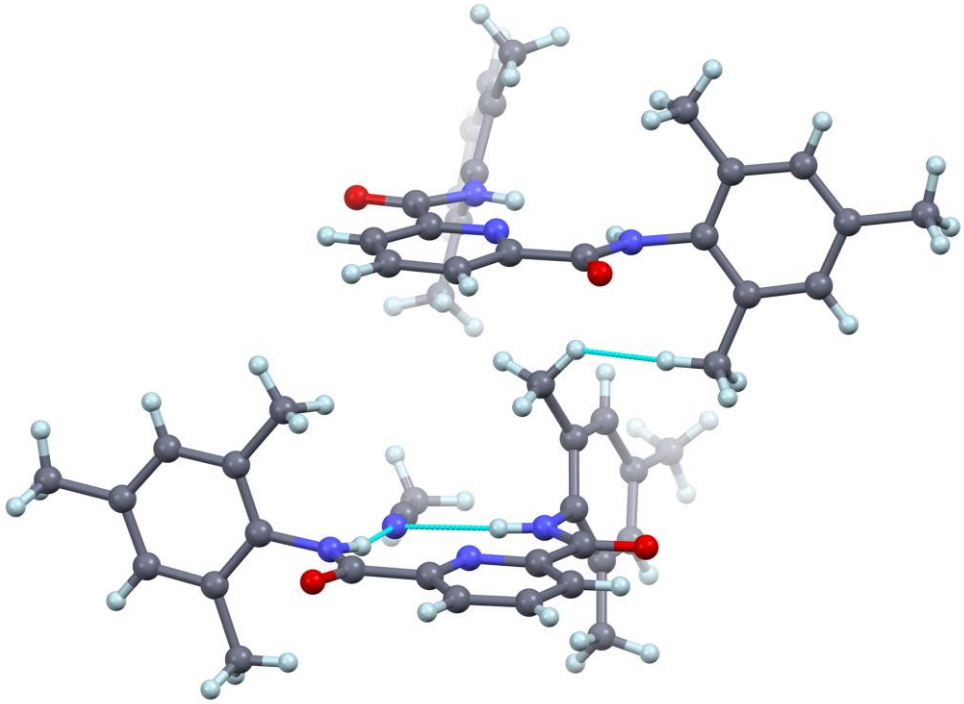


Figure 3.2 Diagram highlighting how intermolecular non-bonded contacts impact the dihedral angles of the mesityl rings in structure **1**.

In the case of compound **2**, the aliphatic rings are expected to have a greater degree of freedom when compared to **1**, due to the lack of bulky methyl substituents on the aliphatic rings. As a result the structure of **2** is far more contorted; this is evidenced by the torsion angles ϕ1 = 149.6° and ϕ2 = 152.2°. A significant contributing factor to the structural contortion is the presence of very pronounced one-dimensional hydrogen bonding. While the structure is a one-dimensional H-bonded chain, the independent molecules in the asymmetric unit constitute a unique pair which repeats along the one-dimensional chain. This unique pair constitutes a H-bonded dimer, which then oligomerizes in the solid state to form the one-dimensional chain. This hydrogen bonding chain is possible because the N-$H_{(amide)}$ hydrogen atoms swivel slightly away from the hemi-cavity in order to from the classic strong hydrogen

bonding seen in Figure 3.3. As a result the compound is decidedly non-planar. This observation is in opposition to the DFT-calculated structure of **2**, which is planar (Figure 3.4). In the DFT-calculated structure of **2** the amide hydrogens are also orientated directly towards the hemi-cavity. This is in contrast to the experimentally observed N-H group orientations. The reason for the difference between the DFT-calculations and the X-ray structure is that lattice effects (in the form of packing interactions) are not taken into account when the DFT calculation is performed.

While

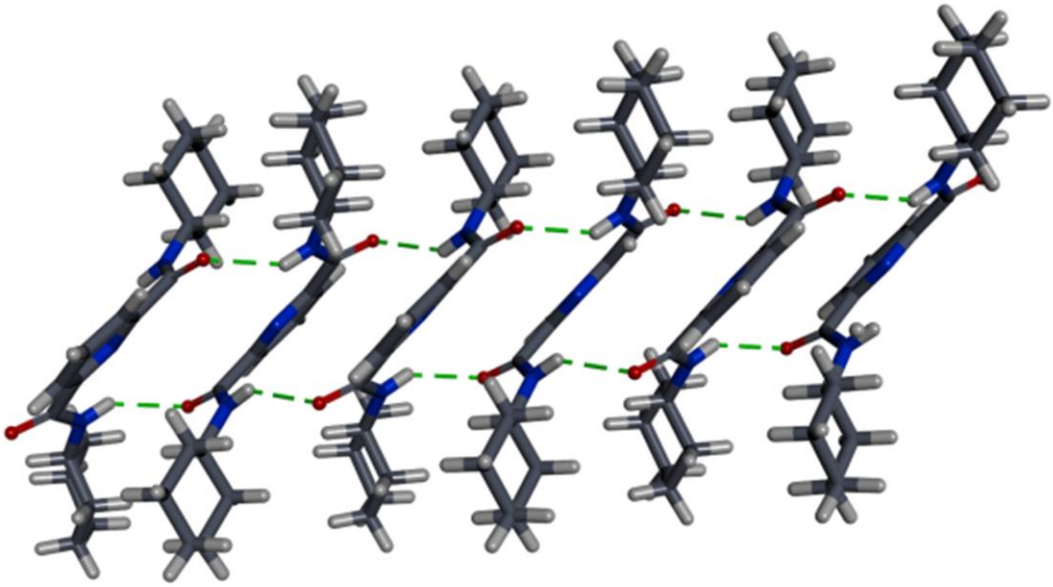


Figure 3.3. Packing diagram showing the intermolecular interactions between molecules of a dimer of **2**. Hydrogen bonds have been shown green. The distance of the $O_{(carbonyl)}\cdots N_{(amide)}$ interaction alternates between 2.229 Å to 2.231 Å with each subsequent addition to the one-dimensionally bonded sequence.

compounds **1** and **2** both exhibit an endo/endo conformation (with respect the amide groups), the amide hydrogens are oriented very differently, making the two seemingly similar structures have very different conformations.

Figure 3.4 shows a comparison between DFT-calculated, and crystallographically derived structures of **1**, **2a** and **2b**. In all cases the similarity indices (SI) are greater than 90%. Because the DFT calculations were performed in *vacuo*, no crystal packing effects were taken into account, and so this accounts for the variations seen between the crystal and DFT-calculated structures.

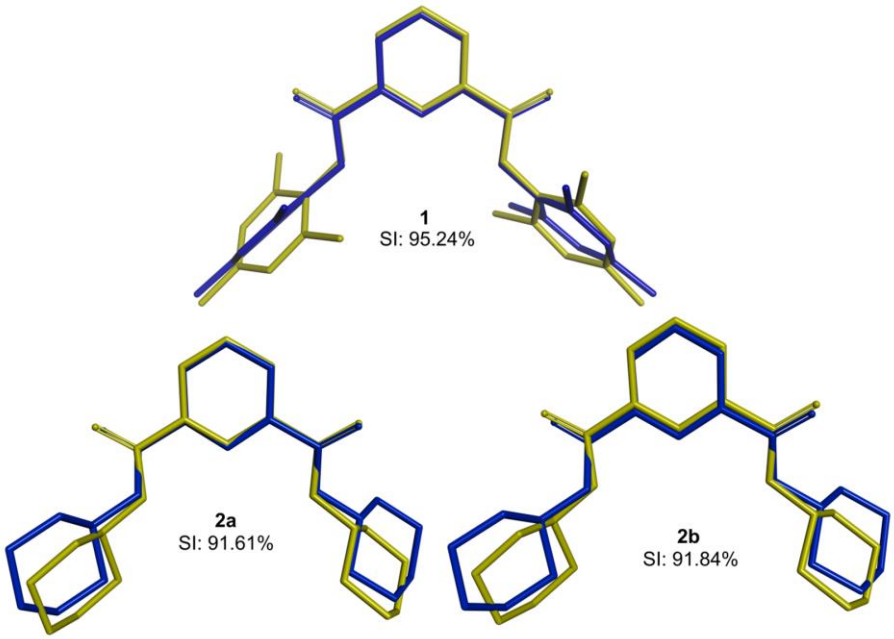


Figure 3.4: A comparison between the DFT-calculated (yellow) and the X-ray crystal structure (blue) of compounds **1** and **2**. The crystallographically-independent molecules of **2** are shown separately as **2a** and **2b**. Hydrogen atoms excluded for visibility. SI values: **1:** 95.24 % **2a**: 91.61 % **2b**: 91.84 %

Many of the structural and electronic differences between ligands **1** and **2** are due to the differences between aryl and aliphatic ring systems. There is a greater degree of resonance delocalization that occurs for the aryl pincer, which results in no dimerization (Figure 3.3) being observed for **1**. As a result one might expect that the bond lengths and angles in compound **2** would be more variable than those of compound **1**, however this is not seen to be the case despite the greater degree of resonance delocalization.

Compound **1** appears to act as an acetonitrile receptor where the acetonitrile molecule is held in place by hydrogen bonds. The acetonitrile is held in the binding pocket, approximately equidistant from the two amide hydrogens (where $N_{(acetonitrile)}\cdots H\text{-}N_{(amide)}$ is 2.307 Å and 2.263 Å). This is an example of a bifurcated hydrogen-bond that anchors the acetonitrile molecule in place.

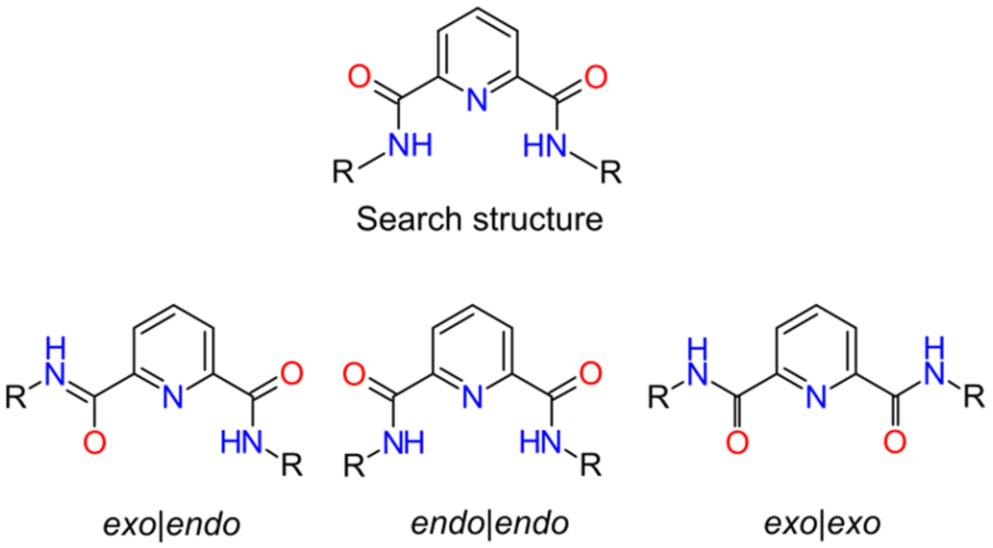
It is worth noting that independent molecules **2a** and **2b** exhibit approximate C_2 symmetry about the plane that passes through N1-C1. This is an unexpected result because the molecule crystalizes in the $P\bar{1}$ space group, which contains no C_2 symmetry elements. This is likely due to the presence of the one-dimensional hydrogen-bonded chain; the hydrogen-bonded units are related by inversion symmetry.

Thus the inversion symmetry that is present between the molecules that compose the hydrogen-bonded chain overrides any symmetry preference that the individual molecules may have (C_2 in this case).

No significant differences between equivalent bond lengths in structures **1** and **2** were observed (pyridine ring, amide groups), hence, the resonance stabilization effects do not seem to make the bond lengths in **1** more equivalent than in structure **2**. The aromatic C-C bond lengths in the crystal structure of **1** are all within 0.0014 Å of the reference value of 1.4 Å[85] (**Appendix A**). The aliphatic C-C bonds in the crystal structure of **2** are all within 0.0056 Å of the reference value of 1.54 Å[85] (**Appendix A**). For both structures **1** and **2** the standard deviation of the bond lengths of equivalently bonded atoms is low. However given the larger value of R^2 for compound **1** it is possible that the structure of **1** exhibits a greater degree of bond length variation.

3.2.2 Conformational diversity and literature comparisons

Two CSD searches for similar pyridine type, amide-containing ligands were performed. Table 3.1 summarizes the findings of this search. Only non-complexed forms of the ligands have been considered.



Scheme 3.2: Clarification of N-H hydrogen orientations and structures that were given as inputs for the CSD search.

Endo has been classified as the amide group (and as a result the amide hydrogen) being orientated towards the hemi-cavity, while an exo amide group is one that is not orientated towards the hemi-cavity, and as a result does not constitute being part of the “pincer”.

Table 3.1. Selected results of the search that was conducted; the input structure used in the search has been shown in Scheme 3.2.

Ref Code	C=O bond lengths (Å)	C(carbonyl)-N(amide) bond lengths (Å)	Conformation (with respect to amide groups)
ALOYIL[86]	1.220, 1.231	1.378, 1.342	*endo*|*endo*
ALOZEI[86]	1.222, 1.221	1.360, 1.360	*endo*|*endo*
ITUPOE[87]	1.239, 1.242	1.307, 1.339	*endo*|*endo*
NEDSAR01[86]	1.223, 1.223	1.359, 1.356	*endo*|*endo*
OTASIN[88]	1.228, 1.218	1.356, 1.356	*endo*|*endo*
COQFOF[89]	1.241, 1.226	1.331, 1.339	*endo*|*exo*
GOKFOB[90]	1.240, 1.225	1.317, 1.320	*endo*|*endo*
KERWIO[91]	1.236, 1.225	1.324, 1.328	*endo*|*endo*
MILHEV[92]	1.245, 1.243	1.352, 1.358	*exo*|*exo*
1*	1.223, 1.220	1.341, 1.343	*endo*|*endo*
2*	1.241, 1.237	1.337, 1.322	*endo*|*endo*

*Structures **1** and **2** are not found in the CSD, but were included for comparison.

The GOKFOB and ILORAE structures exhibit one-dimensional chain formation that is very similar to that of **2**, where in an almost identical fashion, the amide hydrogen had been swivelled away, allowing for strong classical hydrogen bonds to be formed.

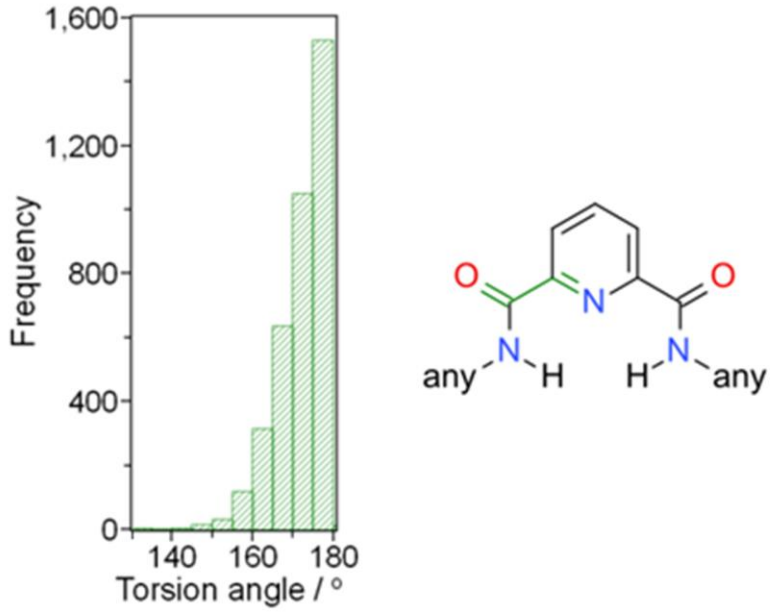


Figure 3.5. MOGUL search of the CSD (up to May 2017) mapping the range of N=C–C=O torsion angles (highlighted in green) in crystallographically characterized bis(amide)-pyridine pincer derivatives. Out of 3721 structures, only 6 have the highlighted torsion angle < 30°. The typical range is 140–180°, with the majority of structures exhibiting a torsion angle between 170–180°. The histogram has been constructed with a 5° bin width.

The results of the MOGUL search of the CSD (Figure 3.5) reveal a number of interesting features of the pincer compounds from the literature.

- Most of the structures deviating from the typical *endo*|*endo* conformation (both N=C–C=O torsion angles trans) are part of a more complex structure (e.g. a polyamide or macrocycle).
- Nearly all simple bis(amides) in this class exhibit endo|endo conformations in which the N=C–C=O torsion angle is close to 180°.
- The outliers (numbering fewer than 9 out of 3721 structures) with an exo|exo or exo|endo. These structures have been shown in Table 3.2.

Table 3.2. Outlier structures that were found during the the search of the CSD. These outliers exhibit *exo*|*exo* or *exo*|*endo* conformations, and their torsion angles have been listed.

Ref Code	N=C–C=O torsion angle (°)
CEFFUP[93]	2.4
MILHEV[92]	4.9
NARCER*	7.7
WANHUQ[94]	15.6
DAPVEW[95]	15.9
SAXFED[96]*	19.4
WENDEZ[97]	21.3
CEFFUP	26.7
COQFOF[89]	51.0

*Denotes non pincer ligands.

The most conspicuous outlier (MILHEV) has two independent molecules in the asymmetric unit, both with an exo|exo conformation that is undoubtedly stabilized by a pair of C=O···H(water) hydrogen bonds (Figure 3.6) involving a bound water molecule.

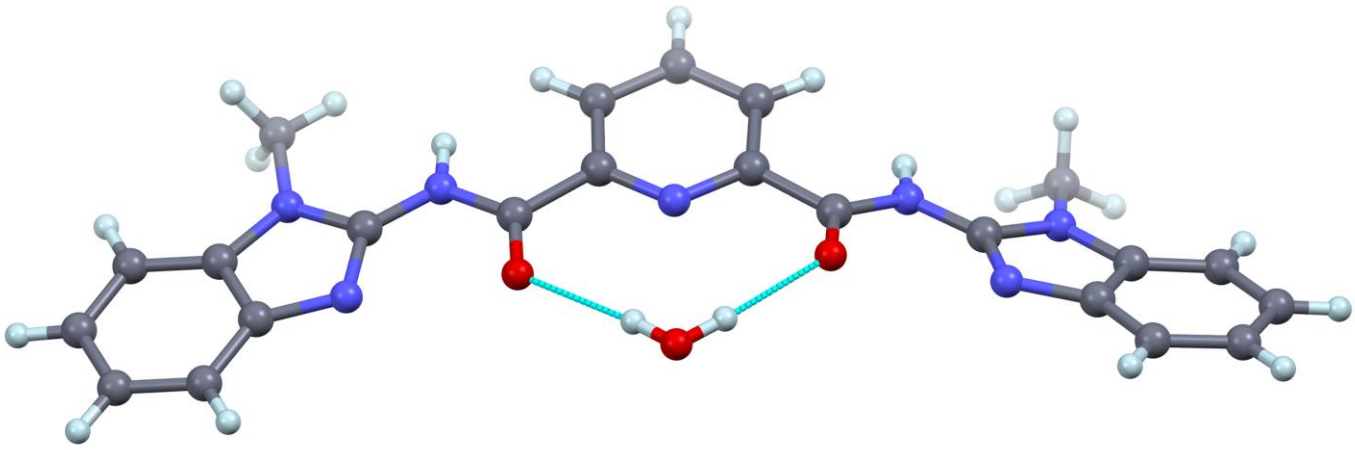


Figure 3.6. One of the independent molecules in the X-ray structure of MILHEV in which an *exo*|*exo* conformation for the bis(amide) system is stabilized by the two amide carbonyl oxygen atoms serving as H-bond acceptors to a water molecule.

Endo|*endo* cases constitute the vast majority of the ligand structures found in the CSD analysis, however chelated forms of the ligand that exhibit *endo*|*exo* and *exo*|*exo* conformations are found far more commonly than for the free ligand alone. (Figure 3.7, EQANOB[98] and FEKYIE[99]). It is important to note that many of the pincer-type ligands analysed in this CSD search have been synthesised for the purpose of metal binding. As a result the structures of this type that are found in the CSD have potentially been tweaked and optimized to bind metals very efficiently. This could have the effect of biasing the search

results to yield a disproportionately large number of ligands with a particular linkage isomerism. That said, the mechanism whereby a particular type of linkage isomer for this class of pincer ligands could be targeted would have to be known a *priori* in order to overcome serendipitous isolation of any of the three isomer types (Scheme 3.1). Our survey of the literature suggests that no deeper analysis of the underlying mechanism of conformational and linkage isomerism in this class of ligands exists, giving impetus to the current investigation.

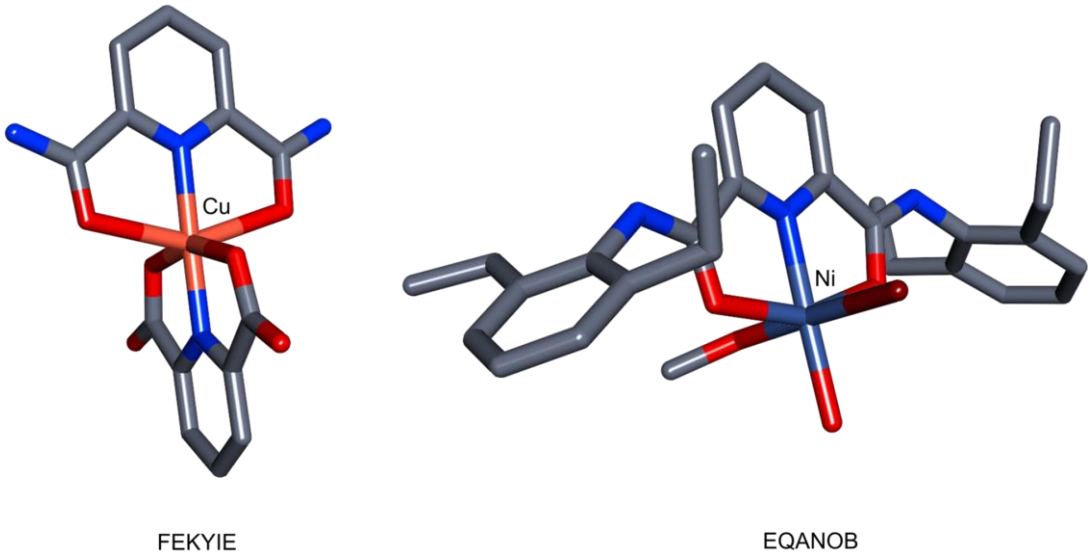


Figure 3.7: Crystal structures of EQANOB and FEKYIE. These are examples of coordination complexes which exhibit an *exo*|*exo* conformation (with respect to the amide group).

Overall, compounds **1** and **2** have very similar conformations, bond lengths and bond angles to similar ligands in the literature. The vast majority of the structures found in literature exhibit *endo*|*endo* conformation, with hydrogen atoms oriented towards the hemi-cavity in essentially the same way as in compounds **1** and **2**. The C=O and C(carbonyl)-N(amide) bond lengths in compounds **1** and **2** are in near-perfect agreement with the structures obtained from literature. The vast majority of literature structures have bond lengths that are in the 1.220 to 1.240 Å range (for C=O) and 1.324 to 1.378 Å (for $C_{(carbonyl)}$-$N_{(amide)}$). This result indicates that the presence of an aromatic vs aliphatic ring has little impact on the bond lengths, and orientations of the C=O and C(carbonyl)-N(amide) groups.

Table 3.3. Selected bond lengths, bond angles and torsions angles for various structures of interest.

Parameter	1	2	ALOYIL	KERWIO
N-H (Å)	0.880	0.880	0.880	0.821
N-H (Å)	0.880	0.881	0.881	0.844
C-N (Å)	1.341	1.337	1.342	1.328
C-N (Å)	1.343	1.322	1.378	1.324
C-N-H (°)	118.08	118.95	116.82	122.86
C-N-H (°)	118.53	118.85	117.93	120.94
O-C-N-H (°)	178.57	172.87	-178.27	175.55
O-C-N-H (°)	-173.17	-172.47	-176.35	-175.31

From the Table 3.3, it is clear that the compounds synthesised in this dissertation have remarkably similar structure features to many derivatives that are found in the literature (Figure 3.8). The structural differences are subtle and can be attributed to mostly crystal packing effects.

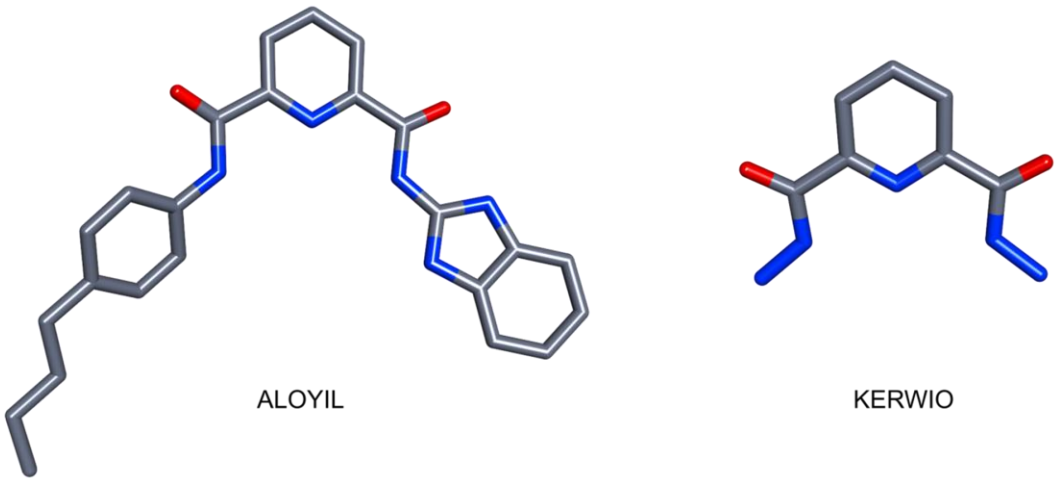


Figure 3.8: Crystal structures of ALOYIL and KERWIO. These are examples of literature pincer ligands, whose structure parameters closely match those of **1** and **2**.

3.2.3 Molecular Simulations

The DFT calculations (*in vacuo*) were performed using Gaussian 09W (WIN64)[100] at the HSEH1PBE/SDD[31] level of theory; the SDD basis set was chosen because it is widely used in calculations of coordination compounds due to its accuracy and speed, which is related to the use of

effective core potentials (ECPs) to treat the core electrons of heavy elements. In all cases, the nature of the stationary states located on the potential energy surface were validated using frequency calculations and were determined to be true minima where no negative frequency eigenvalues were observed. Population analysis of the final wave function, for each geometry-optimized structure, was performed using NBO 3.0[63] (running in Gaussian 09W).[100] The Laplacian of the electron density of bonds was calculated using AIMAII.[62]

Figure 3.9 shows a set of DFT-calculated MO (molecular orbital) diagrams for **1** and **2**. The HOMO and HOMO–1 orbitals of **1** are essentially degenerate (HOMO–1: -6.10 eV, HOMO: -6.09 eV, with $\Delta E_{(HOMO-HOMO-1)}$ = 0.012 eV). The HOMO and HOMO–1 orbitals of **2** are also essentially degenerate (HOMO -1: -6.78 eV HOMO: -6.75 eV, with $\Delta E_{(HOMO-HOMO-1)}$ = 0.026 eV). The extent of conjugation in **2** is less than for **1** and as a result the HOMO-LUMO gap of **2** is larger than **1**. This suggests that the Q-groups appended to the amide nitrogen atoms have a significant impact on the electronic structure of the ligand (as well as its steric bulk) and that variations in the Q-group may be used to control the redox properties of metal ions complexed by this class of pincer ligand. This has been used to good effect in catalysis by metal complexes of these ligands.[101-103]

3.2.4 HOMO-LUMO gap energies

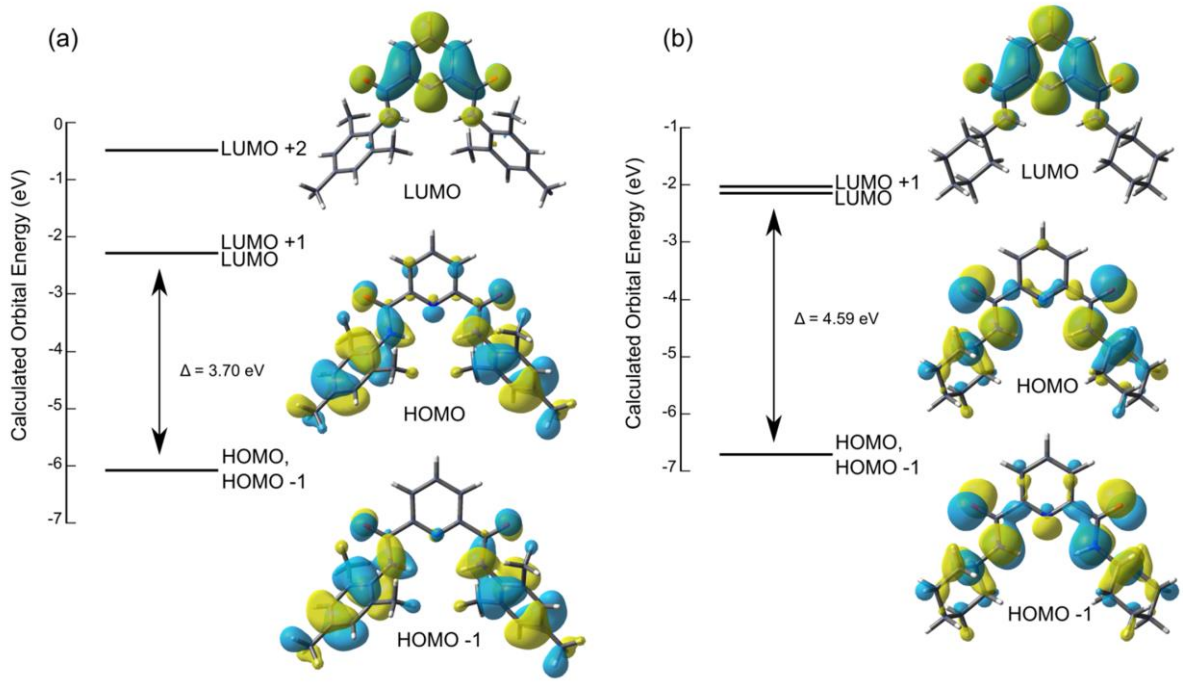


Figure 3.9. (a) DFT-calculated molecular orbital diagram for compound **1**. The HOMO-LUMO gap is 3.70 eV. (b) DFT-calculated molecular orbital diagram for compound **2**. The HOMO-LUMO gap is 4.59 eV.

In the DFT-calculated molecular orbital diagrams, it is seen that ligand **2** has a much larger HOMO-LUMO gap than ligand **1**, the difference being 0.89 eV. This difference is likely due to the greater degree of electron delocalization that is exhibited by the bis(mesityl) ligand. This extended delocalization is caused by the presence of the aromatic rings in the ligand. This same effect is not present for ligand **2** due to the aliphatic nature of the cyclohexyl rings. The results suggest that ligand **2** is more polarizable and is therefore softer than ligand **1**. Because Au(III) is a relatively hard metal ion, the data suggests that Au(III) might, in principle, bind more readily (chelate) to ligand **1** (where a more favourable $\Delta G_{(binding)}$ value will be obtained when using the harder cyclohexyl ligand, **2**). As a result we would overall expect the bis(mesityl) ligand **1** to be more suitable for the binding of softer metals, and the bis(cyclohexyl) ligand **2** to be more suited for the binding of harder metal ions. Pearson[104] states that a small energy gap leads to high polarizability, and a large energy gap leads to low polarizability. Hard molecules have larger HOMO–LUMO gaps. Hard molecules are also chemically less reactive because hardness is related to chemical stability. According to Pearson[104] Au(III) has an absolute hardness of 8.4 eV, putting it in a similar hardness range to borderline metal cations. While the Au(III) cation is not necessarily very hard, it is still much harder than Au^+ which is a soft cation, so it is of vital importance to differentiate between these two metal cations while considering factors relating to ligand binding. Thus it is possible

that ligand **2** being harder would preferentially bind to harder metal cations. A list of potential candidates has been selected from the work of Pearson[104] and has been presented in Table 3.4. A small HOMO–LUMO gap indicates that a molecule is soft. This is because the small energy gap between occupied and unoccupied orbitals contribute significantly the high polarizability of soft molecules.[24] According to HSAB theory, the harder ligand **2** would preferentially bind to Au(III), over the softer mesityl-containing ligand,

Table 3.4. A series of metal cations, and their predicted ligand binding preferences. Absolute hardness values are according to Pearson.[104]

Metal cation	Absolute hardness (eV)
Fe^{3+}	12.1
Cs^{+}	10.6
Co^{3+}	8.9
*Ni^{2+}	8.5
*Au^{3+}	8.4
*Pt^{2+}	8.0
*Pd^{2+}	6.8
*Rh^{+}	5.3
*Ir^{+}	3.9

*isoelectronic to Au^{3+}

Harder metals; will bind more readily to the harder ligand, **2**.



Softer metals; will bind more readily to the softer ligand, **1**.

1. However it is also noted that hard–hard interactions are primarily controlled by the charges of the interacting molecules, while soft–soft interactions are generally orbitally controlled.[24] This distinct difference in the modes of interaction make it very difficult to directly predict or categorize the nature of metal-to-ligand interactions based on HSAB theory alone. Notably, only ligand **1** has been chelated to Au(III), with ligand **1** having also been chelated to Pd(II). (X-ray data are presented for these structures in **Chapter 4**).

3.2.5 3-D Conformational analysis

From the analysis of the available conformational diversity in the CSD presented earlier, it is clear that metal chelates allow for multiple different 3-D conformations of this class of bis(amide) pincer ligand, suggesting that a more thorough analysis is required to fully probe the nature of the conformational space accessible by these ligands. In **Chapter 4** a similar conformational analysis has been performed on the Au(III) chelates.

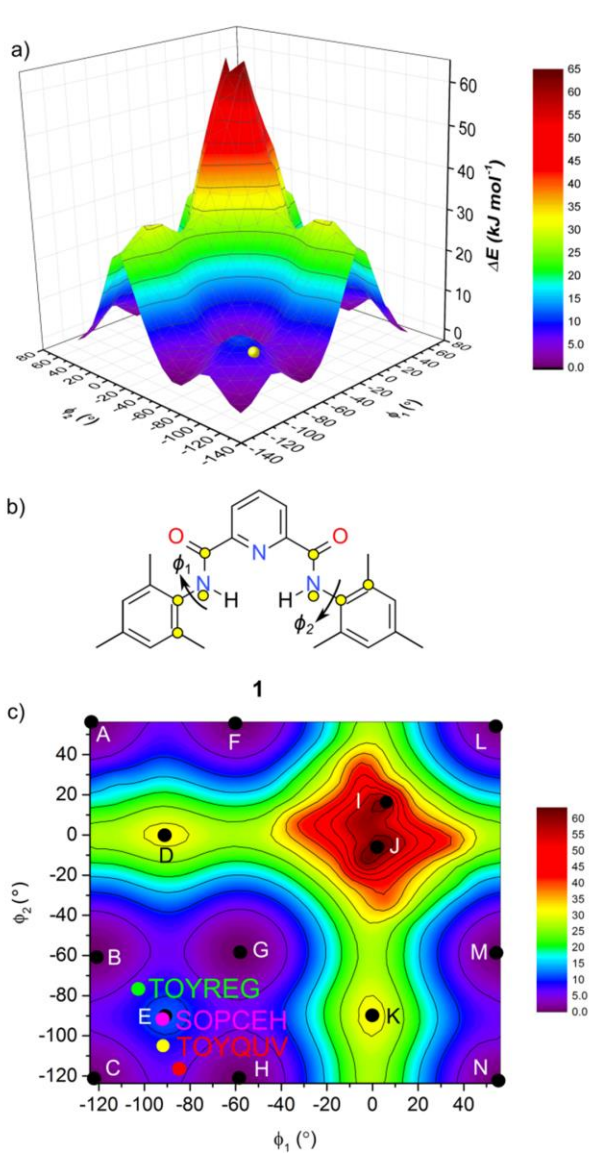


Figure 3.10. a) Three-dimensional plot showing the variation in the relative heat of formation, ΔE, of **1** as a function of the torsion angles ϕ1 and ϕ2. The angular coordinates locating the crystal structure are shown as a yellow sphere (ϕ1 = –91.8°, ϕ2 = –104.9°, ΔE = 8.8 kJ mol^{-1}).

b) Structure of **1** showing how torsion angles ϕ1 and ϕ2 have been defined.

c) Two-dimensional representation of a). The angular coordinates locating the crystal structure are shown as a yellow circle (ϕ1 = –91.8°, ϕ2 = –104.9°). Conformations of crystallographically-characterized examples from the CSD are shown along with their reference codes.

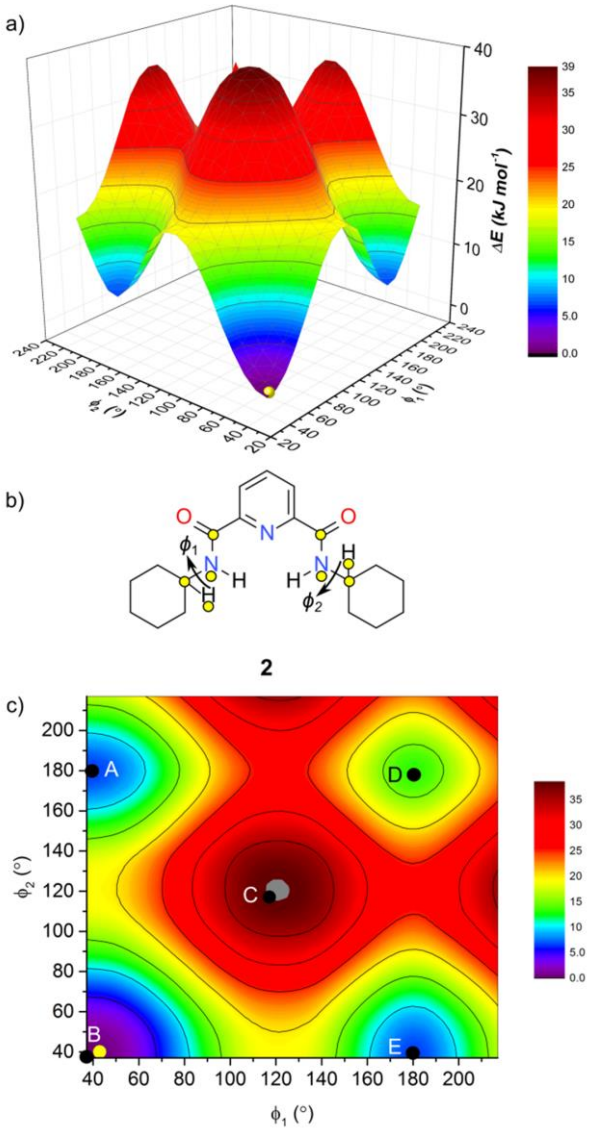


Figure 3.11. a) Three-dimensional plot showing the variation in the relative heat of formation, ΔE, of **2** as a function of the torsion angles ϕ1 and ϕ2. The angular coordinates locating the crystal structure are shown as a yellow sphere (ϕ1 = 42.9°, ϕ2 = 40.1°, ΔE = 0.1 kJ mol^{-1}).

b) Structure of **2** showing how torsion angles ϕ1 and ϕ2 have been defined.

c) Two-dimensional representation of a). The angular coordinates locating the crystal structure are shown as a yellow circle (ϕ1 = 42.9°, ϕ2 = 40.1°). Conformations of crystallographically-characterized examples from the CSD are shown along with their reference codes.

Discussion of **Figure 3.10:**

For the simulation shown in Figure 3.10, torsion angles ϕ1 and ϕ2 are taken to be about the amide nitrogen to the adjacent mesityl carbon bond (Figure 3.13 b). There are approximate symmetry planes about the ϕ1 or ϕ2 = -93.8°, -56.1°, -3.9°, 56.1°, and ϕ1 = ϕ2 axes. Points A, B, C, F, G, H, L, M and N are essentially degenerate and all have energies that are within 0.5 kJ mol^{-1} of the global minimum N (with the exception of G, which has an energy of 0.540 kJ mol^{-1}). The main energy barriers present on the conformational energy surface lie along the ϕ1 = -3.9° and ϕ2 = -3.6° axes. These barriers require approximately 30 kJ $mol^{-1}$of energy to overcome. The only reasonable conformations that can be accessed by crossing this barrier are conformers D and K. As a result these conformers are predicted to only be accessible at high temperatures. Table 3.6 shows three literature structures of metal complexes of **1**. All three of the structures have torsion angles that are similar to that of the crystal structure of **1**. This indicates that the torsion angles ϕ1 and ϕ2 do not change significantly when metal complexation occurs. It is worth noting that SOPCEH (Figure 3.10 c) lies essentially on the local maximum E, while TOYQUV (Figure 3.10 c) and TOYREG (Figure 3.10 c) lie on the saddle points between the global minima and the local maxima E, in much the same way that the crystal structure of **1** does. It is possible that conformer E is more structurally stable than what is predicted by DFT. This could be due to packing or lattice effects in the crystal structure that that were not taken into account for by the simulation (because simulations are performed in *vacuo*). It is possible that these lattice effects add stability to the conformer which make it more favourable for the conformer to pay the energy penalty and deviate from the predicted global minimum thereby gaining additional stability.

Table 3.5. Structural details and parameters of the conformers shown in **Figure 3.10.**

	ϕ1 (°)	ϕ2 (°)	ΔE (kJ mol^{-1})	Assignment
A	-123.9	56.4	0.0	Global minimum
B	-123.9	56.4	0.0	Global minimum
C	-123.9	-123.6	0.1	Global minimum
D	-93.9	-3.6	30.7	Local maximum – on saddle point
E	-93.9	-93.6	11.0	Local maximum – on saddle point
F	-63.9	56.4	0.3	Global minimum
G	-63.9	-53.6	0.5	Global minimum
H	-53.9	-123.6	0.3	Global minimum
I	6.1	16.4	63.3	Global maximum
J	6.1	6.4	52.8	Local maximum

K	-3.9	-93.6	30.9	Local maximum – on saddle point
L	56.1	56.4	0.1	Global minimum
M	56.1	-53.6	0.3	Global minimum
N	56.1	-123.6	0.0	Global minimum

Table 3.6. Structural details and parameters of the literature conformations shown in **Figure 3.10.**

Ref Code	Metal	ϕ1 (°)	ϕ2 (°)
SOPCEH	Au	-91.8	-90.8
TOYQUV	Ni	-115.3	-84.6
TOYREG	Ni	-75.9	-101.4

*TOYREG: [64], TOYQUV: [64], SOPCEH: [74]

Discussion of **Figure 3.11**

Torsion angles ϕ1 and ϕ2 in this simulation are taken to be about the amide nitrogen to the adjacent cyclohexyl carbon bond (Figure 3.11 b). **1** is novel and so no metal complexes of this ligand are available for comparison or analysis. Approximate mirror symmetry is observed along the ϕ1 or ϕ2 = 177.1°, 117.1°, 37.1° and the ϕ1 = ϕ2 axes. The 3D surface plot shows that the energy of the crystal structure (calculated by freezing torsion angles ϕ1 and ϕ2 and performing an energy optimizing DFT calculation) is in good agreement with the energy of the value at the same ϕ1 and ϕ2 points on the surface. The energies of local minima A and E are within 0.1 kJ mol^{-1} of each other and are thus essentially degenerate and isoenergetic. These conformers are approximately 6.5 kJ mol^{-1}higher in energy than conformer B, the lowest energy conformer. A high energy conformer also exists at point D (a high energy local minima), however two separate energy barriers (e.g B to A to D, an overall barrier of ~30 kJ mol^{-1}) need to be overcome achieve this conformer, making it an energetically disfavoured structure. Thus the conformer at E is likely to only be accessed at high temperatures.

Table 3.7. Structural details and parameters of the conformers shown in **Figure 3.11:**

	ϕ1 (°)	ϕ2 (°)	ΔE (kJ mol^{-1})	Assignment
A	37.1	177.1	6.5	Local minimum
B	37.1	37.1	0.0	Global minimum
C	117.1	117.1	38.5	Global maximum
D	177.1	37.1	6.5	Local minimum
E	177.1	177.1	13.3	Local minimum

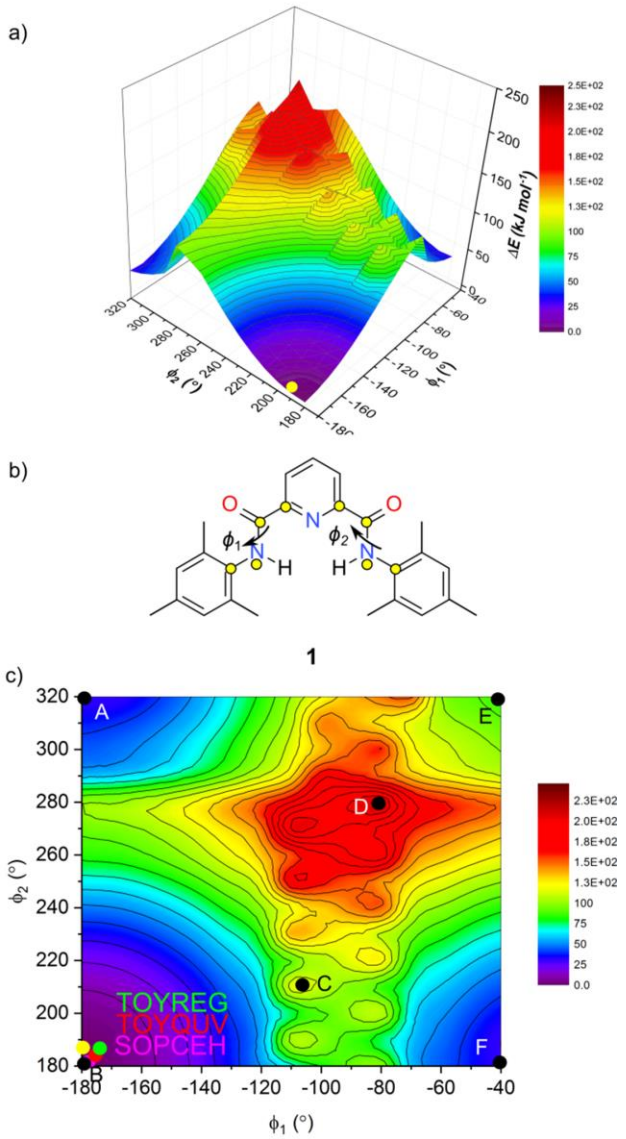


Figure 3.12. a) Three-dimensional plot showing the variation in the relative heat of formation, ΔE, of **1** as a function of the torsion angles ϕ1 and ϕ2. The angular coordinates locating the crystal structure are shown as a yellow sphere (ϕ1 = -178.0°, ϕ2 = 173.0°, ΔE = -0.8 kJ mol^{-1}).

b) Structure of **1** showing how torsion angles ϕ1 and ϕ2 have been defined.

c) Two-dimensional representation of a). The angular coordinates locating the crystal structure are shown as a yellow circle (ϕ1 = 170.5°, ϕ2 = -171.2°)**.** Conformations of crystallographically-characterized examples from the CSD are shown along with their reference codes.

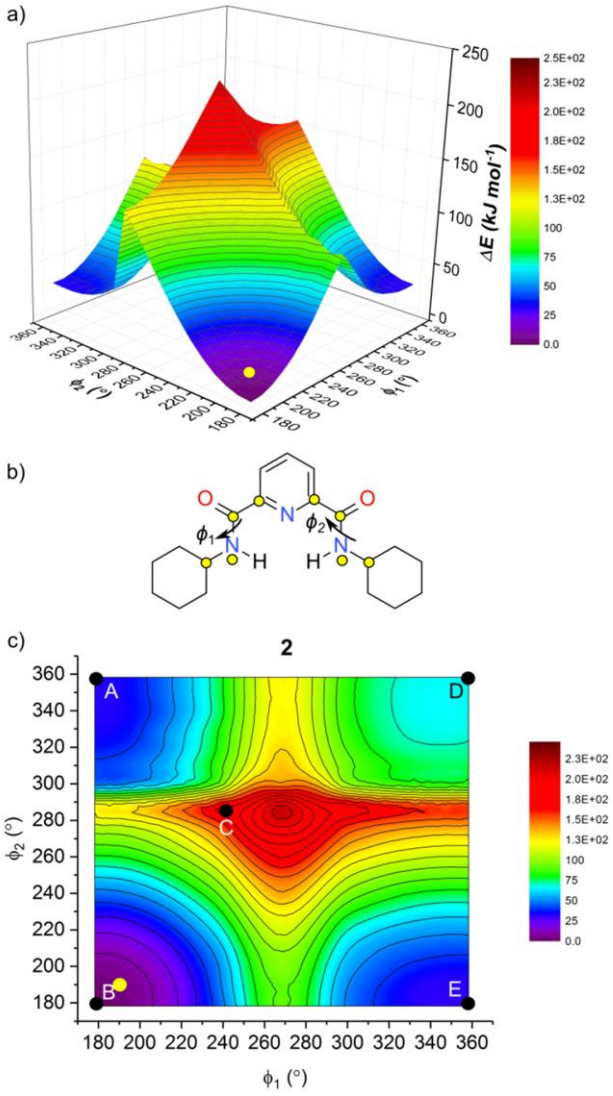


Figure 3.13. a) Three-dimensional plot showing the variation in the relative heat of formation, ΔE, of **2** as a function of the torsion angles ϕ1 and ϕ2. The angular coordinates locating the crystal structure are shown as a yellow sphere (ϕ1 = 170.6°, ϕ2 = -171.2°, ΔE = 1.7 kJ mol^{-1}).

b) Structure of **2** showing how torsion angles ϕ1 and ϕ2 have been defined.

c) Two-dimensional representation of a). The angular coordinates locating the crystal structure are shown as a yellow circle (ϕ1 = 170.6°, ϕ2 = -171.2°).

Discussion of **Figure 3.12:**

Torsion angles ϕ1 and ϕ2 are taken to be about the carbonyl carbon to the amine nitrogen bond (Figure 3.12 b). A and F are points of local minima, D is the global maximum and B is the global minimum. Point C represents a saddle point between minima B and F, approximately ~90 kJ mol mol^{-1}is required to overcome this energy barrier. Unlabelled saddle points are also present between minima A to B (~110 kJ mol mol^{-1}), A to E (~125 kJ mol^{-1}) and F to E (~190 kJ mol^{-1}). Several symmetry elements are present in the conformer map. There is approximate symmetry about the ϕ1 = 95° axis, the ϕ2 = 275° axis and the ϕ1 = (360° - ϕ2) axis. The position of the crystal structure, literature structures TOYREG, TOYQUV and SOPCEH are all clustered close to the global minimum B. This shows that there is strong agreement between the DFT-calculated low-energy conformer, the conformation of the crystal structure and the conformation of complexed forms of the ligand. The DFT calculated energy of the crystal structure was ΔE = -0.1 kJ mol^{-1}, making it very close in energy to the predicted low energy conformer B (ΔE = 0.0 kJ mol^{-1}). The general topology of the PES is remarkably similar to that of the bis(mesitylamide) ligand, except ϕ1 and ϕ2 are interchanged.

Table 3.8. Structural details and parameters of the conformers shown in **3.12**

	ϕ1 (°)	ϕ2 (°)	ΔE (kJ mol^{-1})	Assignment
A	-180.0	320.0	31.0	Local minimum
B	-180.0	180.0	0.0	Global minimum
C	-110.0	210.0	119.4	Saddle point between B and F
D	-80.0	280.0	214.8	Global maximum
E	-40.0	320.0	84.9	Local minimum
F	-40.0	180.0	31.0	Local minimum

Table 3.9. Structural details and parameters of the literature conformations shown in Figure **3.12**

Ref Code	Metal	ϕ1 (°)	ϕ2 (°)
SOPCEH	Au	180.0	180.0
TOYQUV	Ni	-179.6	-176.4
TOYREG	Ni	-175.3	176.2

*TOYREG: [64], TOYQUV: [64], SOPCEH: [74]

A similar ligand-metal complex comparison was not performed for ligand **2** because no chelated forms of **1** have been reported in the literature.

Discussion of **Figure 3.13:**

Torsion angles ϕ1 and ϕ2 are taken to be about the carbonyl carbon to the amine nitrogen bond (Figure 3.13 b). A, E and F are points of local minima, C is the global maximum and B is the global minimum. Unlabelled saddle points are present between minima A to B, with ~130 kJ mol^{-1} being required to overcome this energy barrier, A to D (~130 kJ mol^{-1}), B to E (~105 kJ mol^{-1}) and D to E (~200 kJ mol^{-1}). Several symmetry elements are present in the conformer map. There is approximate symmetry about the ϕ1 = 268.3° axis, the ϕ2 = 288.3° axis and the ϕ1 = ϕ2 axis. The crystal structure lies very close to the global minimum B. This shows that there is strong agreement between the DFT-calculated low-energy conformer and the conformation of the crystal structure as it was obtained in this study. The DFT calculated energy of the crystal structure was ΔE = 1.7 kJ mol^{-1}, making it very close in energy to the predicted low energy conformer B (ΔE = 0.0 kJ mol^{-1}).

Table 3.10. Structural details and parameters of the conformers shown in **Figure 3.13**

	ϕ1 (°)	ϕ2 (°)	ΔE (kJ mol^{-1})	Assignment
A	178.3	358.3	33.4	Local minimum
B	178.3	178.3	0.0	Global minimum
C	248.3	288.3	245.4	Global maximum
D	358.3	358.3	67.3	Local minimum
E	358.3	178.3	30.7	Local minimum

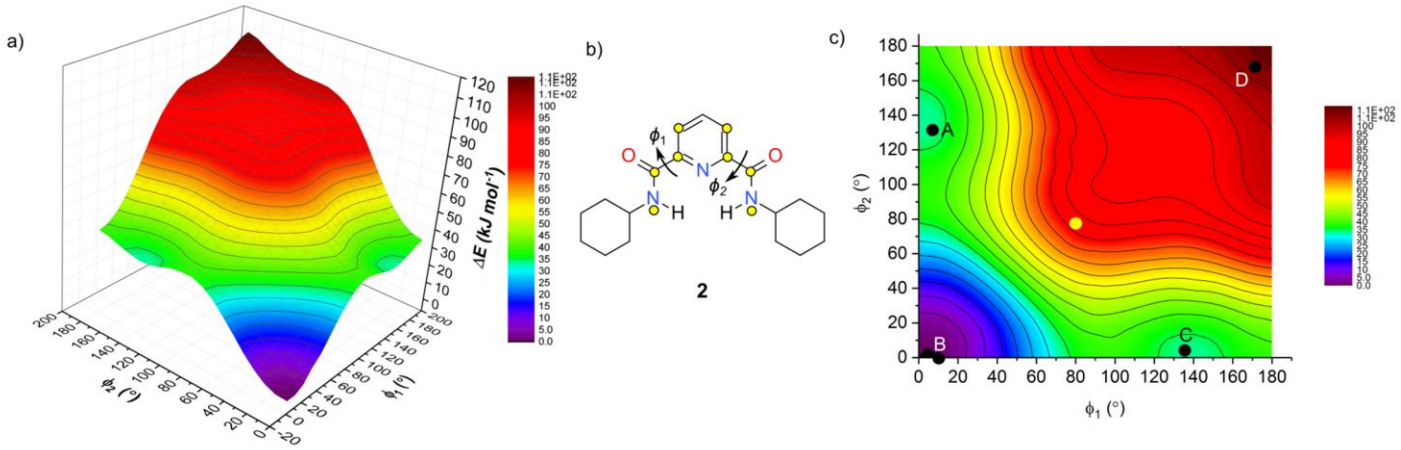


Figure 3.15. a) Three-dimensional plot showing the variation in the relative heat of formation, ΔE, of **1** as a function of the torsion angles ϕ1 and ϕ2. The angular coordinates locating the crystal structure are shown as a yellow sphere (ϕ1 = -83.7°, ϕ2 = -86.4°, ΔE = -0.8 kJ mol^{-1}).

b) Structure of **2** showing how torsion angles ϕ1 and ϕ2 have been defined.

c) Two-dimensional representation of a). The angular coordinates locating the crystal structure are shown as a yellow circle (ϕ1 = -83.7°, ϕ2 = -86.4°). Conformations of crystallographically-characterized examples from the CSD are shown along with their reference codes.

Discussion of **Figure 3.15:**

Torsion angles ϕ1 and ϕ2 are taken to be about the amide nitrogen to the adjacent cyclohexyl carbon bond (Figure 3.15 b). A and C represent points of local minima, D is the global maximum and B is the global minimum. Unlabelled saddle points are present between minima A to B and B to C. In both cases ~50 kJ mol^{-1} of energy is required to overcome these barriers. The conformer plot is symmetric about the ϕ1 = ϕ2 axis. The position of the crystal structure lies significantly far away from the global minimum B, at a very high predicted energy (78.2 kJ mol^{-1}) on the conformer plot. This is seemingly contradicted by its very low DFT-calculated energy of ΔE = -0.8 kJ mol^{-1}. This seeming paradox occurs because of the

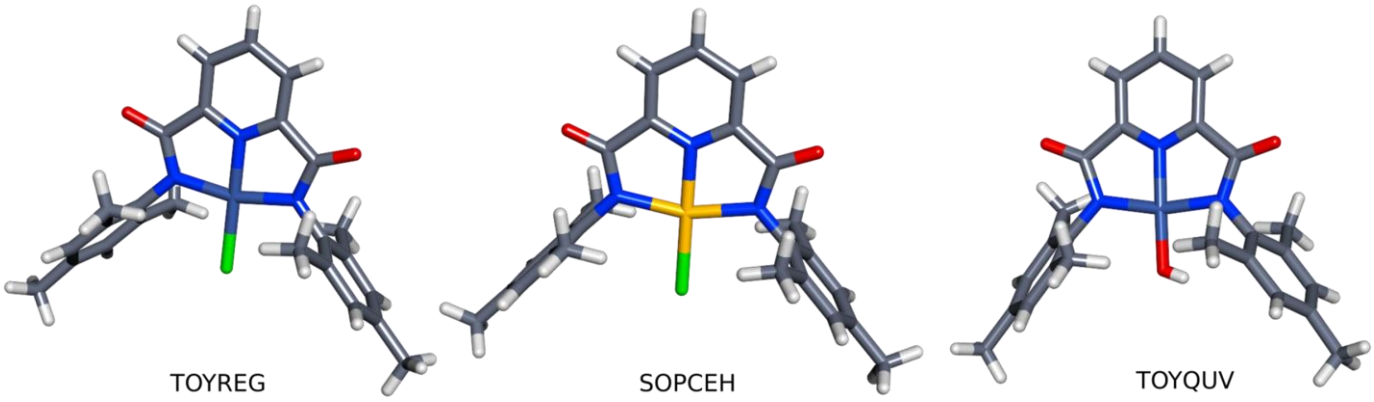


Figure 3.14. Crystal structures of TOYREG, TOYQUV and SOPCEH. TOYREG and TOYQUV are Ni(II) chelates of **1** and SOPCEH is a Au(III) chelate of **1**. The locations of the conformations of these structures on the surfaces shown in Figures 3.10 and 3.11 are indicated.

extensive one-dimensional dimerization that occurs in the solid state. The cyclohexyl ring has to shift to an energetically disfavoured orientation in order to allow for the hydrogen bonding chain to occur. In doing so the structure pays an energy penalty, yet gains structural stability due to the additional stabilization provided by the hydrogen bonding. This additional stabilization makes the resultant structure have greater stability than predicted. As has been stated before packing effects are not taken into account for DFT calculations, because calculations were performed in *vacuo*. The global minimum for the DFT-calculated surface has an *endo*|*endo* conformation with the N-H groups pointing inward to the metal-binding site (hemi-cavity) and the amide carbonyl C=O groups pointing out (*exo*|*exo*). This, in the case of the mesityl system, explains why most metal chelates of this type of pincer ligand exhibit the *endo*|*endo* conformation.

Table 3.11. Structural details and parameters of the conformers shown in **3.15**

	ϕ1 (°)	ϕ2 (°)	ΔE (kJ mol^{-1})	Assignment
A	0.0	140.0	33.0	Local minimum
B	10.0	0.0	0.0	Global minimum
C	140.0	0.0	33.4	Local minimum
D	180.0	180.0	112.1	Global maximum

There was good agreement between the crystal structure, and the global energy minima that were calculated by the torsion scan (Figure 3.16). The torsion angles of one of the global energy minimum conformers (E) had very similar torsion angles to that of the crystal structure of **1**, with the structures having a SI of 95.26 %. The torsion angles of global energy-minimum conformer B were also very similar to that of the crystal structure of **2**. The structures have a SI value of 91.62 %.

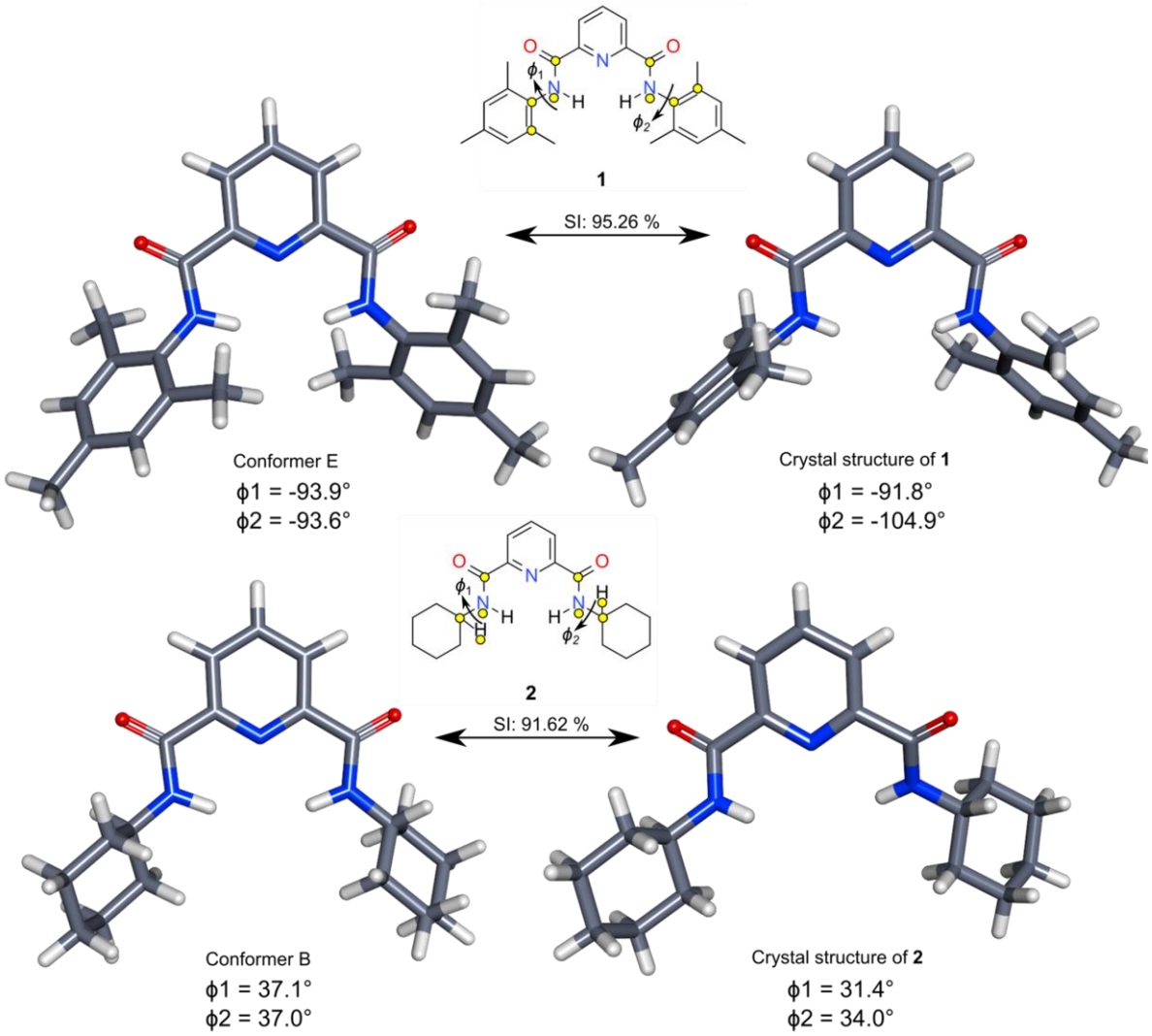


Figure 3.16. Conformational comparison between the global energy minimum conformer E (Scan 1, Figure 3.10), and the crystal structure of **1**, and the Conformational comparison between the global energy minimum conformer B (Scan 1, Figure 3.11) and the crystal structure of **2**.

3.2.6 Solution ^{1}H NMR studies

Compound **2** was studied as a function of concentration and by dynamic NMR (DNMR) in order to garner experimental evidence for intermolecular hydrogen bonding and any feasible conformational interconversions, such as rotation of the cyclohexyl groups, given the nature of the PES calculated by DFT methods in Figure 3.8. The DFT results clearly indicated that the *in vacuo* barrier to this process is around 20 kJ mol^{-1} for the N=C-C=O torsion angles involving the pyridine ring, suggesting that experimental observation of the process might be feasible. Dynamic NMR experiments were performed using DMSO-d_6 and $CDCl_3$ solvents. DMSO-d_6 was used for high temperature experiments (293.15 K to 388.15 K), while $CDCl_3$ was used for low temperature experiments (213.15 K to 283.15 K).

3.2.6.1 1H NMR study as a function of [2]

Figure 3.18 shows the results of a constant temperature ^{1}H-NMR experiment that was performed on **2** using concentrations ranging from 0.0051 M to 0.2024 M. This experiment was hampered by solubility issues where no limiting signal shift (i.e., saturation point) was observed even at the upper end of the concentration range that was used. It was observed that increasing the concentration beyond 0.2024 M resulted in significant precipitation within the NMR tube at room temperature. However this experiment did prove that the one-dimensional hydrogen bonding that is seen in the solid state (crystal structure) of **2** is also seen in the liquid state. There was a 0.2 ppm shift when increasing concentration, which is enough of a shift to show that some sort of self-assembly occurs in solution. When this data was plotted, it was determined that the ΔG value was negative (-0.02 kJ mol^{-1}), and therefore the self-assembly of **2** in solution is just spontaneous. The model used for this determination can be found in **Appendix A**. It was also observed that as concentration was increased, the N-H proton resonance sharpens (evidenced by narrower linewidths of the signals). This is evidence for the formation of an H-bonded assembly involving the N-H groups as the equilibrium shifts from monomers to higher H-bonded oligomers.[105]

The overall results of this variable concentration NMR experiment are limited because only two solvents have been used (DMSO-d_6 and $CDCl_3$) and it is known that solvents can affect the nature of one-dimensional chain assembly, since certain solvents may compete for H-bonding sites. It is possible that when a less polar solvent is used there will be less competition with hydrogen bonding from the solvent, and therefore dimerization might be more pronounced. It has also been documented that solvents have an effect on the barrier of C-N bond rotation.[106] These limitations aside, the experiments were able to confirm self-assembly of **2** in fluid solution to give a structure that might be consistent with that observed crystallographically (Figure 3.2).

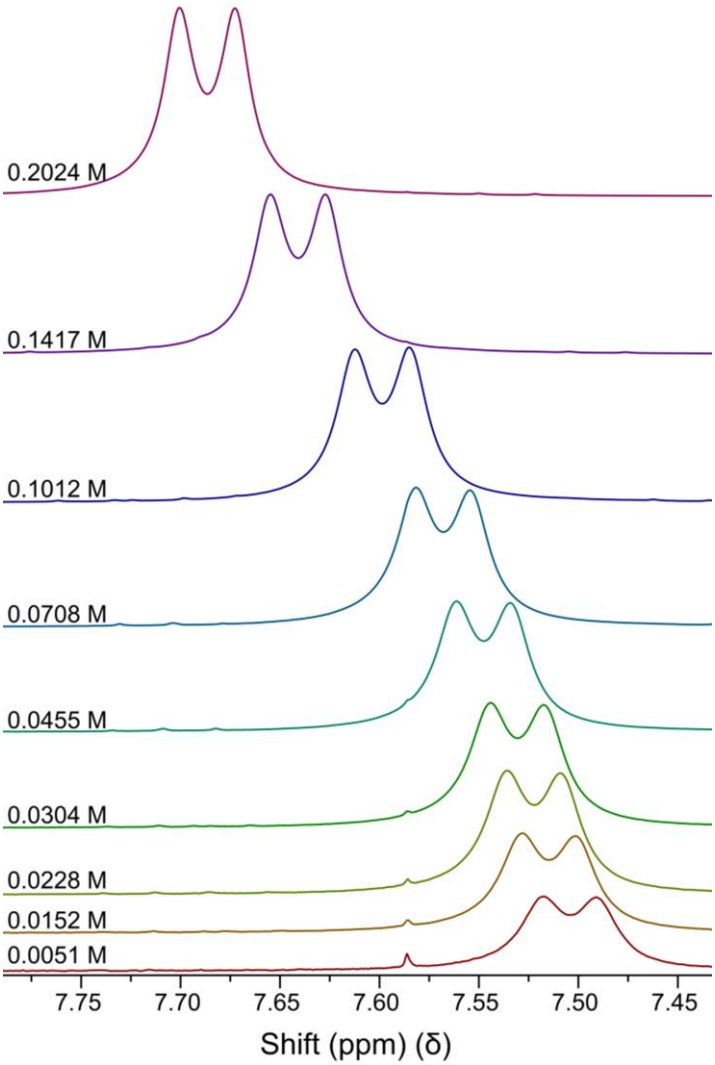


Figure 3.17. Variable concentration ^{1}H NMR spectra, taken at a constant temperature of 293.15 K. The plot shows the downfield shift of the N-H amide peak with increasing concentration.

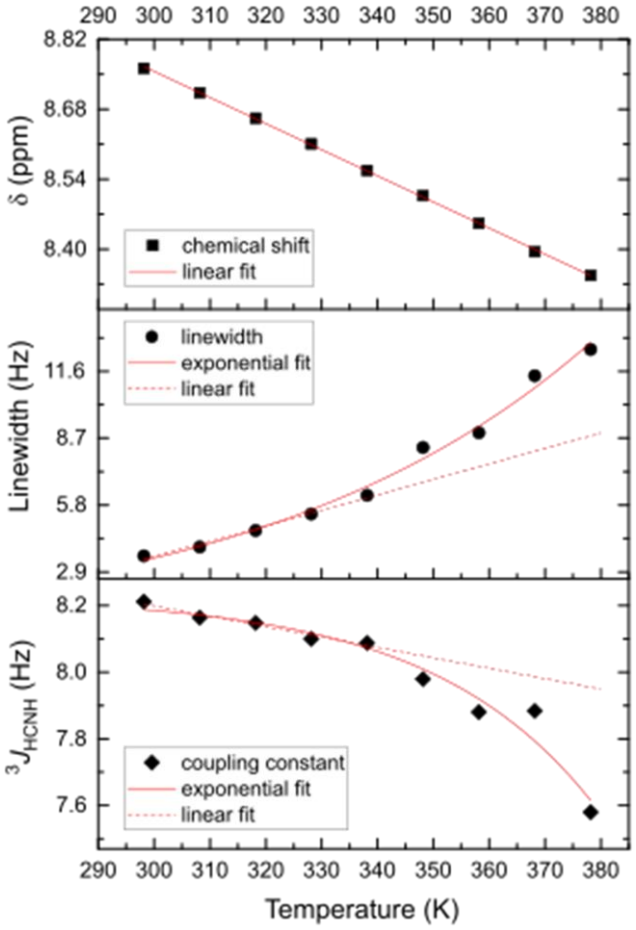


Figure 3.18. Plots of temperature vs ^{3}J(HCNH), linewide and shift value for the variable temperature ^{1}H NMR experiment. This study was performed at a constant concentration of 0.0228 M.

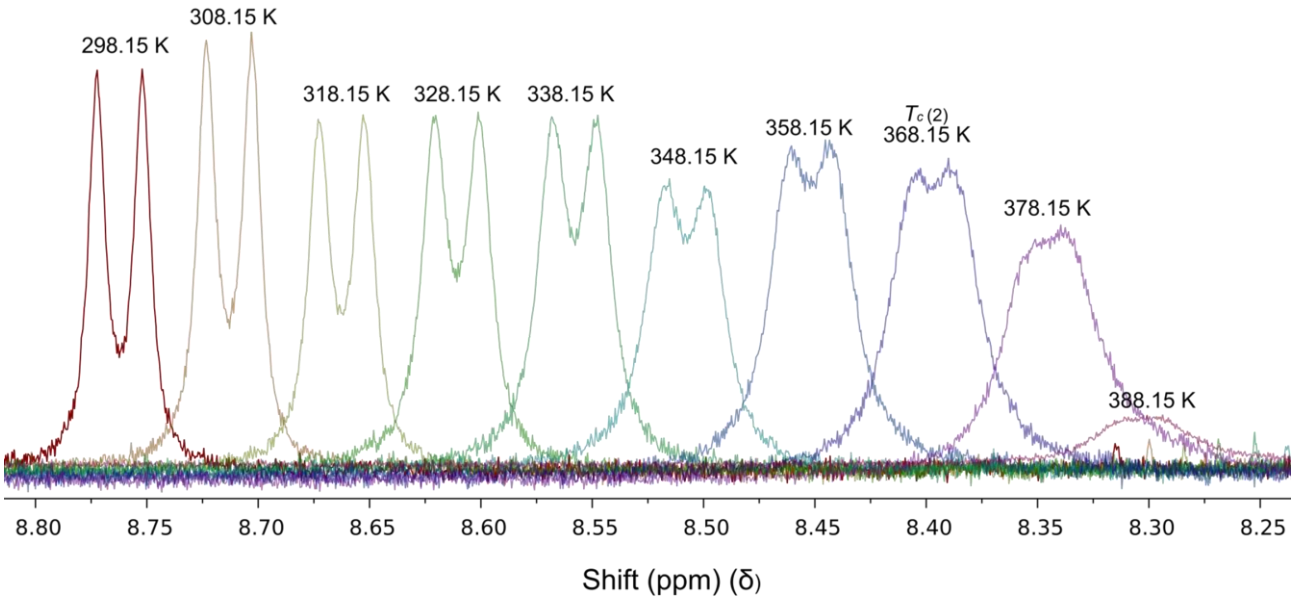


Figure 3.19. Variable temperature ^{1}H NMR spectra, taken at a constant concentration of 0.0228 M. The plot shows the downfield shift of the N-Hamide peak. The temperature range for the experiment was 298.15 K to 388.15 K, with spectra recorded at 10 K intervals. The *Tc*(2) value is at 378.15 K

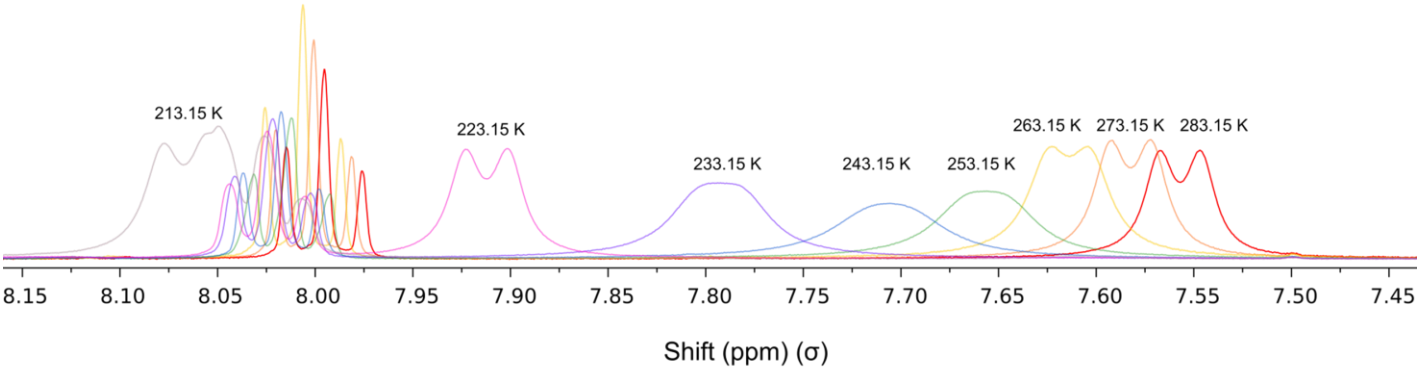


Figure 3.20. Variable temperature ^{1}H NMR spectra, taken at a constant concentration of 0.0228 M. The temperature range for the experiment was 288.15 K to 213.15 K, with spectra recorded at -10 K intervals. The plot shows the downfield shift of the N-Hamide peak.

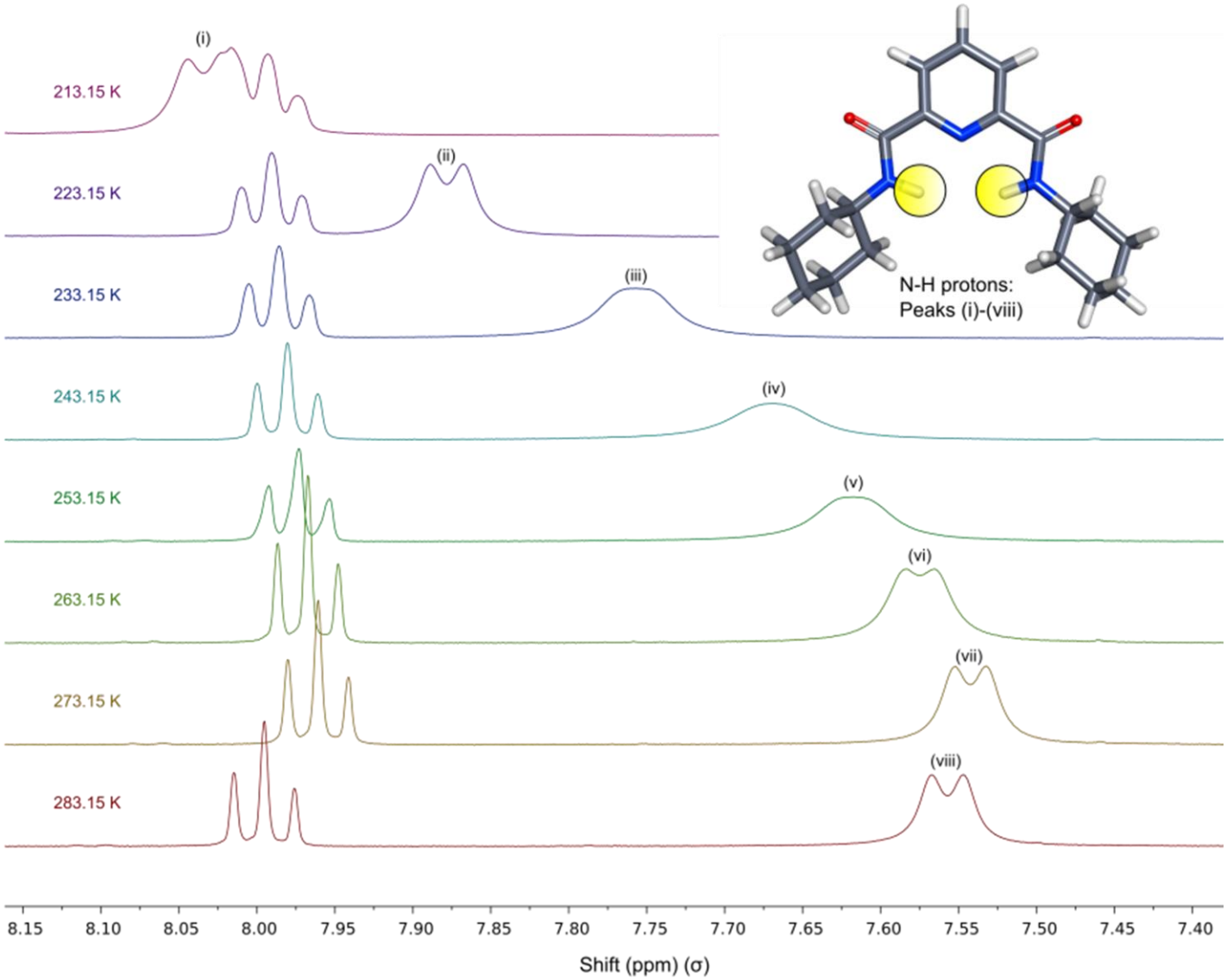


Figure 3.21. Variable temperature ^{1}H NMR spectra, taken at a constant concentration of 0.0228 M. This is a stacked view of the data presented in previous Figure 3.20. The temperature range for the experiment was 288.15 K to 213.15 K, with spectra recorded at -10 K intervals. The plot shows the downfield shift of the N-Hamide peak. N-H peaks have been labelled (i) to (viii).

3.2.6.2 Dynamic ^{1}H NMR study of 2 at T < 285.15 K

The low-temperature DNMR spectra for compound **2** are shown in Figures 3.20 and 3.21. The amide NH proton resonance appears as a doublet (8.035 ppm) overlapping the para-CH proton signal from the pyridine ring at 213.15 K (i). On warming, the NH proton resonance shifts upfield to 7.541 ppm (vii, 273.15 K), before shifting downfield to 7.557 ppm at 283.15 K (viii). The linewidth of the signal broadens monotonically with increasing temperature until signal coalescence is observed (243.15 K, iv). Thereafter, the linewidth sharpens with further warming. From the coalescence temperature (T_c), eqs 3.1-3.3 below may be used to determine the free energy of activation for the dynamic process, ΔG. Notably, the system is in the slow exchange limit at 213.15 K (relatively sharp linewidths), but clearly switches fully to the fast exchange limit at 283.15 K (sharpest linewidths). The terms in equations 3.1-3.3 are defined as follows: k^1 is the exchange rate constant, $\Delta\nu$ is the peak separation in the slow exchange limit, K is the equilibrium constant, k is the rate of the exchange, T is the temperature, T_c is the coalescence temperature, R is the gas constant, h is Plank's constant, $\Delta G^{\ddagger}$ is the free energy of activation for the process.

Discussion of Figure 3.21:

(i): This is the N-H amide peak that represents the slow exchange limit of the system. The signal is a doublet (8.035 ppm) that slightly overlaps with the para-hydrogen (position 4 on the pyridine ring) peak at ~7.980 ppm. Only one N-H conformer is likely populated at this low temperature.

(ii): As the solution is warmed the N-H amide doublet shifts further upfield to a position at 7.878 ppm. This is a significant peak shift and the N-H proton becomes more shielded.

(iii): At 243.15 K the N-H amide coalescence temperature has been reached. The signal coalesces to form a discrete singlet at 7.755 ppm. This is the key temperature information needed to calculate ΔG, as T_c(1) is now known.

$$k^1 = \frac{\pi \Delta \nu}{\sqrt{2}}$$

3.1

$$k^1 = K \frac{kT}{h} \exp\left(\frac{-\Delta G\ddagger}{RT}\right)$$

3.2

$$\Delta G \ddagger = 2.303RT_c(10.319 - \log_{10} k^1 + \log_{10} T_c)$$

3.3

Using these equations the ΔG value of the energy barrier was calculated to be 50.9 kJ mol^{-1} (T_c(1)) and 84.0 kJ mol^{-1} (T_c(2)). This is a similar result to the *in vacuo* DFT calculation that estimated this energy barrier to be between 20 and 40 kJ mol^{-1}. A possible reason for the lower DFT results could be due to the one-dimesional hydrogen bonding, present between molecules of this ligand, which are not taken into account for the DFT calculations.

The N-H signal for the amide proton is a doublet due to ^3J coupling with the methine C-H proton of the cyclohexyl ring. As a result, once the system is in the region of the fast exchange limit, the doublet signal can shift and the individual peak can broaden, but no further coalescence will be seen unless a higher-energy barrier is crossed. In the slow exchange limit, the conformation adopted will likely correspond to the global minimum energy conformation of **2** calculated *in vacuo* (Figure 3.22).

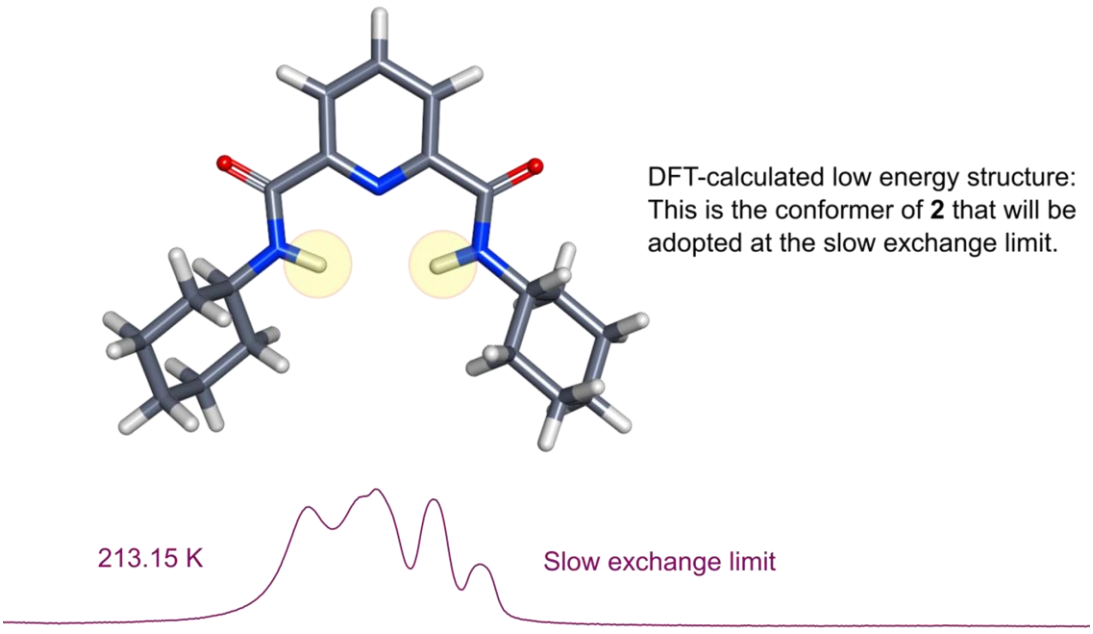


Figure 3.22.Low energy DFT calculated structure of **2**. At the slow exchange limit (213.15 K) this is likely the only conformer that will be adopted by the system.

The signal linewidth will be relatively narrow, but broadened somewhat by slow tumbling of the system in the cold, more viscous solvent. On warming, the system will cross any low energy barriers (Figure 3.10) interlinking local minima A and E with the global minimum (B) on the energy surface. From the conformational energy map, the saddle points (ϕ1 and ϕ2 = ~120°) have barriers of 20-30 kJ mol^{-1} and likely represent the barriers correlating with the DNMR barrier crossed at 243.15 K. At the barrier crossing, the linewidth of the NMR signal is broadened by the exchange process to the extent that the *J*-coupling is unresolved. In the fast exchange limit, all the low-lying conformers are populated and the narrow linewidth for the weighted average conformer in solution permits resolution of the *J*-coupling such that the doublet signal re-appears above 273.15 K. The signal is at a different chemical shift due to the general temperature dependence of the shielding for the protons in the molecule and the fact that the weighted average structure represents an average of all the populated minima (as opposed to just the global minimum at 213.15 K). It is also possible that concurrent rotation about the $C_{(alpha)}$-$C_{(carbonyl)}$ bond in **2** (Figure 3.15) occurs since the barrier to this process in the gas phase is only around 45 kJ mol^{-1} from our analysis of the PES for the system. The minima that would form part of the weighted population average in the fast exchange regime are labelled A and C in Figure 3.15, corresponding to tilted *exo*|*endo* conformers with ϕ1 = ~140° and ϕ2 = ~0°. This information suggests that the domination of *endo*|*endo* conformers in crystal structures of this class of ligands (Figure 3.5) is due to the *endo*|*endo* conformation being more favourable for coordination to most metal ions, and that there is a preference for *endo*|*endo* over *endo*|*exo* conformers in metal-free systems, with the *endo*|*endo* conformation being approximately 30 kJ mol^{-1} more energetically favoured. The DNMR study of **2** at higher temperatures (Figures 3.17 and 3.19) shows the normal behaviour of an upfield shift in the signal with increasing temperature. One further signal coalescence is observed at 378.15 K intensity loss and broadening due to thermal smearing of the linewidthis also evident. From equation 3.3, the second barrier has ΔG = 84.0 kJ mol^{-1}. This suggests that only one other barrier is crossed in the temperature range investigated (at 378.15 K), consistent with the fact that Figure 3.13 reflects a barrier height approaching 100 kJ mol^{-1} for rotation about the $C_{(carbonyl)}$-$N_{(amide)}$ bond.

Various studies have quantified the energy of the barrier to the internal rotation of amides in a number of compounds. The values can be highly variable, because they depend on the environment that the amide group is in. For example the barrier energy of internal rotation about the C-N(amide) is 40.6 kJ mol^{-1} in oxamide[107], 100.4 kJ mol^{-1} in dithiooxamide[107], 80.3 kJ mol^{-1} in formamide[108] and 64.4 kJ mol^{-1} in acetamide.[109] A highly relevant compound for comparison is N-methylacetamide (in $CHCl_3$), because the amide environment in this compound is very similar to that of **2,** and thus by comparing the energy barriers in these two compounds, many structural variables will be controlled for. In N-methylacetamide, the energy barrier of the rotation of the C-N(amide) bond is 86.6 kJ kJ mol^{-1}.[110] This energy barrier is in

very good agreement to the energy barrier calculated for the C-N bond rotation in compound **2** (84.0 kJ mol^{-1}). The minor energy difference is likely due to the increased bulk of ligand **2** when compared to the relatively sterically unencumbered N-methylacetamide.

It should be noted that the system is very complicated, and that it is possible that more experimental evidence is required to fully support some key points in this section. Obtaining ^{13}C DNMR data for the system is of vital importance in this regard; however such an analysis is currently not possible given the limited capabilities of the NMR unit at the University of the Witwatersrand. However this is something that could be conducted in the future as a way to validate the results and the interpretations of this analysis.

3.3 Conclusions

The analysis of the CSD allowed for the analysis of many ligands and complexes that are structurally similar to **1** and **2**. This analysis found that **1** and **2** are structurally similar to other pincer ligands that have been crystallographically characterized. The ligands exhibited an *endo*|*endo* conformation, a trait shared by the majority of the ligands in this category.

DFT simulations were performed in order to predict structural features, conformational energy profiles and molecular orbital configurations. This was ultimately done so that the empirical data could be compared to experimentally derived dynamic ^{1}H NMR, FTIR and crystal structure data. This dissertation found that there is strong agreement between the computationally, and experimentally derived data for the ligand systems. In particular, the simulations clearly suggest that although the system is conformationally flexible (several low barriers to dihedral angle rotation), there is a strong thermodynamic preference of at least 30 kJ mol^{-1} for *endo*|*endo* over *endo*|*exo* or *exo*|*exo* conformations, the latter being especially unfavourable for the free ligands ($\Delta E > 100$ kJ mol^{-1}).

The presence of the one-dimensional H-bonded chain in solution and in the solid state for compound **2** was a key area that was explored in this dissertation. The presence of NH···O dimerization and higher oligomerization in the solid state was confirmed through crystal structure data, while dimerization (early-onset oligomerization) in the liquid state was confirmed through a ^{1}H NMR study as a function of [**2**]. The hydrogen bonding chains cause the C_2 symmetry of **2** to be overridden by the symmetry of the supramolecular one-dimensional chain. Similar one-dimensional hydrogen bonded chains/dimers have been reported in the literature.[90, 111] The result of this section in the dissertation contributes to what is known in regards to possible intermolecular interactions in pincer-type ligands, and will serve to assist scientists who are studying similar systems. The self-assembly was spontaneous, evidenced by the ΔG

value that was obtained. Oligomerization *via* H-bonding in **2** was not investigated by DFT methods. Despite this fact the crystal structures for **1** and **2** are in good agreement with the DFT calculated structures, suggesting that formation of one-dimensional chains as the supramolecular structure negligibly perturbs the preferred conformation of **2**.

The main structural differences between ligands **1** and **2** are due to the presence of aliphatic ring groups in **2** and aromatic rings in **1**. The aromatic rings in compound **1** cause an increase in resonance stabilization due to delocalization of electrons, which results in **1** having a higher degree of polarizability. The increased resonance stabilization of **1** has not appeared to have made an impact on the range of bond lengths in the structures (the bond lengths are all consistent with literature reference values). Molecular orbital simulations were used to predict the relative hardness of ligands **1** and **2** in order to determine which types of metals each ligand might, in theory, bind most effectively. Based on molecular orbital simulations (specifically HOMO-LUMO gap data), it was determined that ligand **2** is harder than ligand **1**, and will thus preferentially bind to harder metal cations. This information could be of vital importance for industry and researchers who seek to tweak and optimize pincer ligand systems so that selective binding to a given metal ion may be possible. It may be instructive going forward to measure the thermodynamic affinity of pincer ligands for metal ions of varying degrees of hardness.

The 3-D potential energy surfaces were used to predict what the most stable conformer at a given temperature might be, and also to determine which conformers are able to be accessed at different energy states. This conformational analysis is of vital importance because similar pincer ligands in the CSD have been observed as having *endo*|*endo, endo*|*exo and exo*|*exo* conformations. The dynamic ^{1}H NMR study showed that at 213.15 K only one N-H conformer of **1** was populated (global minimum with *endo*|*endo* N-H groups) and that at 243.15 K and higher temperatures *endo*|*endo, endo*|*exo and exo*|*exo* conformations are all populated. Finally, free rotation about the C-N amide bond in 2 had the largest barrier (84.0 kJ mol^{-1}) and required temperatures > 378.15 K.

3.4 References and Notes

13. M. P. Akerman, O. Q. Munro, M. Mongane, J. A. Staden, W. I. Rae, C. J. Bester, B. Marjanovic-Painter, Z. Szucs and J. R. Zeevaart, Journal of Labelled Compounds and Radiopharmaceuticals, 2013, 56, 530-535.

17. L. Messori, F. Abbate, G. Marcon, P. Orioli, M. Fontani, E. Mini, T. Mazzei, S. Carotti, T. O'Connell and P. Zanello, Journal of Medicinal Chemistry, 2000, 43, 3541-3548.

22. C. R. Wilson, A. M. Fagenson, W. Ruangpradit, M. T. Muller and O. Q. Munro, Inorganic chemistry, 2013, 52, 7889-7906.

24. F. Jensen, Introduction to computational chemistry, John Wiley & Sons, 2017.

31. P. Fuentealba, H. Preuss, H. Stoll and L. Von Szentpály, Chemical Physics Letters, 1982, 89, 418-422.

62. AIMAll (Version 17.11.14), Todd A. Keith, TK Gristmill Software, Overland Park KS, USA, 2017 (aim.tkgristmill.com)

63. E. D. Glendening, A. E. Reed, J. E. Carpenter, F. Weinhold. NBO Version 3.1

64. F. Czerny, P. Döhlert, M. Weidauer, E. Irran and S. Enthaler, Inorganica Chimica Acta, 2015, 425, 118-123.

65. J.-C. Wasilke, G. Wu, X. Bu, G. Kehr and G. Erker, Organometallics, 2005, 24, 4289-4297.

66. O. Baldovino-Pantaleón, S. Hernández-Ortega and D. Morales-Morales, Advanced Synthesis & Catalysis, 2006, 348, 236-242.

67. W. Ye, M. Zhao, W. Du, Q. Jiang, K. Wu, P. Wu and Z. Yu, Chemistry-A European Journal, 2011, 17, 4737-4741.

68. Q.-Q. Wang, R. A. Begum, V. W. Day and K. Bowman-James, Journal of the American Chemical Society, 2013, 135, 17193-17199.

69. K. Ghosh, S. Kumar, R. Kumar and U. P. Singh, Journal of Organometallic Chemistry, 2014, 750, 169-175.

70. P. J. Donoghue, J. Tehranchi, C. J. Cramer, R. Sarangi, E. I. Solomon and W. B. Tolman, Journal of the American Chemical Society, 2011, 133, 17602-17605.

71. D. Huang, O. V. Makhlynets, L. L. Tan, S. C. Lee, E. V. Rybak-Akimova and R. H. Holm, Inorganic Chemistry, 2011, 50, 10070-10081.

72. B. Bertrand and A. Casini, Dalton Transactions, 2014, 43, 4209-4219.

73. Y. Gartia, P. Ramidi, D. E. Jones, S. Pulla and A. Ghosh, Catalysis letters, 2014, 144, 507-515.

74. M. W. Johnson, A. G. DiPasquale, R. G. Bergman and F. D. Toste, Organometallics, 2014, 33, 4169-4172.

75. M. Ray, D. Ghosh, Z. Shirin and R. Mukherjee, Inorganic chemistry, 1997, 36, 3568-3572.

76. A. K. Singh, V. Balamurugan and R. Mukherjee, Inorganic chemistry, 2003, 42, 6497-6502.

77. L. Fan, B. M. Foxman and O. V. Ozerov, Organometallics, 2004, 23, 326-328.

78. J. Lapka, A. Paulenova, L. Zakharov, M. Y. Alyapyshev and V. Babain, IOP Conference Series: Materials Science and Engineering, 2010, 9, 012029.

79. D. Dhar, G. M. Yee, A. D. Spaeth, D. W. Boyce, H. Zhang, B. Dereli, C. J. Cramer and W. B. Tolman, Journal of the American Chemical Society, 2016, 138, 356-368.

80. T. Hirao, T. Moriuchi, T. Ishikawa, K. Nishimura, S. Mikami, Y. Ohshiro and I. Ikeda, Journal of Molecular Catalysis A: Chemical, 1996, 113, 117-130.

81. S. L. Barnholtz, J. D. Lydon, G. Huang, M. Venkatesh, C. L. Barnes, A. R. Ketring and S. S. Jurisson, Inorganic Chemistry, 2001, 40, 972-976.

82. R. V. Parish, B. P. Howe, J. P. Wright, J. Mack, R. G. Pritchard, R. G. Buckley, A. M. Elsome and S. P. Fricker, Inorganic chemistry, 1996, 35, 1659-1666.

83. Todd C. Harrop, Laurie A. Tyler, Marilyn M. Olmstead and Pradip K. Mascharak, European Journal of Inorganic Chemistry, 2003, 2003, 475-481.

84. C. Wallenhorst, K. V. Axenov, J. S. Samec, R. Fröhlich and G. Erker, Zeitschrift für Naturforschung B, 2007, 62, 783-790.

85. M.A. Fox, J.K. Whitesell, Organische Chemie: Grundlagen, Mechanismen, Bioorganische Anwendungen. Spektrum Akad. Verlag,1995.

86. M. F. Graham J. Tizzard, Philip A. Gale, Mark E, 2016, Cambridge Structural Database, DOI: 10.5517/ccdc.csd.cc1ljmnd

87. A. Galanti, O. Kotova, S. Blasco, C. J. Johnson, R. D. Peacock, S. Mills, J. J. Boland, M. Albrecht and T. Gunnlaugsson, Chemistry-a European journal, 2016, 22, 9709-9723.

88. W. Juan, H. Peng, H. Chao and Z. Bixue, Chinese Journal of Applied Chemistry, 2014, 32, 284-291.

89. S.-K. Ko, S. K. Kim, A. Share, V. M. Lynch, J. Park, W. Namkung, W. Van Rossom, N. Busschaert, P. A. Gale and J. L. Sessler, Nature chemistry, 2014, 6, 885.

90. N. W. Alcock, P. Moore, C. J. Reader and S. M. Roe, Journal of the Chemical Society, Dalton Transactions, 1988, 2959-2963.

91. B. Jia, Z.-Q. Hu, X.-T. Deng, C.-X. Cheng and S.-M. Shi, Acta Crystallographica Section E: Structure Reports Online, 2006, 62, o4902-o4903.

92. M. G. Fisher, P. A. Gale and M. E. Light, New Journal of Chemistry, 2007, 31, 1583-1584.

93. E. A. Katayev, G. D. Pantos, M. D. Reshetova, V. N. Khrustalev, V. M. Lynch, Y. A. Ustynyuk and J. L. Sessler, Angewandte Chemie International Edition, 2005, 44, 7386-7390.

94. J. M. Baumes, I. Murgu, R. D. Connell, W. J. Culligan, A. G. Oliver and B. D. Smith, Supramolecular Chemistry, 2012, 24, 14-22.

95. A. Casnati, N. Della Ca, M. Fontanella, F. Sansone, F. Ugozzoli, R. Ungaro, K. Liger and J. F. Dozol, European journal of organic chemistry, 2005, 2005, 2338-2348.

96. J. C. Burley, Acta Crystallographica Section B: Structural Science, 2005, 61, 710-716.

97. N. Adams, H. J. Arts, P. D. Bolton, D. Cowell, S. R. Dubberley, N. Friederichs, C. M. Grant, M. Kranenburg, A. J. Sealey and B. Wang, Organometallics, 2006, 25, 3888-3903.

98. J. Zhang, S. Liu, A. Li, H. Ye and Z. Li, New Journal of Chemistry, 2016, 40, 7027-7033.

99. M. a. P. Brandi-Blanco, D. Choquesillo-Lazarte, C. G. García-Collado, J. M. a. González-Pérez, A. Castiñeiras and J. Niclós-Gutiérrez, Inorganic Chemistry Communications, 2005, 8, 231-234.

100. M. J. Frisch, G. W. Trucks, H. B. Schlegel, G. E. Scuseria, M. A. Robb, J. R. Cheeseman, G. Scalmani, V. Barone, B. Mennucci, G. A. Petersson, H. Nakatsuji, M. Caricato, X. Li, H. P. Hratchian, A. F. Izmaylov, J. Bloino, G. Zheng, J. L. Sonnenberg, M. Hada, M. Ehara, K. Toyota, R. Fukuda, J. Hasegawa, M. Ishida, T. Nakajima, Y. Honda, O. Kitao, H. Nakai, T. Vreven, J. A. Montgomery, Jr., J. E. Peralta, F. Ogliaro, M. Bearpark, J. J. Heyd, E. Brothers, K. N. Kudin, V. N. Staroverov, R. Kobayashi, J.

Normand, K. Raghavachari, A. Rendell, J. C. Burant, S. S. Iyengar, J. Tomasi, M. Cossi, N. Rega, J. M. Millam, M. Klene, J. E. Knox, J. B. Cross, V. Bakken, C. Adamo, J. Jaramillo, R. Gomperts, R. E. Stratmann, O. Yazyev, A. J. Austin, R. Cammi, C. Pomelli, J. W. Ochterski, R. L. Martin, K. Morokuma, V. G. Zakrzewski, G. A. Voth, P. Salvador, J. J. Dannenberg, S. Dapprich, A. D. Daniels, Ö. Farkas, J. B. Foresman, J. V. Ortiz, J. Cioslowski, and D. J. Fox, Gaussian 09 (Gaussian, Inc., Wallingford CT, 2009).

101. O. Baldovino-Pantaleón, S. Hernández-Ortega and D. Morales-Morales, Advanced Synthesis & Catalysis, 2006, 348, 236-242.

102. O. Baldovino-Pantaleón, S. Hernández-Ortega and D. Morales-Morales, Inorganic Chemistry Communications, 2005, 8, 955-959.

103. C. Gunanathan and D. Milstein, Chemical reviews, 2014, 114, 12024-12087.

104. R. G. Pearson, Inorganic chemistry, 1988, 27, 734-740.

105. O. Q. Munro, S. D. Joubert and C. D. Grimmer, Chemistry-A European Journal, 2006, 12, 7987-7999.

106. P. R. Rablen, S. A. Pearlman and D. A. Miller, Journal of the American Chemical Society, 1999, 121, 227-237.

107. R. E. Carter and J. Sandstrom, The Journal of Physical Chemistry, 1972, 76, 642-647.

108. T. Drakenberg, K. I. Dahlqvist and S. Forsen, The Journal of Physical Chemistry, 1972, 76, 2178-2183.

109. C. R. Kemnitz and M. J. Loewen, Journal of the American Chemical Society, 2007, 129, 2521-2528.

110. Y. K. Kang and H. S. Park, Journal of Molecular Structure: THEOCHEM, 2004, 676, 171-176.

111. H. Zhang, J. Lee, A. D. Lammer, X. Chi, J. T. Brewster, V. M. Lynch, H. Li, Z. Zhang and J. L. Sessler, Journal of the American Chemical Society, 2016, 138, 4573-4579.

CHAPTER 4

Structural and Theoretical Studies on Pincer Chelates of d^8 Metal Ions

4.1 Introduction

4.1.1 Background and relevance of Au(III), Pd^{2+} and Pt^{2+} complexes

The invariant low-spin d^8 electron configuration of Pd^{2+}, Pt^{2+}, and Au(III) reflects the large ligand field splitting for these metal ions and ensures that their complexes are almost always square planar. However, inspection of the crystal structures of many simple Au(III) complexes in the Cambridge Crystallographic Database (CSD) reveals that it is common to find the Au(III) ion associated with both coordinating and non-coordinating anions or electron-rich, polar neutral groups. These charge-donating groups are normally located in axial positions above the plane of the Au(III) ion, often with a measureable lateral displacement from exact orthogonality. Figure 4.1 illustrates the fundamental geometry typical of Au(III)···Q interactions seen in the solid state.

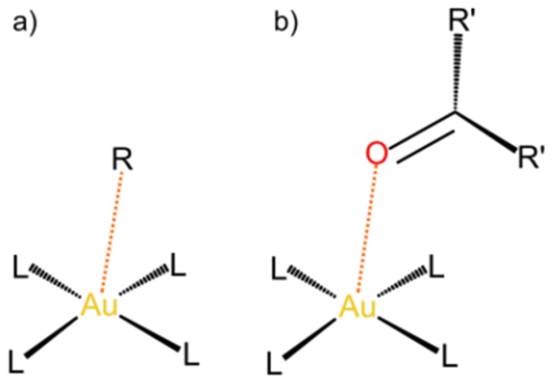


Figure 4.1. Diagram showing (a) a generalised example of the Au(III)···Q interaction, where Q axially interacts with Au(III), and (b) the stabilizing Au(III)···O=C interaction.

The importance of Au(III)···Q interactions in chemical biology is illustrated by the fact that cytotoxic macrocyclic Au(III) metallointercalators[11] which catalytically inhibit human topoisomerase I (Top 1), can only bind noncovalently to their DNA target if Au(III) is the

metal ion (the Ni^{2+} analogues failed to bind DNA and were not cytotoxic). A related study on cytotoxic square planar bis(pyrrole-imine) tris(chelates) of Au(III), which are DNA-binding metallointercalators that target topoisomerase II (Top 2), showed that the non-cytotoxic Pd^{2+} analogues failed to bind DNA[112]. In the case of the Au(III) macrocycles[11] the mechanism of action was pinned on the existence of a crucial, stabilizing Au(III)···O=C interaction involving the carbonyl group of thymine in the TA base pair targeted by the metallodrug for intercalative binding (Figure 4.1).

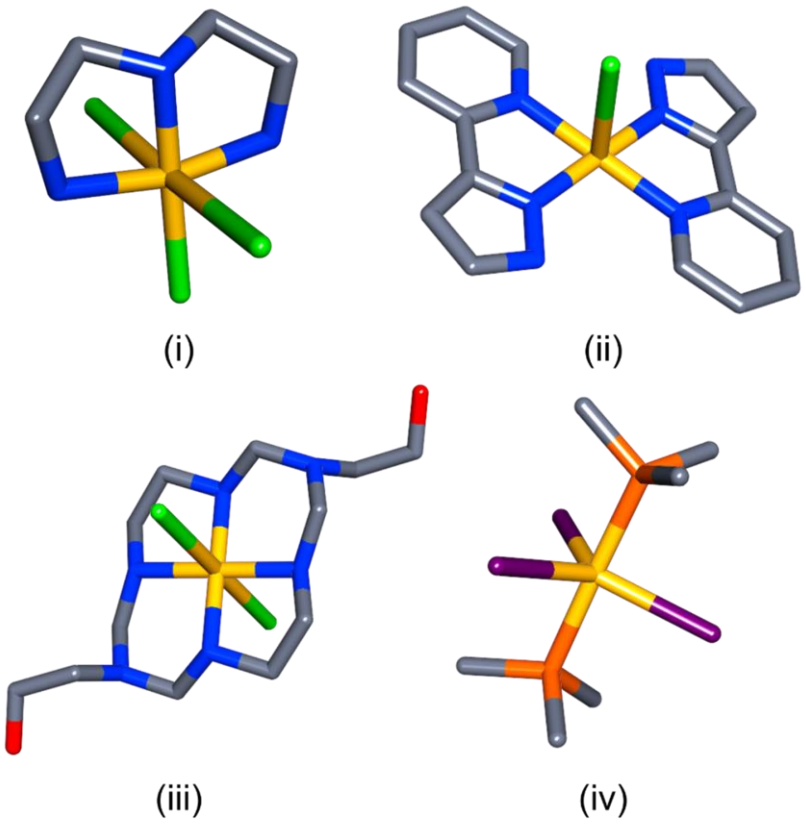


Figure 4.2. Diagram showing examples of structures obtained from the CSD, where the Au(III) ion is associated with non-coordinating, electron-rich groups. Hydrogen atoms have been omitted for visibility. Crystal structures of DODXID (i), NURYAB (ii), TEMMED (iii), and TUBBOH (iv) are shown.

Axial interactions involving Au(III) ions are prevalent in the CSD when examining structures of this nature, as illustrated in Figure 4.2 for DODXID[113], NURYAB[114], TEMMED[115] and TUBBOH.[116] Given the expectation that Au(III) complexes should typically be square planar and the ubiquity of axial interactions involving Au(III) in the solid state, a theoretical study aimed at delineating the nature of these axial interactions which lead to apparent higher coordination numbers for Au(III) is warranted.

4.1.2 Experimental design and aims for this chapter

If we assume that the metal cation (M) acts as a non-specific acceptor (i.e., one that lacks any geometric preference) for an ostensibly electronegative donor atom (Q), then a number of fundamental questions arise concerning M···Q interactions which may be of relevance to the design of novel metallointercalator compounds. First, what range of axial interactions are possible for Au(III)? Can they be categorized according to axial donor type? Second, how strong are these axial M···Q interactions? Are they typical ion···dipole interactions, or are they energetically more like hydrogen bonds? Third, the evidence to date suggests that Au(III) ions are better at forming stabilizing M···Q interactions than their isoelectronic Pt^{2+} and Pd^{2+} congeners, all other factors being equal. What is the fundamental reason for this phenomenon? Are the radially-expanded lowest-energy 6s or $6p_z$ atomic orbitals of Au(III) involved in any way?

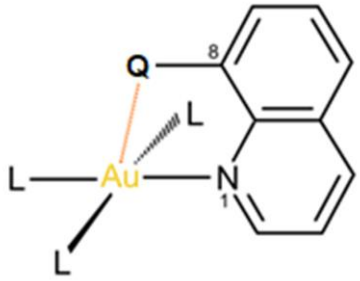


Figure 4.3. Diagram showing an example of the Au(III)···Q interaction that would occur in our proposed metal-quinoline system.

In this Chapter we have attempted to answer some of the aforementioned questions using a series of novel compounds designed to facilitate investigation of axial M···R interactions in Pd^{2+}, Pt^{2+}, and Au(III) compounds geometrically pre-organized to form these interactions. When conceptualizing the design of the compounds, we sought *a priori* to limit difficult-to-control crystal packing effects as far as possible through judicious choice of the ligands. Because quinolines bind well to d^8 metal ions through the pyridine N-donor atom, and those substituted at position 8 are commercially available, this group of ligands allows one to orient the substituent atom at position 8 on the ring above the square planar metal ion in an axially-offset manner in accord with the geometric requirement illustrated (Figure 4.1). We elected further to use sterically bulky tridentate bis(amide) pincer ligands to “capture” the structurally variable quinoline ligand in a somewhat restricted binding pocket to limit the degree of torsional freedom, the specific objective being to better-control formation of the offset M···Q

interaction involving the Q-substituent on the quinoline ring. These design specifications for the target compounds have been presented in Figure 4.3.

Our experimental and theoretical analysis of the conformational preferences of bis(amide)-pyridine pincer ligands (Chapter 3) clearly showed that this class of tridentate ligands is pre-organized for chelation of di- and trivalent metal ions via the neutral pyridyl nitrogen and two deprotonated amide nitrogen donors (NNN donor atom set, *endo*|*endo* conformer). Given the desired design framework illustrated in Figure 4.3, the tridentate pincer ligands of Chapter 3 are particularly well-suited to stabilizing Au(III) (as well as Pt^{2+} and Pd^{2+}) and ensuring square planar coordination of the d^8 metal ion when a quinoline co-ligand is bound in the "pocket" of the pincer ligand, thereby occupying the fourth coordination site at the metal centre.

4.1.3 Cambridge structural database (CSD) analysis

As discussed in Chapter 1, one of the goals of this project is to establish what range of axial M···Q interaction types are possible. This includes investigating the identity of Q atoms which interact most frequently and establishing common interaction distances.

The results of an analysis from the November 2016 CSD (5.3.8) have been presented below:

- Total number of AuN_4 type structures: 88
- Total number of AuN_4 type structures exhibiting axial Q interaction: 29
- Interacting Q atoms that were observed: H, O, F, Cl.

Average M···Q distance: 3.10 Å (distances below 3.5 Å were considered) where the Q atom is defined as an atom that is positioned above or below the plane of the square planar AuX_4. Note that in the case of multiple interacting atoms, only the atom closest to Au was considered. For the structure to be included in this analysis the Au···Q distance may be no greater than 3.5 Å. Only AuN_4-type structures were considered because a search of AuX_4 type structures yielded over 3600 hits. It is also useful to only consider AuN_4 type compounds because doing this controls for other structural factors and allows for comparisons between structures to be made in a more valid manner.

Table 4.1. Selected AuN_4-type structures that were found in the CSD. The identity of the axially interacting atom, and its distance from the Au(III) metal centre, have been included in the table.

CSD ref code	Interacting Q atom	Au···Q distance (Å)
BORROR[117]	O	2.761
BORQUW[117]	O	2.860
GEKRUL[118]	O	2.895
UCEXUX[119]	H	2.960
ROKFIG[120]	Cl	2.911
HAZMOM[121]	Cl	2.986
QAGBOS[122]	F	2.974

An additional analysis using a query of (Au/Pd/Pt-N_2Cl_3) was also performed. This was done because structures of this type are frequently listed as 5 or 6 coordinate in the CSD. This information will be used later on in the dissertation when we probe the M···Q interactions and make use of AIMAII to deduce the type of interaction.

The results of an analysis from the November 2016 CSD (5.3.8) have been presented below:

- Total number of (AuN_2Cl_3) type structures: 16
- Total number of (PdN_2Cl_3) type structures: 215
- Total number of (PtN_2Cl_3) type structures: 4

Table 4.2. Selected Au/Pd/Pt-N_2Cl_3-type structures that were found in the CSD. The identity of the metal, the axially interacting atom, the M···Q distance and the interaction type have been included in the table.

CSD ref code	Interacting Metal	Interacting Q atom	M···Q distance (Å)	Interaction type
AUBQNL01[55]	Au(III)	N	2.559	$(AuNCl_3)\cdots N$
CDMPAU[123]	Au(III)	N	2.584	$(AuNCl_3)\cdots N$
CPYQAU[124]	Au(III)	N	2.672	$(AuNCl_3)\cdots N$
DODXID[113]	Au(III)	Cl	3.183	$(AuN_2Cl_2)\cdots Cl$
ENESIB[125]	Pt(II)	Cl	2.318	$Cl\cdots(PtN_2Cl_2)\cdots Cl$
KASMIB[126]	Pt(II)	Cl	2.321	$Cl\cdots(PtN_2Cl_2)\cdots Cl$
BOKHAK[127]	Pd(II)	Cl	2.302	$Cl\cdots(PdN_2Cl_2)\cdots Cl$

In some cases, the N atom is above the plane of square planar $MNCl_3$, while in other cases the Cl atom is above the plane of square planar MN_2Cl_2. In some cases Q atoms interact above and below the plane, these structures particularly are common for Pd(II) and Pt(II) and have been included in Table 4.2 for sake of completeness. In the case of a 4-coordinate structure, with two axially interacting atoms, only the smaller of the two M···Q distances has been tabulated.

Interestingly, for all structures presented in Tables 4.1 and 4.2 (with the exception of UCEXUX) the M···Q distance is smaller than the sum of the van der Waals radii of the interacting atoms. The structural data suggest that these interactions are more than just weak electrostatic interactions, and could have some formal bond character. Further investigation is warranted to explain this phenomenon.

4.2 X-Ray Crystallography

In order to validate the computational studies and acquire experimental verification of metrical parameters for simple quinoline complexes of pincer ligands chelated to d^8 metal ions (Section 4.3), attempts to synthesize and structurally characterize a number of derivatives of this novel class of compounds were made. In general, most crystallization methods (including liquid and vapour diffusion experiments) failed to generate X-ray quality crystals of suitable target complexes, despite the fact that these compounds could be synthesized and detected via mass spectrometry in the reaction solution. The most effective method for growing single crystals of $[M(pincer)(Quinoline)]^{n+}$ derivatives proved to be slow evaporation of the reaction solution in acetonitrile (after transfer of the reaction solution to test tubes), which resulted in the isolation of acetonitrile solvates of the compounds of interest.

4.2.1 Crystal and molecular structure of $[Au(L1)(Quinoline)][PF_6]\cdot(CH_3CN)$

The X-ray structure of $[Au(L1)(Quinoline)][PF_6]\cdot(CH_3CN)$ is depicted in Figure 4.4. The Au(III)

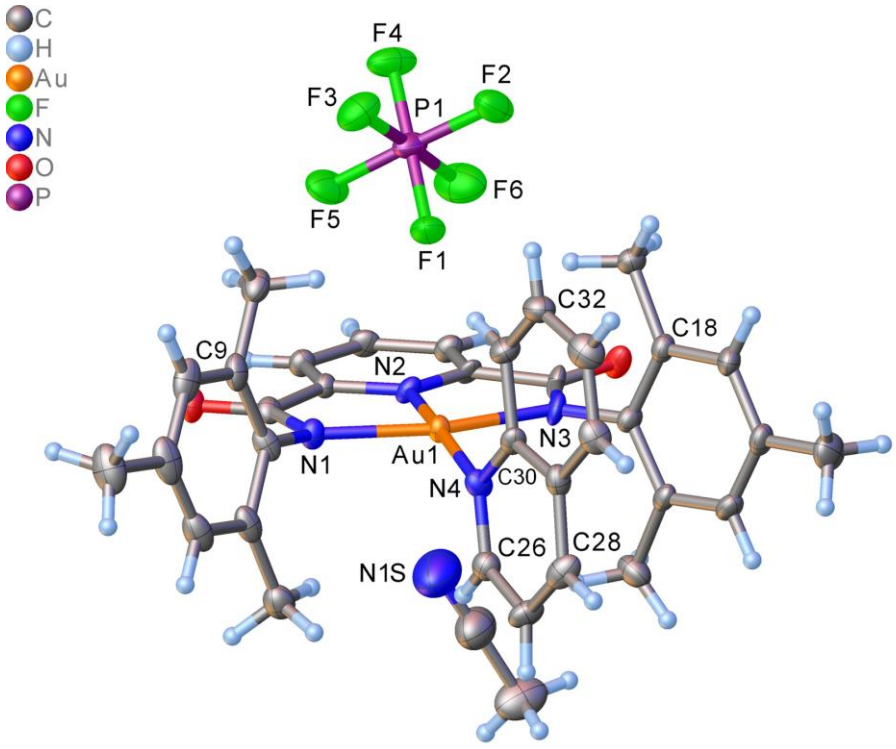


Figure 4.4. Thermal ellipsoid plot (30% probability surfaces) of the $[Au(L1)(Quinoline)][PF_6]\cdot(CH_3CN)$ crystal structure showing selected atom labels from the crystallographic numbering scheme. Hydrogen atoms have been rendered as spheres of arbitrary radius.

cation is nominally square planar with the three N-donors of the pincer ligand taking up three of the four donor atom sites about the metal ion. The pyridine and amide nitrogen atoms lie

in the same plane and the pincer ligand adopts the thermodynamically favoured *endo*|*endo* conformation (as established by an analysis of the metal-free ligand system in Chapter 3). The fourth coordination site at the Au(III) centre is located within the "arms" of the pincer ligand and is occupied by the N-donor atom of the quinoline co-ligand. Selected bond distances and bond angles for the coordination group are summarised in Table 4.3. The Au–$N_{pyridine}$ bond (1.95 ± 0.01 Å) is shorter than the flanking Au–N_{amide} bonds (mean, 2.03 ± 0.01 Å), which are equivalent (within one standard deviation) to the Au–$N_{quinoline}$ bond (2.04 ± 0.01 Å).

The plane of the quinoline ligand (10 atoms) in [Au(L1)(Quinoline)][PF_6]·(CH_3CN) exhibits a dihedral angle of 84.7° relative to the plane of the pyridine ring and amide chelate atoms (11 atoms in total within the pincer ligand, Figure 4.5). The torsion angle best-measuring the non-orthogonal orientation of the quinoline ligand, N3—Au1—N4—C30, measures 73(1)°, consistent with a considerable off-axis tilt of the guest ligand, which is evidently caused by π–π interactions involving the closest mesityl ring and the quinoline ligand (centroid···centroid distance, 3.650 (8) Å; ring···ring angle, 16.3(5)°). This rather significant intramolecular π–π

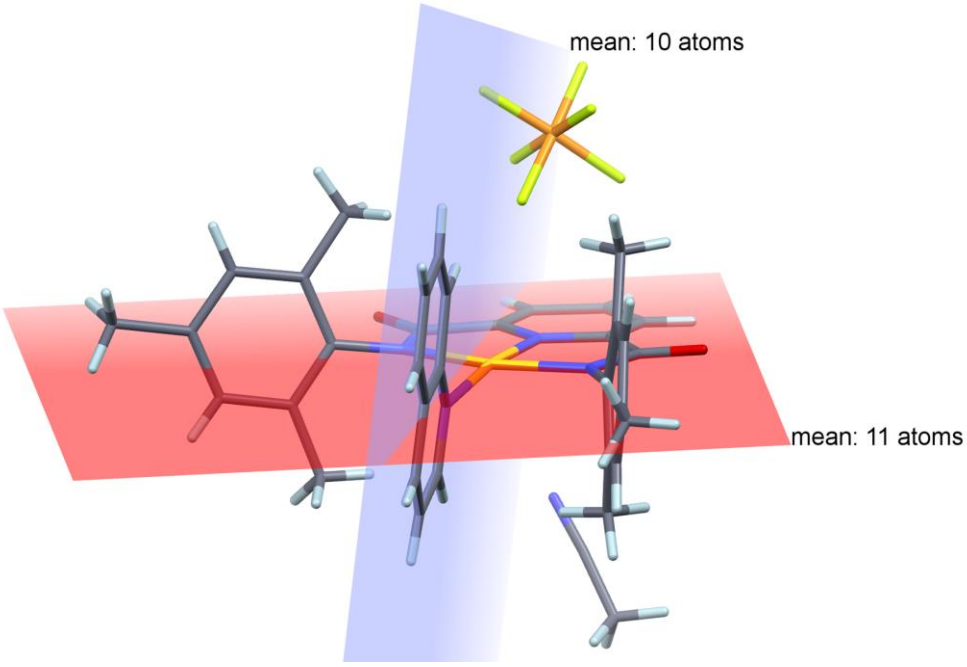


Figure 4.5. Diagram illustrating the least-squares planes between the metal-chelating 11-atom pincer ligand and the 10-atom quinoline ligand plane. The dihedral angle between the planes is 84.7°. The Au(III) ion and three N atoms of the pincer ligand lie approximately in the chelate plane (Au is displaced only 0.04 Å below the plane), while the quinoline N atom is displaced significantly below the plane (0.36 Å) giving it the appearance of a downward tilt.

interaction accounts for the fact that the plane of the quinoline ligand does not lie within the N2–Au1–N4 plane, which might be expected in the absence of such an interaction (for

example, in the cyclohexyl ligand analogue). As shown by the crystal packing diagram in Figure 4.6, the quinoline ligand of one molecule is also π-stacked with the mesityl ring of the closest neighbour in the lattice. The intermolecular π-π interaction has a centroid···centroid distance of 3.75 (8) Å, a lateral displacement of 1.82 (2) Å, and a ring···ring angle of 13.2°. As discussed later, these nonbonded intermolecular interactions impact significantly on the conformation of the molecule and account for the fact that the DFT-calculated *in vacuo* structure shows significant conformational deviations from the crystal structure.

Regarding the supramolecular or extended crystal structure of the compound, the hexafluorophosphate(V) counterion and acetonitrile solvent molecule are located above and below the the Au(III) ion. The relevant nonbonded distances are: F1···Au1, 3.18(1) Å; F1···N2, 3.02(1)Å; N1S···Au1, 3.46(4) Å; and N1S···N2, 3.06(3) Å. The F1···Au1 contact is only fractionally longer than the sum of the van der Waals radii of the interacting atoms (3.13 Å).

Table 4.3. Selected geometrical and conformational parameters for the structure of [Au(L1)(Quinoline)][PF_6]·(CH_3CN).

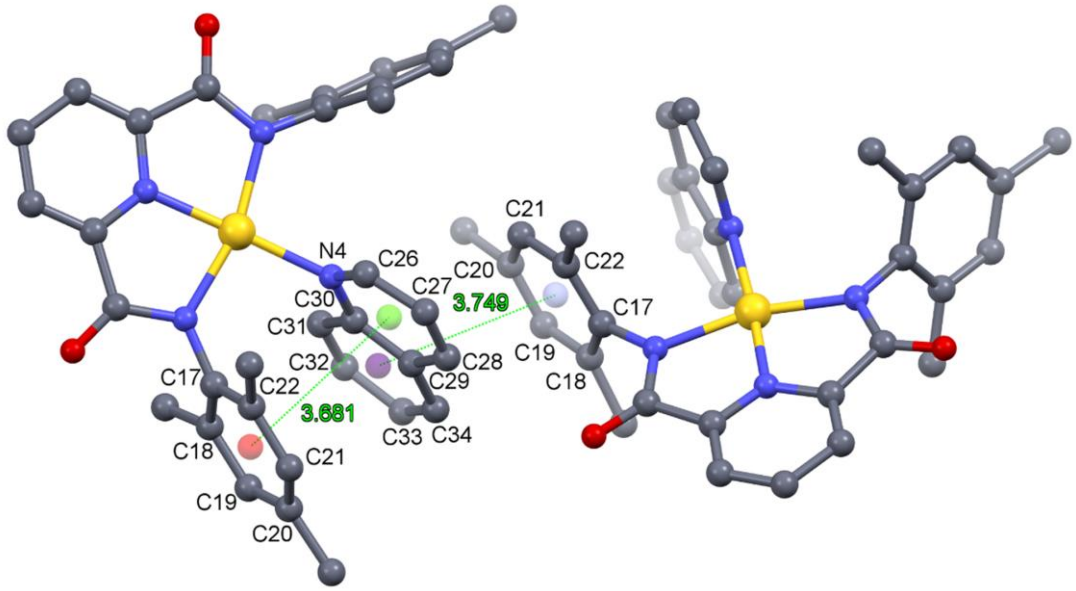


Figure 4.6. Partly labelled diagram illustrating the packing between two $[Au(L1)(Quinoline)]^+$ cations. The quinoline ligand of the left structure [symmetry code: *x*, *y*, *z*] is π-stacked with the mesityl ring of the neighbouring molecule [symmetry code: –0.5+*x*, 0.5–*y*, *z*] in the lattice. Ring centroids are illustrated as coloured spheres; distances between selected centroids are in Å. H atoms have been omitted for clarity.

Bond length/bond angle	Length/degree (Å/°)	Bond angle/dihedral angle	(°)
Au1—N4	2.035 (10)	N3—Au1—N4	94.8 (4)
Au1—N2	1.948 (10)	N3—Au1—N1	164.1 (5)
Au1—N3	2.027 (10)	N1—Au1—N4	101.1 (4)
Au1—N1	2.035 (11)	Au1—N1—C8—C9	96 (1)
N2—Au1—N4	172.0 (5)	N1—Au1—N4—C30	–107 (1)
N2—Au1—N3	81.8 (4)	N3—Au1—N4—C30	73 (1)
N2—Au1—N1	82.4 (4)	Au1—N3—C17—C18	–93 (1)

The X-ray data for [Au(L1)(Quinoline)][PF_6]·(CH_3CN) listed in Table 4.3, particularly the coordination bond distances between the metal ion and pincer ligand donor atoms compare favourably with those reported by Johnson *et al.*[12] (CSD code SOPCEH) for Au(L1)Cl (Au—$N_{pyridine}$, 1.952 Å; Au—N_{amide}, 2.029 ± 0.001 Å). This observation is expected due to the fact that the pincer ligand effectively dominates the coordination geometry of the Au(III) ion and the fourth ligand is free to adopt a less restricted coordination position at the metal centre. There are no pyridine or quinoline adducts of Au(III) pincer ligands in the literature to gauge the accuracy of the Au—$N_{quinoline}$ bond distance determined in this dissertation. However, the structure of [$Au(Py)_4$][BF_4]$_3$·(CH_3CN) reported by Corbo *et al.*[128] exhibits a mean Au—$N_{pyridine}$ bond length of 2.026 ± 0.006 Å, which is consistent (within experimental error) with the Au—$N_{quinoline}$ bond distance (Au1—N4, Table 4.3) determined above.

4.2.2 Crystal and molecular structure of Pd(L1)(Quinoline)·(CH_3CN)$_n$

The X-ray structure of Pd(L1)(Quinoline) is shown in Figure 4.7; selected bond distances, bond angles, and dihedral angles are given in Table 4.4. The quality of the crystal of Pd(L1)(Quinoline) used for data collection was not overly high (internal *R*-factor = 6.15%), but was the best of several crystals screened. The crystal was preserved in Paratone® oil during data collection to limit solvent loss at ambient temperature. During structure solution and refinement, it was not possible to assign electron density residing in an extensively disordered solvent region to discrete acetonitrile molecules. The disordered solvent was thus masked (using the default settings in OLEX2) for the final refinement cycles. Thus, although the experimental structure is that of a solvate of acetonitrile, specific solvent molecules are not shown due to the fact that they could not be experimentally located. The true number of solvent molecules in the asymmetric unit is thus also unknown for this structure. The total

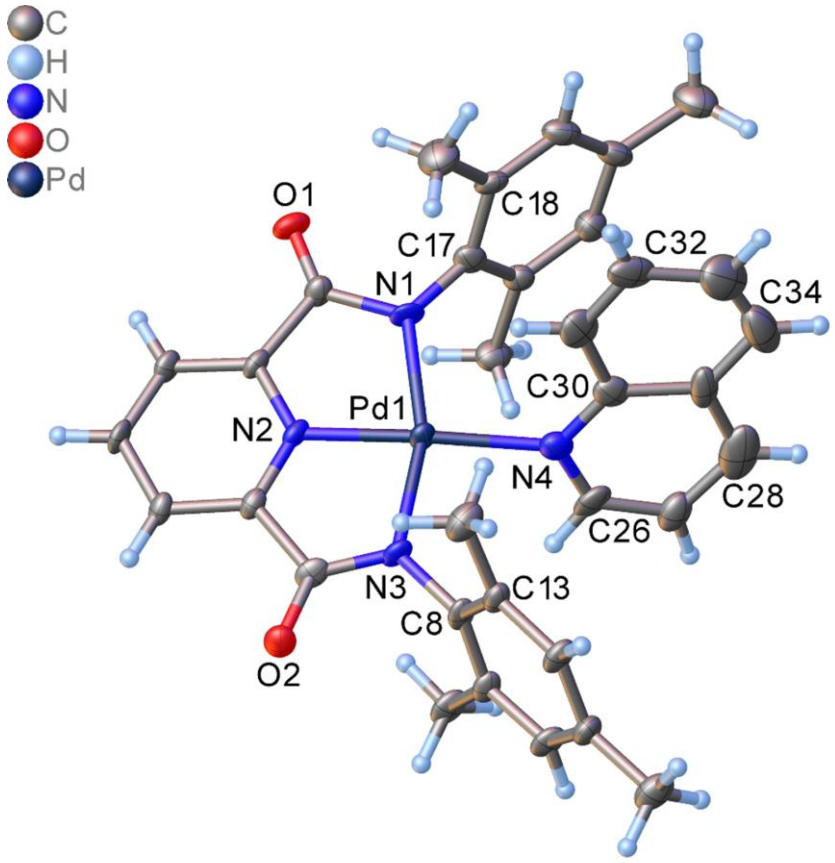


Figure 4.7. Thermal ellipsoid plot (25% probability surfaces, 296 K) of the Pd(L1)(Quinoline) crystal structure showing selected atom labels from the crystallographic numbering scheme. Hydrogen atoms have been rendered as spheres of arbitrary radius. Solvent (acetonitrile) is associated with the structure, but due to disorder and diffuse electron density was omitted using solvent masking in OLEX2. Two voids (each corresponding to 967.6 Å^3; 368.6 electrons) exist in the asymmetric unit at (0.000, 0.000, –0.986) and (0.500, 0.500, –0.402).

solvent accessible volume in the unit cell measured 1935.3 Å^3, amounting to 27.1% of the total unit cell volume.

Despite the above limitations in the X-ray data, which resulted in a final R_1 > 10%, the X-ray structure of Pd(L1)(Quinoline) is informative, of sufficient precision, and of scientific value to the study presented in this dissertation (especially as a form of structural verification of the DFT calculations presented later). As observed for the Au(III) analogue (discussed above), the quinoline ligand occupies the expected fourth coordination site at the metal centre and resides in the “pocket” created by the mesityl rings (or “arms”) of the pincer chelate. The 10-atom plane of the quinoline ligand makes a dihedral angle of 68.5° relative to the 11-atom plane of the Au, pyridine, and two chelating amide groups. The plane of the visibly tilted quinoline ligand does not bisect the plane of the N2—Pd1—N4 vector, being distinctly offset in the same manner as observed above for the Au(III) analogue. This structural feature, as in the case of the Au(III) complex, suggests the presence of significant intramolecular π-π stacking between the quinoline rings and the nearest mesityl ring flanking the ligand binding

pocket (i.e., that containing C17). The relationship between the relevant dihedral planes discussed above is depicted more graphically in Figure 4.8. An intramolecular π-π interaction exists between the mesityl ring containing C18 and the coordinated quinoline ring containing the pyridine-type N atom (N4). The angle between the ring planes measures 26.5°, the centroid-centroid distance is 3.87 Å, and the lateral shift distance (for the centroids) is 0.68 Å.

Table 4.4. Selected metrical parameters for the X-ray structure of Pd(L1)(Quinoline).

Bond length/bond angle	Length/degree (Å/°)	Bond angle/dihedral angle	(°)
Pd1—N2	1.932 (7)	N1—Pd1—N4	98.6 (4)
Pd1—N1	2.045 (7)	N3—Pd1—N1	162.2 (3)
Pd1—N4	2.048 (10)	N3—Pd1—N4	99.1 (3)
Pd1—N3	2.041 (7)	N1—Pd1—N4—C30	61(1)
N2—Pd1—N1	81.7 (3)	Pd1—N1—C17—C18	106(1)
N2—Pd1—N4	174.2 (4)	Pd1—N3—C8—C13	82(1)
N2—Pd1—N3	80.7 (3)		

As observed with the Au(III) analogue, the coordination group distances for Pd(L1)(Quinoline) match the pattern expected for coordination of the metal ion by the pincer ligand. Specifically, the Pd—$N_{pyridine}$ bond measures 1.932 (7) Å and is the shortest of the three bonds, while the pair of chemically equivalent Pd—N_{amide} bonds average 2.043 (2) Å and are thus comparable (within one standard deviation) to the Pd—$N_{quinoline}$ bond (Pd1—N4, 2.048 ± 0.010 Å). Interestingly, these bond lengths in the Pd(II) derivative are only 0.5% longer than those observed for the Au(III) derivative, despite the higher oxidation state of the metal ion in the gold chelate and its markedly smaller van der Waals radius (as discussed later). This presumably indicates substantial control of the metal ion coordination geometry by the ridged, pre-organized pincer ligand.

As far as comparing the X-ray data for Pd(L1)(Quinoline) with data available in the literature is concerned, the most relevant structure is that of (acetonitrile)-(*N*,*N*'-bis(4-methylphenyl)pyridine-2,6-dicarboxamidato)palladium(II) acetonitrile solvate (DOGKER[68]). In this Pd(II) derivative, the Pd—$N_{pyridine}$ bond measures 1.923 Å, while the Pd—N_{amide} bond distances average 2.034 ± 0.011 Å; both are thus in agreement with the structural data for

Pd(L1)(Quinoline) given in Table 4.4. There are no pyridine or quinoline addicts of Pd(II) pincers available in the literature for comparison of the Pd—$N_{quinoline}$ bond distance.

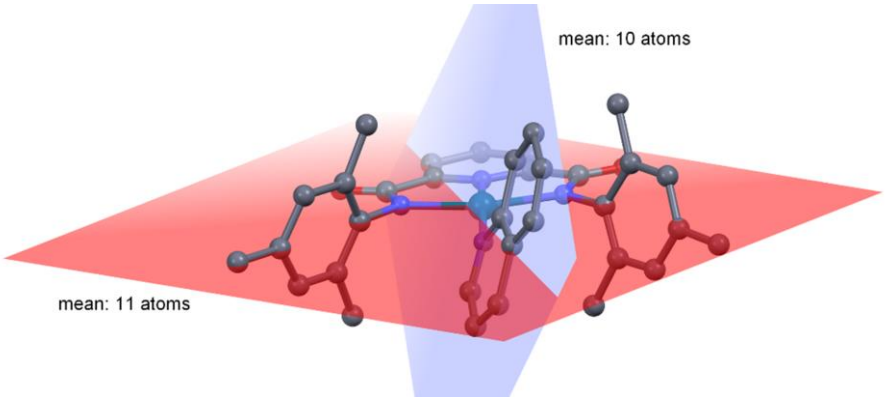


Figure 4.8. Diagram illustrating the least-squares planes between the metal-chelating 11-atom pincer ligand and the 10-atom quinoline ligand plane for Pd(L1)(Quinoline). The dihedral angle between the planes is 68.5°. The Pd(II) ion and three N atoms of the pincer ligand lie approximately in the chelate plane (Pd is displaced only 0.08 Å below the plane), while the quinoline N atom is displaced significantly below the plane (0.41 Å) giving it the appearance of a downward tilt. H atoms have been omitted for clarity.

4.3 Computational Chemistry

4.3.1 General comments and procedures

The initial input structures used for the simulations were created by modifying the crystal structure of *N,N'*-bis(2,4,6-trimethylphenyl)-2,6-pyridinecarboxamidato(quinoline)Au(III) as appropriate, using GaussView 5.0,[129] and saved as .mol2 files. These files were used as the inputs for density functional theory (DFT) calculations using GAUSSIAN 09W (WIN64).[130] Initial simulations were performed (in vacuo) at the HSEH1PBE/SDD[31] level of theory, final simulations were performed (*in vacuo*) at the HSEH1PBE/SARC-ZORA[131]/(6-311G(d,p)[132] or DGDZVP[35]) level of theory. The SDD basis set was chosen because of its accuracy and speed for heavier elements, making it ideal for use in calculations of complexes containing heavy metal ions.

The SARC-ZORA[131] (segmented all-electron relativistically contracted (SARC) zeroth-order regular approximation (ZORA)) all-electron scalar relativistic basis sets were used for each of the metals in question (Au, Pd, Pt). These are cutting-edge basis sets, that computational chemists have not had access to in the past, and they have proved to be the perfect tool for obtaining data with a high level of accuracy which is absolutely vital for the process of probing the nature of the electrostatic interactions that we are interested in. The outputs of these simulations, in conjunction with atoms in molecules (AIM) analysis (particularly analysis of the Laplacian of the electron density of electrostatic interactions and bonds), provide an unambiguous way to differentiate between formal dative covalent bonds and interactions that are electrostatic. The results of these analyses can also provide us with a measure of the electron density of the bond critical point of the interaction and can thus provide us with a measure of the strength of the interaction without having to consider thermodynamic factors directly. This is possible because the electron density at a bond critical point is correlated to the strength of the bond.[42] AIM analysis was performed using AIMAII.[133]

All of the simulations reported in this section have been calculated using the SARC-ZORA basis set for the metal and the 6-311G(d,p)[132] basis set was used for the remaining light elements. However the SARC-ZORA/DGDZVP[35] basis set was used for Iodine-containing structures, because iodine is not supported by the 6-311G(d,p) basis set. In all cases, the nature of the stationary states located on the potential energy surface were validated using frequency calculations and were determined to be true minima where no negative frequency eigenvalues were observed. Population analysis of the final wave function, for each

geometry-optimized structure, was performed using natural bond orbital analysis (NBO) using NBO 3.0[134] (running in Gaussian 09W).

4.3.2 Objectives and purpose of analysis

In this study, the main purpose of investigating correlations and relationships between structural and electronic features of the compound's structure is ultimately to determine which factors influence the strength of the M···Q interaction. Because of this, it is important for us to differentiate between correlations that occur because a structural element has changed as a result of a change in M···Q interaction strength and correlations that occur as the result of a variation in a structural element that causes a change in the M···Q interaction strength (a causal relationship where the factor in question is directly responsible changes for the M···Q interaction strength). We want to isolate which particular variables have the greatest impact on the strength of the M···Q interaction.

In keeping with the design criteria illustrated in Figure 4.3, we chose to use the conformationally-pre-organized pincer ligands H_2L1 and H_2L2 (Chapter 3) as chelators for the d^8 metal ions Au(III), Pt(II), and Pd(II). The complexes used for computational analysis with quinolines bearing a single atom substituent at position 8 in the ring are listed in Table 4.5. The naming convention employed for the compounds studied as well as an illustration of their structures is given in Figure 4.9.

The approach taken in this dissertation to simplify the presentation and discussion of what amounts to a large body of computational data (both DFT and AIMAII) is first to show that the DFT-calculation methodology employed is robust and accurate enough to match experimentally-derived data (X-ray crystal structures). Because the X-ray structure analyses suggested that quinoline co-ligands bound to the metal centres of pincer-chelated ions can have orientations that are non-orthogonal relative to the plane of the pincer chelate, the second step in the approach was to use DFT methods to carry out conformational analyses of quinoline rotamers for this class of compounds, with a specific focus on the Au(III) chelates. The final step was to then carry out the required calculations needed to probe the strength of the M···Q interaction in the target compounds with the validated DFT methodology.

Table 4.5. A list of the structures on which DFT and AIM analysis was performed. See Figure 4.9 for details on the naming convention used for the compounds.

Au(III) Complexes	Pd(II) Complexes	Pt(II) Complexes
	Complexes of [L1]$^{2-}$	
[Au(L1)(8-F-Quin)]$^{+}$	[Pd(L1)(8-F-Quin)]	[Pt(L1)(8-F-Quin)]
[Au(L1)(8-Cl-Quin)]$^{+}$	[Pd(L1)(8-Cl-Quin)]	[Pt(L1)(8-Cl-Quin)]
[Au(L1)(8-Br-Quin)]$^{+}$	[Pd(L1)(8-Br-Quin)]	[Pt(L1)(8-Br-Quin)]
[Au(L1)(8-I-Quin)]$^{+}$	[Pd(L1)(8-I-Quin)]	[Pt(L1)(8-I-Quin)]
[Au(L1)(8-H-Quin)]$^{+}$	[Pd(L1)(8-H-Quin)]	[Pt(L1)(8-H-Quin)]
[Au(L1)(8-OMe-Quin)]$^{+}$	[Pd(L1)(8-OMe-Quin)]	[Pt(L1)(8-OMe-Quin)]
[Au(L1)(8-SeH-Quin)]$^{+}$	[Pd(L1)(8-SeH-Quin)]	[Pt(L1)(8-SeH-Quin)]
[Au(L1)(8-SH-Quin)]$^{+}$	[Pd(L1)(8-SH-Quin)]	[Pt(L1)(8-SH-Quin)]
[Au(L1)(8-NH_2-Quin)]$^{+}$	[Pd(L1)(8-NH_2-Quin)]	[Pt(L1)(8-NH_2-Quin)]
[Au(L1)(8-OH-Quin)]$^{+}$	[Pd(L1)(8-OH-Quin)]	[Pt(L1)(8-OH-Quin)]
	Complexes of [L2]$^{2-}$	
[Au(L2)(8-F-Quin)]$^{+}$	[Pd(L2)(8-F-Quin)]	[Pt(L2)(8-F-Quin)]
[Au(L2)(8-Cl-Quin)]$^{+}$	[Pd(L2)(8-Cl-Quin)]	[Pt(L2)(8-Cl-Quin)]
[Au(L2)(8-Br-Quin)]$^{+}$	[Pd(L2)(8-Br-Quin)]	[Pt(L2)(8-Br-Quin)]
[Au(L2)(8-I-Quin)]$^{+}$	[Pd(L2)(8-I-Quin)]	[Pt(L2)(8-I-Quin)]
[Au(L2)(8-H-Quin)]$^{+}$	[Pd(L2)(8-H-Quin)]	[Pt(L2)(8-H-Quin)]

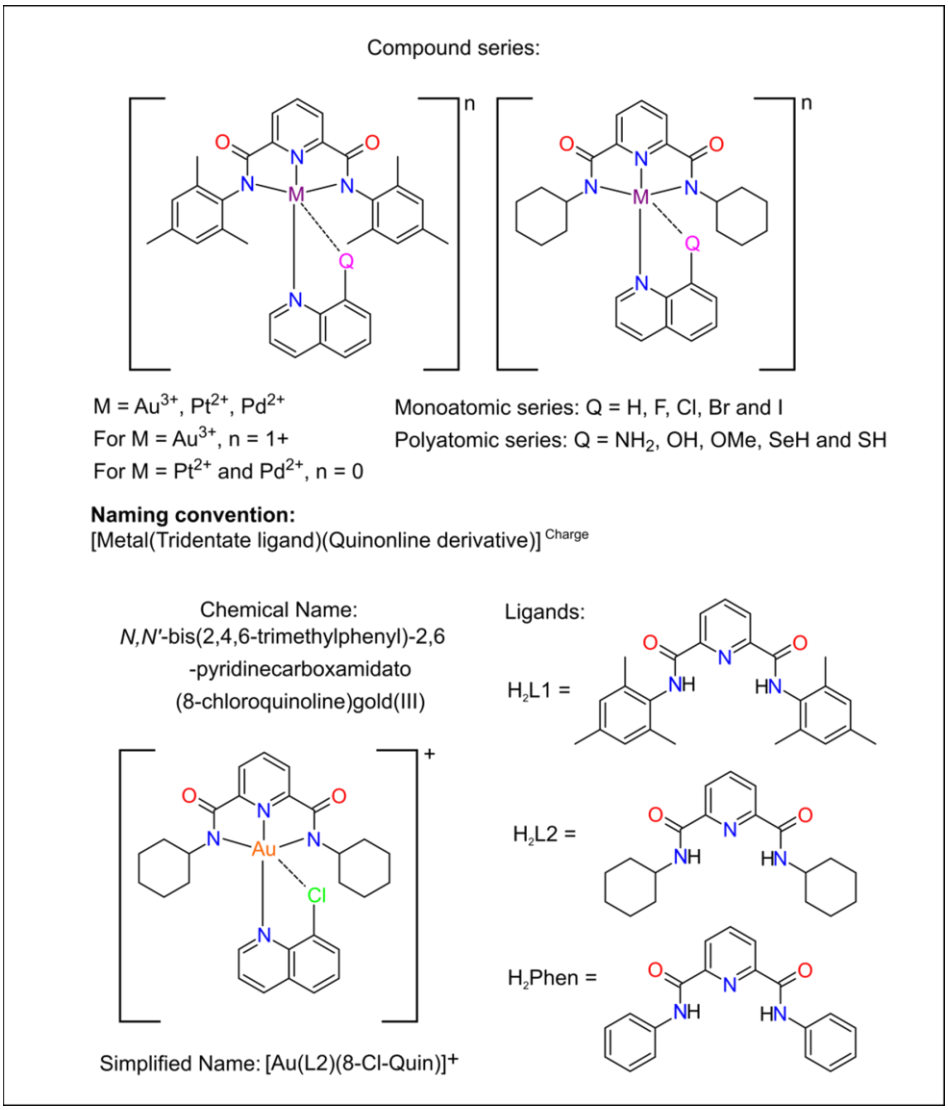
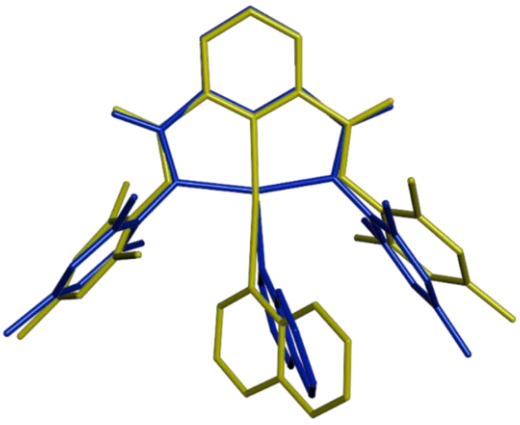


Figure 4.9. Diagram summarising the structures that were investigated, and the simplified naming convention that will be used throughout this dissertation.

The polyatomic substituent series (Q = NH_2, OH, OMe, SeH, and SH; Figure 4.9) did not adhere to the linear trends that were observed for the monoatomic substituent series (Table. 4.3) and so the structural properties of the polyatomic-substituted compounds seem to be unpredictable or only weakly predictable by the criteria we have analysed them with. Consequently, the data that are presented in this Chapter are specific to the results for the monoatomic series. The monoatomic series proved to be the easiest for which to establish and investigate trends. This is likely due to all atoms in the series having similar relative valence shell electron configurations. As a result there are fewer variables and so the various structural and electronic trends in the structures are more easily discernible. The variability of the polyatomic series seems to be too great and so structural and electronic trends for the structures are not able to be predicted.

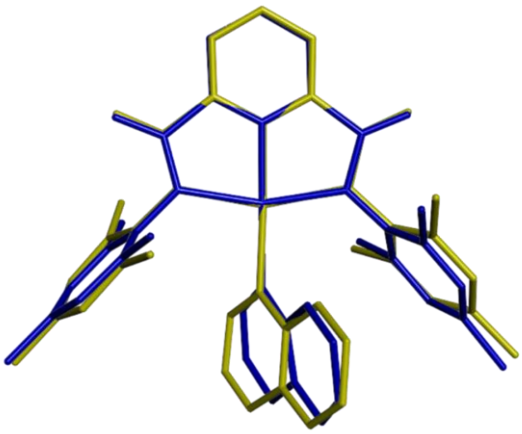
4.3.3 Comparison between the crystal and DFT-calculated structures

Computational methods of general utility should be able to reproduce experimentally-derived structural data accurately. This includes being able to predict bond lengths and angles as well as the conformational architecture of the compounds of interests. Comparison of DFT-calculated structures with suitable X-ray structures (where these are available) is a necessary validation of a theoretical approach or method being used to compute the properties of a series of related compounds. Because we were able to crystallize two metal



SI: 85.96 %

Figure 4.10a. A comparison between the DFT-calculated (yellow) and X-ray crystal structure (blue) of $[Au(L1)(8\text{-H-Quin})]^+$. The DFT calculation was performed at the HSEH1PBE/SARC-ZORA/ 6-311G(d,p) level of theory. For the DFT calculation the SARC-ZORA basis set was used for the metal (Au) and the 6-311G(d,p) basis set was used for light atoms (H, C, N, O). SI: 85.96%. Hydrogen atoms have been excluded for visibility.



SI: 97.50 %

Figure 4.10b. A comparison between the DFT-calculated (yellow) and X-ray crystal structure (blue) of Pd(L1)(8-H-Quin). The DFT calculation was performed at the HSEH1PBE/SARC-ZORA/ 6-311G(d,p) level of theory. For the DFT calculation the SARC-ZORA basis set was used for the metal (Pd) and the 6-311G(d,p) basis set was used for light atoms (H, C, N, O). SI: 97.50%. Hydrogen atoms have been excluded for visibility.

complexes relevant to the theoretical study in this Chapter, two structural comparisons are possible, as illustrated below.

The crystal structure of $[Au(L1)(8\text{-H-Quin})]^+$ is in fairly good agreement with the DFT-calculated structure, as evidenced by the similarity index (SI) for the two structurally-superimposed molecules (85.96%, Figure 4.10a). A possible reason for the difference observed between the two structures is the presence of a $[PF_6]^-$ ion and an acetonitrile solvent molecule in the lattice of the crystal structure. Furthermore, the DFT calculations were performed *in vacuo* and thus crystal packing effects were not taken into account for the DFT-calculated structure. The π-stacking which leads to a tilted coordination mode for the quinoline ligand is partially accounted for by the *in vacuo* DFT simulation. The packing interaction diagram for the X-ray structure (Figure 4.6) reveals that intermolecular quinoline···mesityl π-π interactions exist. These are not included in the *in vacuo* simulations because such simulations on molecular aggregates are computationally very expensive and require inclusion of dispersion effects. This aside, the advantage of comparing an *in vacuo* calculated structure with an experimental crystal structure is that it highlights when an experimental structure is subject to appreciable nonbonded packing interactions (as in the present case).

The crystal structure of Pd(L1)(8-H-Quin) is in good agreement with the corresponding DFT-calculated structure, having a near-perfect similarity index (SI) value when superimposed (97.50%) (Fig. 4.10b). The minor differences that are observed between the two structures are, as in the above case of $[Au(L1)(8\text{-H-Quin})]^+$, likely caused by packing effects that are not taken into account during the *in vacuo* DFT-simulation. These differences involve minor differences in the orientations of the mesityl substituent rings as well as the quinoline rings. The π-stacking interaction which leads to a tilted coordination mode for the quinoline ligand was also seen in DFT-calculated structure. This result is particularly encouraging because it strongly indicates that the DFT-calculated structures of the compounds listed in Table 4.5 are sufficiently accurate and can be reliably used to delineate trends in the electronic and molecular structures of the series of compounds.

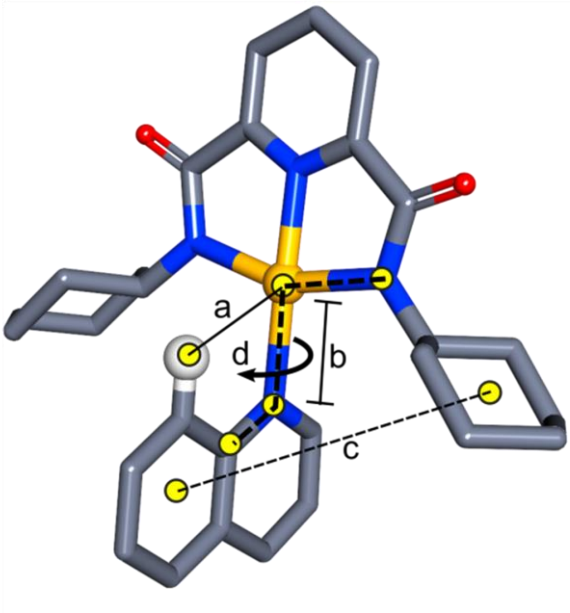


Figure 4.11. Diagram defining the main structural features that were systematically analysed for a series of Au(III) pincer complexes. The structure of $[Au(L2)(Quin)]^+$ has been used for illustration: (a) M···Q distance, *l*; (b) M—$N_{(Quin)}$ distance; (c) Inter-centroid distance; (d) Torsion angle defining the orientation of the quinoline ligand, *d.* The electron density at the bond critical point along *a*, ρ(M···Q), was obtained from AIMAII analysis of the final DFT-calculated geometry and electron density of the system; the location of the bond critical point (BCP) was structure-dependent.

4.3.4 DFT-calculated energy profiles: Au(III) conformers (quinoline rotamers)

Because the X-ray structures of $[Au(L1)(8\text{-H-Quin})]^+$ and Pd(L1)(8-H-Quin) showed that the quinoline co-ligand could tilt substantially away from an orthogonal orientation relative to the plane of the pincer ligand and chelated metal ion, we elected to study the rotamer (conformer) energy profiles of several metal complexes in the series. Importantly, we wanted to understand what energy barriers exist for rotation of the quinoline co-ligand as well as what the lowest-energy orientation of the quinoline co-ligand should be in the absence of crystal packing effects and as a function of three pincer ligand types: (i) L1 with mesityl (i.e., bulky aromatic) substituents, (ii) L2 with cyclohexyl substituents (i.e., bulky aliphatic substituents), and (iii) the parent pincer ligand with unsubstituted aryl ring substituents (i.e., simple phenyl rings). The results of this analysis are presented in Figure 4.11.

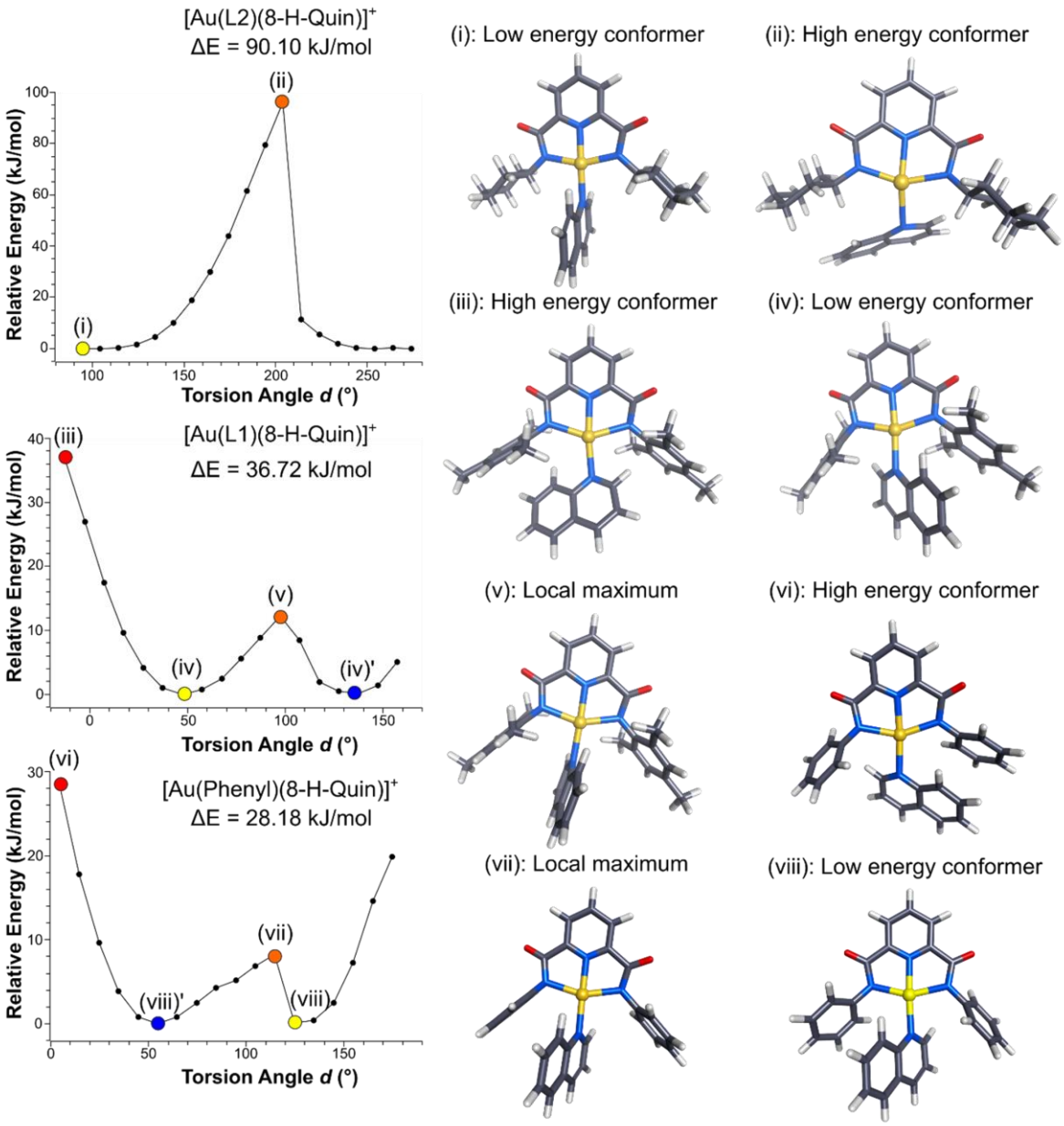


Figure 4.12. Diagram showing the energy profile of quinoline rotamers for [Au(L1)(8-H-Quin)]$^+$, [Au(L2)(8-H-Quin)]$^+$, [Au(Phenyl)(8-H-Quin)]$^+$. The relative energy (kJ mol^{-1}) of the conformer has been plotted against the quinoline ligand's torsion angle (°), *d* (see Figure 4.11 for torsion angle *d*). Torsion angles: (i), 94.13°; (ii), 204.13°; (iii), −12.68°; (iv), 47.32°; (v), 97.32°; (vi), 4.63°; (vii), 54.63°; (viii), 114.63°. Note conformers or rotamers (viii)′ and (iv)′ are slightly higher energy structures, but can essentially be seen as being degenerate to conformers (viii) and (iv), respectively.

In all three cases, the DFT-calculated conformational/rotamer energy plots exhibited well-defined points of global energy minima, global energy maxima, local energy minima and local energy maxima. Selected points of interest have been labelled (i)–(viii) in Figure 4.11 and have been discussed in relation to individual compounds below.

[Au(L2)(8-H-Quin)]$^+$: The conformer energies increase at an increasing rate, from the energy minimum structure (i) to the energy maximum structure (ii), as torsion angle *d* is

increased from 94.1° to 204.1°. Point (i) corresponds to the conformer where the distance between quinonline group and the cyclohexyl group has been kept to a maximum, thereby limiting van der Waals repulsion between the two ring systems. Consequently, this is the least sterically hindered structure and so it is also the lowest-energy structure. Point (ii) corresponds to the confromer where the distance between the quinoline co-ligand and the cyclohexyl group is at its smallest. Because this is the most sterically hindered conformer/rotamer, it has a large amount of structural (steric) strain. This makes (ii) the most unstable structure (highest-energy conformer). The plot is approximately symmetrical about the *d* ~ 204° axis. ΔE for the plot is 90.10 kJ mol^{-1}. There are no well-defined points of local maxima, and thus no saddle points are present.

[Au(L1)(8-H-Quin)]$^+$: The conformer energy decreases between points (iii) and (iv) (global energy maximum and minimum, respectively, *d* = –12.7° to 47.3°), then increases from (iv) to (v) ~47° to ~97° (point of local energy maximum). Conformer (iii) has the quinoline ligand oriented too close to the adjacent mesityl ring and as a result there is a high degree of steric hindrance and structural instability – this is a very unfavourable conformation (not likely to be observed in reality). Conformer (iv) exhibits an intramolecular π-stacking interaction between the quinoline and the mesityl group. This results in additional structural stability and is the reason why (iv) is the low energy conformer. Conformer (v), corresponds to a conformer where the π-stacking interaction (inter-centroid distance: 3.924 Å) seen in (iv) has been broken. Therefore structure (v) provides a convenient way of measuring the energy penalty that the structure must pay in order to break the π-stacking interaction (in this case 12.27 kJ mol^{-1}). This is a significantly different trend to what is seen for the [Au(L2)(8-H-Quin)]$^+$ conformers, with the difference arising from the presence of the π-stacking interaction in the Au(L1) series and the lack of the interaction in the Au(L2) series. The plot is approximately symmetrical about the *d* ~ 97° axis. The symmetry-ideal torsion angle is likely 90° for the compound; the ~7° offset is probably the result of bias due to the scan direction. It is possible that when a reverse scan is performed, the averaged data points will yield a trajectory-independent conformational energy profile. ΔE for the plot is 36.7 kJ mol^{-1}.

[Au(L1)(Phen)]$^+$: This plot exhibits many of the trends observed for the [Au(L1)(8-H-Quin)]$^+$ conformer series. This is because both sets of compounds exhibit π-stacking interactions. In this case the intramolecular π-stacking interactions occur between the metal-bound quinoline ligand ring system and one of the two phenyl ring substituents of the pincer ligand. The low energy conformer (viii) is the conformer where the π-bonding interaction is the strongest and thus the lowest energy structure due to the stabilizing effect of the π-stacking interaction. Conformer (vii) is the conformer where the π-stacking interaction has been

broken, and as a result the structure has paid an energy penalty, ensuring a higher energy structure when compared to (vii). The conformer profile is significantly less symmetrical when compared to the Au(L1) and Au(L2) profiles. It is possible that this asymmetry has been caused by scan bias. This presumably occurs as a result of persistence of the intramolecular π-π interaction even when the quinoline and phenyl ring systems are approximately parallel (*d* ~ 90°). The plot is roughly symmetrical about the *d* ~ 54° axis. ΔE for the plot is 28.2 kJ mol^{-1}.

The π-stacking interaction strength can be viewed as the energy difference between conformer pairs (iv) and (v) and (vii) and (viii), because this corresponds to the energy needed to break the π-stacking interaction. The strength of benzene dimer π-stacking interactions has been experimentally measured at 8-12 kJ/mol.[135] These experimental measurements are very close to the calculated π-stacking interaction strengths: Au(L1), 12.3 kJ mol^{-1}; Au(Phen), 8.2 kJ mol^{-1}. This is an expected result as both are benzene derivatives, which affirms the assignment and accounts for the tilt of the quinoline ligand away from orthogonality relative to the AuN_4 plane in each case. This is not seen in the chelate with cyclohexyl rings because π-stacking interactions are absent. The rotamer analysis performed here (Figure 4.11) therefore neatly confirms the π-stacking origin of the "tilted quinoline" conformational effect seen in the present class of pincer chelates with quinoline co-ligands and aryl ring substituents.

4.3.5 Electronic structures: pincer chelates of d^8 metals with quinoline co-ligands

The DFT-calculated structures of all compounds listed in Table 4.5 amount to a significant body of structural and electronic data. All Gaussian job files (input, output, and formatted checkpoint files) are available in the electronic Appendix accompanying this dissertation.

An analysis of the data in Tables 4.6 and 4.7, and the trends prevalent therein, is presented in this Section. The overall aim of the study is to gain a computationally-based theoretical understanding of what factors affect the nonbonded interaction between the metal ion and the atom affixed to position 8 of the quinoline co-ligand in this series of chelates.

Selected correlations are plotted in Figure 4.13. The atomic overlap parameter β in Tables 4.6 and 4.7 is based on the van der Waals radii of the metal and interacting atom (Figures 4.11 and 4.13) appended to position 8 of the quinoline ring. This was calculated according to the method of Weisstein.[136] Suitable van der Waals radii for metals were employed in the calculations: Au = 1.66(Å)[137], Pt = 2.06 (Å), Pd = 2.05 (Å).[138] One limitation to using these van der Waals radii for metals is that the radii size should be adjusted for oxidation state and

such values are limited in the literature. The van der Waals radii values that are reported are the most appropriate values to the best of my knowledge. This is significant because the Au(III) ion will be substantially smaller and harder when compared to Au(I), for example. It is possible that there is see some degree of absolute error in the β calculation – however there will be no relative error because any errors arising from using an incorrect metal van der Waals radius will carry over into all calculations. This parameter will be further discussed in the Section 4.3.5

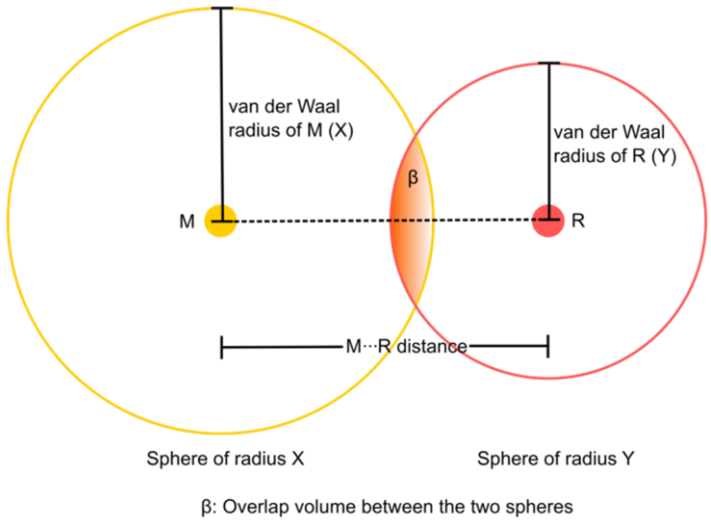


Figure 4.13. A diagram showing a graphical representation of the volume of sphere overlap, β, which was calculated according to Weisstein[136]. $\beta = \frac{\pi(X+Y-l)^2(l^2+2lY-3Y^2+2lX+6XY-3X^2)}{12l}$, where β is the overlap volume of two spheres of radii X (van der Waals radius of M) and Y (van der Waals radius of Q). l is the distance between the atom centers (i.e., the M···Q distance).

Table 4.6. Observed correlation coefficients, R^2, for the monoatomic halide series of Au(III), Pt(II), and Pd(II) chelates of deprotonated ligands H_2L1 and H_2L2. Correlations were derived using the correlation function found in Excel's data analysis ToolPak plugin. Refer to Figures 4.11 and 4.12 for a graphical explanation of the structural features that were probed during the analysis.

Trend	[Au(L1)(8-Q-Quin)]$^+$	[Au(L2)(8-Q-Quin)]$^+$	[Pd(L1)(8-Q-Quin)]	[Pd(L2)(8-Q-Quin)]	[Pt(L2)(8-Q-Quin)]	[Pt(L2)(8-Q-Quin)]
M···Q distance (Å) vs VDW radii of Q (Å)	0.9750	0.9648	0.9992	0.9999	0.9954	0.9985
Electronegativity of Q[139] vs M···Q distance (Å)	–0.1257	–0.1676	0.0684	0.0850	0.1192	0.1046
HOMO-LUMO gap (eV) vs M···Q distance (Å)	0.5088	–0.8102	–0.8789	–0.8144	–0.6515	–0.3094
Hardness of Q[140] vs M···Q distance (Å)	–0.9725	–0.9734	–0.9066	–0.9036	–0.8930	–0.8880
M–N(quin) distance (Å) vs M···Q distance (Å)	0.9625	0.9587	0.8568	0.9902	0.8407	0.8951
6s [valence] electron occupancy of metal* vs M···Q distance (Å)	–0.9020	–0.8811	–0.9346	–0.9242	–0.9031	–0.9509
$6p_z$ [valence] electron occupancy of metal* vs M···Q distance (Å)	0.8223	0.9965	0.9764	0.9770	0.9017	0.9677
ρ(M···Q) (au) vs M···Q distance (Å)	0.8157	0.8908	0.9991	0.9964	0.9228	0.9866
ρ(M···Q) (au) vs VDW radii of Q (Å)	0.9236	0.9787	0.9983	0.9958	0.9544	0.9936
ρ(M···Q) (au) vs M–N(quin) distance (Å)	0.9322	0.9734	0.8497	0.9749	0.6061	0.9494
ρ(M···Q) (au) vs Inter–Centroid distance (Å)	–0.9701	0.9659	–0.9078	0.3823	–0.4492	–0.1652
ρ(M···Q) (au) vs α [valence electron occupancy of M]*	0.7053	0.9005	0.9794	0.9788	0.9893	0.9945
M–N(quin) distance (Å) vs Torsion angle d (°)	–0.8850	0.2763	–0.9762	–0.8878	–0.9327	0.3459
ρ(M···Q) (au) vs 6s [valence] electron occupancy of M	–0.8837	–0.8894	–0.9351	–0.9469	–0.9219	–0.9785
ρ(M···Q) (au) vs β (Å^3)**	0.9779	0.9997	0.9979	0.9988	0.9987	0.9995

*α = $6p_z$ electron occupancy of the metal. For Pd^{2+} the $5p_z$ orbital is considered. **$\beta = \frac{\pi(X+Y-l)^2(l^2+2lY-3Y^2+2lX+6XY-3X^2)}{12l}$ (see Figure 4.13).

Table 4.7. Selected DFT–calculated structural and electronic data (quinolines substituted by a single atom). M···R atomic overlaps (van der Waals radii) determined via trigonometric methods are included.

Compound	M···Q distance (Å)	M—$N_{(quin)}$ (Å)	ρ(M···Q) (au)	α*	β**
$[Au(L1)(8\text{-}F\text{-}Quin)]^+$	2.858	2.281	0.0160	0.0606	0.1758
$[Au(L1)(8\text{-}Cl\text{-}Quin)]^+$	3.100	2.302	0.0187	0.1154	0.2493
$[Au(L1)(8\text{-}Br\text{-}Quin)]^+$	3.179	2.315	0.0199	0.1319	0.2914
$[Au(L1)(8\text{-}I\text{-}Quin)]^+$	3.276	2.331	0.0221	0.0960	0.3627
$[Au(L1)(8\text{-}H\text{-}Quin)]^+$	2.809	2.250	0.0000	0.0545	0.0057
$[Au(L2)(8\text{-}F\text{-}Quin)]^+$	2.749	2.216	0.0202	0.0710	0.3404
$[Au(L2)(8\text{-}Cl\text{-}Quin)]^+$	2.976	2.236	0.0245	0.0977	0.4829
$[Au(L2)(8\text{-}Br\text{-}Quin)]^+$	3.059	2.249	0.0256	0.1114	0.5351
$[Au(L2)(8\text{-}I\text{-}Quin)]^+$	3.173	2.265	0.0271	0.1198	0.5911
$[Au(L2)(8\text{-}H\text{-}Quin)]^+$	2.717	2.187	0.0121	0.0660	0.0437
[Pd(L1)(8-F-Quin)]	2.893	2.155	0.0144	0.0599	1.0024
[Pd(L1)(8-Cl-Quin)]	3.093	2.166	0.0175	0.0825	1.4081
[Pd(L1)(8-Br-Quin)]	3.176	2.165	0.0184	0.0947	1.5222
[Pd(L1)(8-I-Quin)]	3.283	2.161	0.0200	0.1016	1.6789
[Pd(L1)(8-H-Quin)]	2.708	2.129	0.0121	0.0550	0.6586
Pd(L2)(8-F-Quin)]	2.831	2.151	0.0162	0.0633	1.1826
[Pd(L2)(8-Cl-Quin)]	3.032	2.178	0.0195	0.0850	1.6283
[Pd(L2)(8-Br-Quin)]	3.104	2.186	0.0209	0.0956	1.8021
[Pd(L2)(8-I-Quin)]	3.197	2.189	0.0232	0.1006	2.0435
[Pd(L2)(8-H-Quin)]	2.646	2.125	0.0133	0.0579	0.7951
[Pt(L1)(8-F-Quin)]	2.959	2.196	0.0144	0.0599	0.8366
[Pt(L1)(8-Cl-Quin)]	3.221	2.215	0.0158	0.0752	0.9887
[Pt(L1)(8-Br-Quin)]	3.240	2.207	0.0188	0.0976	1.3108
[Pt(L1)(8-I-Quin)]	3.348	2.200	0.0203	0.1051	1.4488
[Pt(L1)(8-H-Quin)]	2.742	2.169	0.0126	0.0557	0.6033
[Pt(L2)(8-F-Quin)]	2.886	2.065	0.0175	0.0580	1.0401
[Pt(L2)(8-Cl-Quin)]	3.087	2.221	0.0205	0.0805	1.4525
[Pt(L2)(8-Br-Quin)]	3.163	2.229	0.0217	0.0912	1.5992
[Pt(L2)(8-I-Quin)]	3.297	2.213	0.0222	0.0921	1.6426
[Pt(L2)(8-H-Quin)]	2.658	2.055	0.0156	0.0500	0.7917

*α = $6p_z$ electron occupancy of the metal. For Pd^{2+} the $5p_z$ orbital is considered. **$\beta = \frac{\pi(X+Y-l)^2(l^2+2lY-3Y^2+2lX+6XY-3X^2)}{12l}$ (see Figure 4.13).

Table 4.8. Table of parameters for the halide series atoms and hydrogen.

Identity of R	Van der Waals radii of Q (Å)[141]	Hardness of Q[140]
F	1.47	7.01
Cl	1.75	4.68
Br	1.85	4.22
I	1.98	3.69
H	1.20	6.43

4.3.5.1 Electronic structure trends: pincer chelates of d^8 metals with quinoline co-ligands

The reader is advised that in the discussion of the trends presented in Tables 4.6 and 4.7, the "$6p_z$" and "6s" orbitals lables also refer to the $5p_z$ and 5s orbitals (in the case of Pd(II)).

van der Waals radius of atom Q (Å) vs M···Q distance (Å)

The van der Waals radius of atom Q was a very good predictor of the M···Q distance across all structures, where strong directly proportional relationships were observed (correlation coefficients: 0.9750 for Au(L1), 0.9648 for Au(L2), 0.9992 for Pd(L1), 0.9999 for Pd(L2) , 0.9954 for Pt(L1) and 0.9985 for Pt(L2). As the van der Waals radii of atom Q increased, the M···Q distance increased. The correlations were particularly strong for the Pd(II) series, where near perfect correlations were observed. This observation is supported by the steric trends observed in the structure (discussed later in this Chapter) where for Q atoms of small atomic radii, the M···Q distance is a minimum due to a lack of significant steric strain on the structure, with the opposite being true for Q atoms of large atomic radii, where the increased radius of the atom causes steric structural strain, which the compound must accommodate for by maximising the M···Q distance. This correlation might be fortuitous and linked to the underlying and dominant correlation with the van der Waals radius of R.

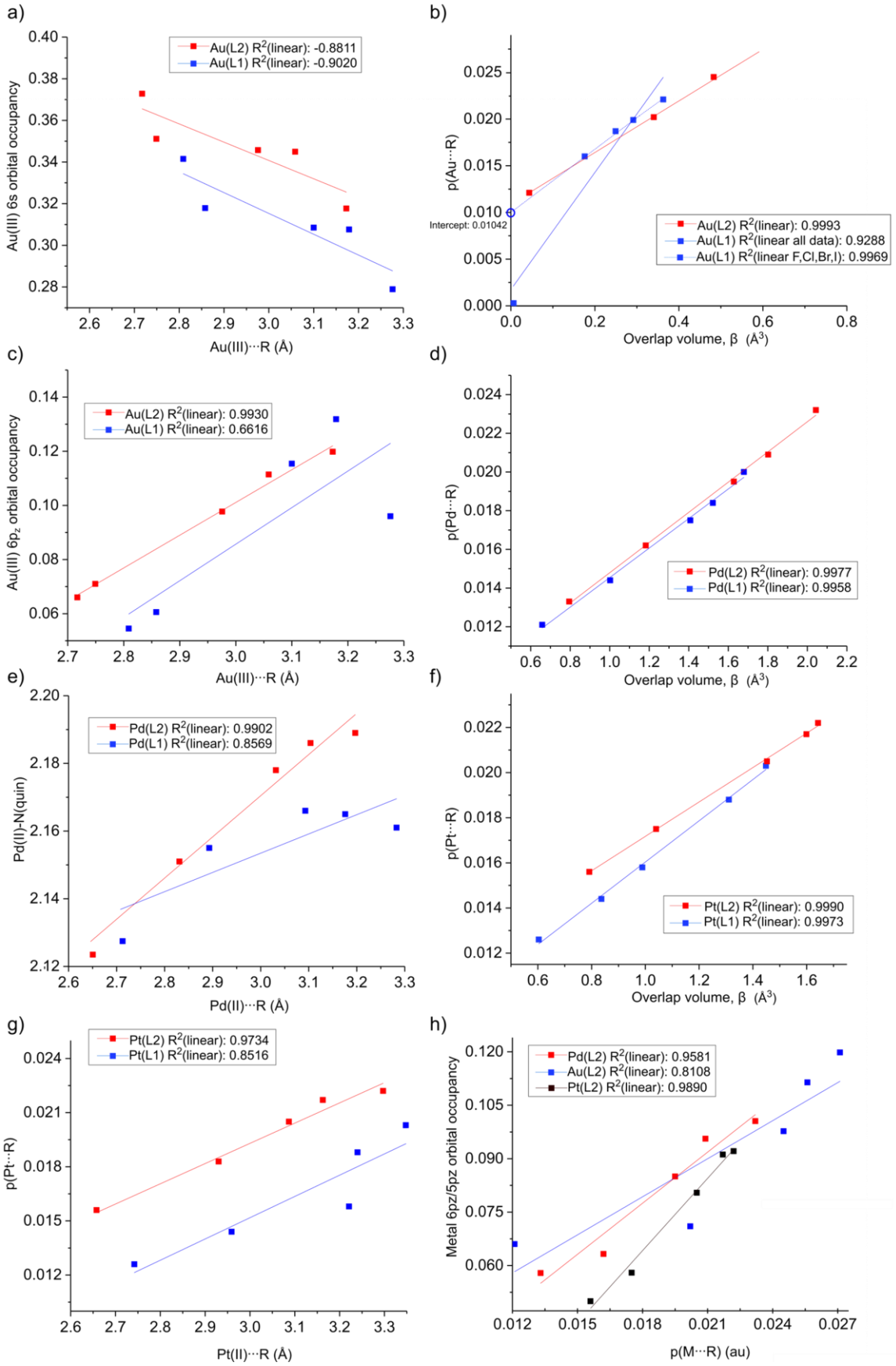


Figure 4.14. Plots of selected data from Table 4.7. These plots are discussed further in Section 4.3.5.1.

Electronegativity of Q vs M···Q distance (Å)

Across the structures analysed (Tables 4.6 and 4.7), no correlation was observed between the M···Q distance and the electronegativity of the heteroatom Q (correlation coefficients: –0.126 for Au(L1), –0.168 for Au(L2), 0.0684 for Pd(L1), 0.0850 for Pd(L2) , 0.119 for Pt(L1) and 0.105 for Pt(L2). This is an unexpected result, especially because hardness has been shown to be a reliable predictor of M···Q distance in our systems, and thus one would assume that electronegativity would also be a good predictor, given that absolute electronegativity is correlated to absolute hardness.[142] The lack of a correlation here suggests that either the correlation with hardness as noted above might be spurious or that the strength of the M···Q interaction is weak and thus negligibly impacted on by electronegativity effects as these operate mainly in covalent bonds.

HOMO-LUMO gap energy (eV) vs M···Q distance (Å)

No significant correlations were found between the HOMO-LUMO gap energy and M···Q distance or the ρ(M···Q) value. Thus the energy of the HOMO-LUMO gap does not appear to alter or be altered by the M···Q distance or the ρ(M···Q) value (**Appendix B**). In addition neither the HOMO nor the LUMO energies correlated to either of the probed M···Q distance and ρ(M···Q) value, with no significant relationships observed (**Appendix B**).

ρ(M···Q) (au) vs Inter-Centroid distance (Å)

ρ is defined as the electron density at the bond critical point of a bond or interaction. This value can be used to quantify the strength of an interaction. There is a strong correlation seen for the Au(L1), Au(L2) and Pd(L1) compound series but not for the remaining Pt or Pd derivatives (correlation coefficients: –0.970 for Au(L1), 0.966 for Au(L2), –0.908 for Pd(L1), 0.382 for Pd(L2), –0.449 for Pt(L1) and –0.165 for Pt(L2)). It is unclear why these trends are so inconsistent—with the correlations for Au(L1) and Pd(L1) being strongly inversely proportional, and the correlation for Au(L2) being strongly directly proportional. One might expect there to be no correlation for the M(L1) compound series, given that π-stacking interactions are occurring which would likely result in the inter-centroid distance remaining relatively constant regardless of the identity or size of the interacting atom Q (given the energy penalty that the structure would need to pay to overcome this π-stacking force, see Figure 4.11). Similarly, the L2 ligand series of structures would also exhibit no correlation, especially given that (due to steric repulsion effects) it is optimally favorable for the structure to keep the quinoline group as far away from either cyclohexyl group as is possible (Figure

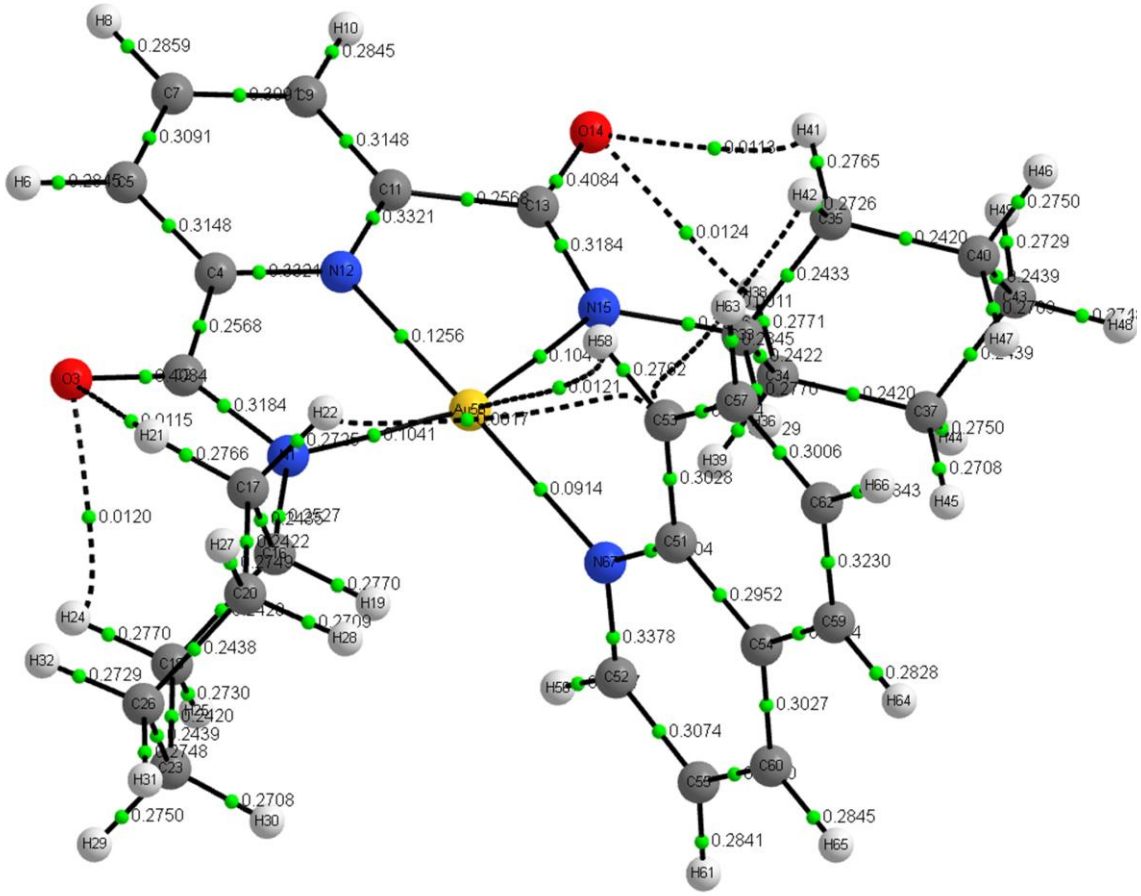


Figure 4.15. AIMAII output of the calculated structure of $[Au(L2)(8\text{-H-Quin})]^{+}$. The green dots are bond critical points and the number adjacent to the dots is the ρ value (electron density) at that point. In this case, the ρ(M···Q) (where Q = H) value is 0.0121 au.

4.14). A possible explanation of this could be that as the bulkiness of atom Q increases, the M—$N_{(quin)}$ distance increases to accommodate for the increased structural strain. Consequently, the quinoline co-ligand has a greater degree of freedom movement and repositions itself in a way that is not yet fully understood.

6s [valence] electron occupancy of metal vs M···Q distance (Å) and ρ(M···Q) (au)

It was observed that as the electron density of the 6s orbital of the metal (5s in the case of Pd^{2+}) decreases, the M···Q distance increases and so does electron density of the bond critical point between M and R. This likely occurs because as the Q-group is moved closer to the metal center, the vacant 6s/5s orbital gains some electron density as a result of through-space donation of electron density from the Q-group to the metal. The trends observed simply reflect the electrostatic interactions caused by the electron-poor metal ion.

M···Q distance (Å) vs ρ(M···Q) (au)

A significant trend reflected in the data is that as the M···Q distance increases, ρ(M···Q) also increases. This seems counter-intuitive, because in the case of formal bonding one would expect a short bonding interaction to be stronger such that as the M···Q distance increased the ρ(M···Q) would decrease. To understand this seemingly paradoxical trend we note that as the M···Q distance increases the electron density of the Au($6p_z$) orbital (measured by the Au($6p_z$) orbital occupancy parameter) increases as well. As a result, and due to the increased electron density of the Au($6p_z$) orbital, the interaction does indeed become stronger, based on the electron density at the bond critical point, which is evidenced by the increasing ρ(M···Q) value (ρ(M···Q) correlates with $6p_z$ orbital occupancy in all structures analysed, correlation coefficients: 0.70 for Au(L1) and 0.90 for Au(L2) (Table 4.6)).

The correlation coefficient between the van der Waal radii of Q and Au($6p_z$) orbital occupancy are: 0.808 for Au(L1) and 0.969 for Au(L2) (**Appendix B**). This shows that steric factors (in the form of the size of Q) play a significant role in populating the $6p_z$ orbital of Au. It seems that as the valence shell of atom Q increases in size, the amount of orbital overlap between Au and Q also increases. As a result, the Au(III) ion is forced into acting as an electron acceptor where electron density from atom Q is transferred into the $6p_z$ orbital of Au. This greater degree of orbital overlap increases the strength of the M···Q "bonding interaction" as sensed at the bond critical point. There are a number of literature reports that show that Au(III) can form apparent 5-coordinate complexes.[123, 143-146] These nominal 5-

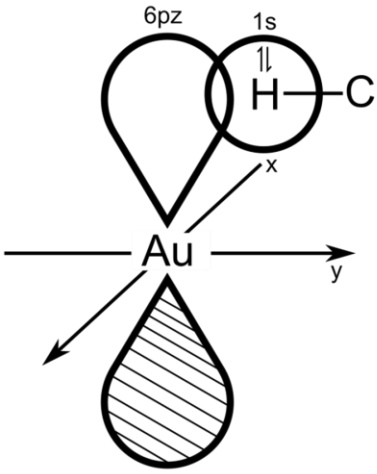


Figure 4.16. Diagram illustrating the orbital overlap present in the $[Au(Lx)(8\text{-H-Quin})]^+$ structure. As the degree of orbital overlap increases, the electron occupancy of the $6p_z$ orbital increases. Since the $6p_z$ orbital is vacant, the interaction is of the donor–acceptor type.

coordinate species could possibly be forming due to a similar orbital overlap, where the Au $6p_z$ orbital and the electron valence shell of the axially interacting atom overlap as depicted in Figure 4.16.

M-N(Quin) distance (Å) vs M···Q distance (Å)

The M-$N_{(quin)}$ distance is very well correlated to the M···Q distance. (Correlation coefficients: 0.963, Au(L1); 0.959, Au(L2); 0.857, Pd(L1); 0.990, Pd(L2); 0.841, Pt(L1); and 0.895 for Pt(L2).) These correlations suggests that as the M···Q distance increases, the strain on the structure also increases, and so to accommodate for this structural strain, the structure distorts by commensurate elongation of the M—$N_{(Quin)}$ distance. Thus the increases in the M—$N_{(quin)}$ distance occurs as a result of the increases in M···Q distance. The fact that M—$N_{(quin)}$ changes in proportion to M···Q indicates that 5-coordination is unfavourable and as a result of this, M—$N_{(quin)}$ lengthens as the ligand is forced by steric repulsion to move away from the chelated metal ion. This seems to be a steric response, as the van der Waals radius of atom Q becomes larger it is forced to interact with the metal ion more closely and so the degree of steric repulsion increases. This causes additional strain on the compound which is counterbalanced by the elongation of the M—$N_{(quin)}$ bond distance. This observation is presented graphically in Figure 4.17.

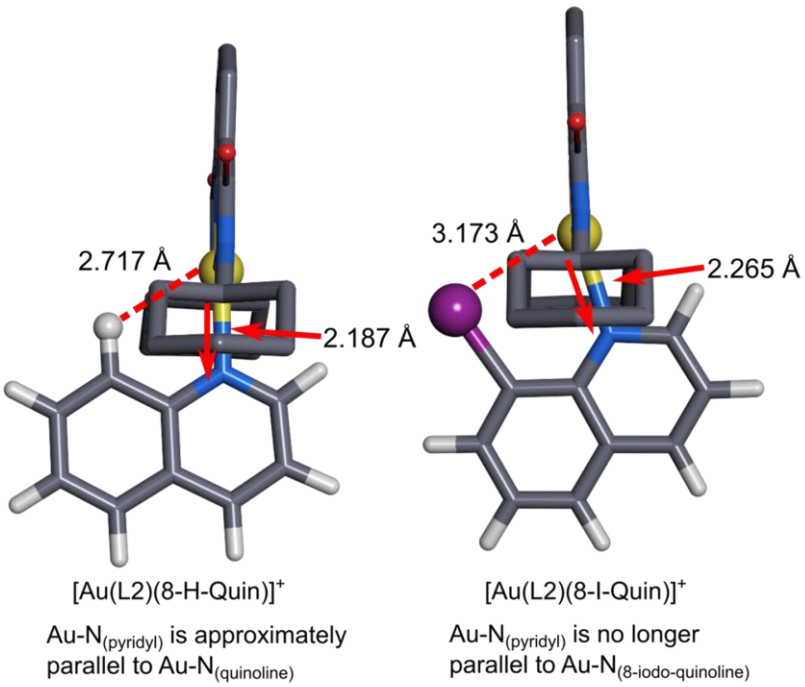


Figure 4.17. Diagram emphasising how M—$N_{(quin)}$ increases as M···Q increases. $N_{(pyridyl)}$—Au—$N_{(quinoline)}$ = 177.80° and $N_{(pyridyl)}$—Au—$N_{(8\text{-iodo-quinoline})}$ = 164.62°. Some hydrogen atoms have been excluded for visibility.

ρ(M···Q) (au) vs M-N(quin) distance (Å)

Relatively strong directly-proportional relationships exist. For example, as the electron density of the bond critical point (BCP) of M···Q increases, the M—$N_{(quin)}$ distance for all complexes, except in the case of Pt(L1) also increase. Correlation coefficients: 0.932, Au(L1); 0.973, Au(L2); 0.850, Pd(L1); 0.975, Pd(L2); 0.606, Pt(L1); 0.949, Pt(L2). This trend suggests that the M···Q interaction becomes stronger with greater elongation of the M—$N_{(quin)}$ bond. Because it has been established that the M···Q distance and ρ(M···Q) are directly proportional, it follows that the ρ(M···Q) value increases, and so does the M···Q distance. This results in steric stress exerted in the structure (discussed above: M-N(quin) distance vs M···Q distance, Figure 4.17) and thus the M—$N_{(quin)}$ bond lengthens in an effort to maintain the greatest possible distance away from R. It is not entirely clear why the Pt(L1) series of compounds does not exhibit this relationship as strongly as all the other complexes. This is an area that requires further study.

It is possible that the ligand system we chose hinders 5-coordination from occurring (Figure 4.16). Many of the nominally 5-coordinate Au(III), Pt^{2+} and Pd^{2+} ($Au^{123, 143-146}$, $Pt^{147-150}$, $Pd^{149, 151-153}$) complexes (Figures 4.18 and 4.22) are achieved through use of a 1,10-phenanthroline ligand where the axially interacting atom is a nitrogen with a lone pair and is acting as a typical Lewis base. The quinolines used in this study have only one such nitrogen, the axially interacting atoms (in the 8-position on quinoline) are mostly suited to

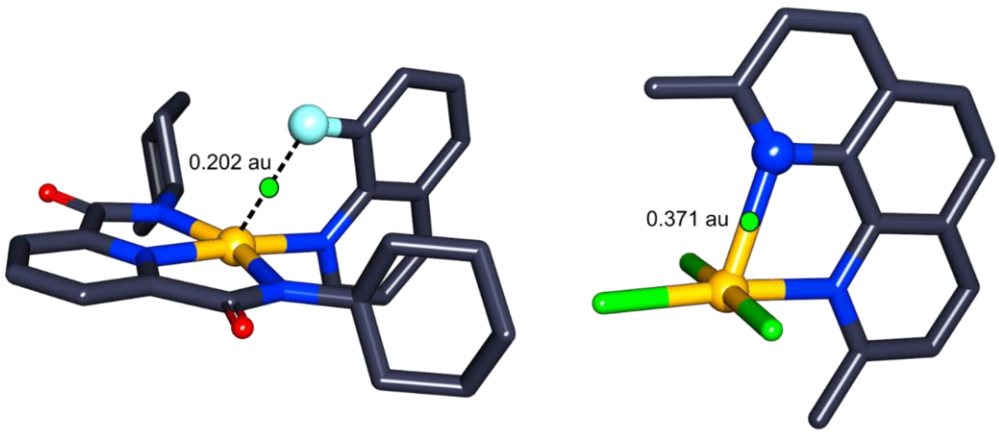


Figure 4.18. Diagram showing the structural differences between 5-coordinate Au(III) structures in the literature (CDMPAU) and a Au(III) structure that was analysed as part of this study. Hydrogen atoms have been excluded for visibility. The ρ(Au···F) value for $[Au(L2)(8\text{-F-Quin})]^+$ is 0.202 au and the ρ(Au-N) value is 0.371 au.

forming non-bonding interactions (Figures 4.18 and 4.22).

An example of a nominally 5-coordinate Au(III) structure from the literature will be discussed in detail in Section 4.3.5.3. Although the two tridentate ligands used in the study are rigid, the substituted quinoline that is bonded in the 4 position of Au(III) is relatively free to move (laterally) in order to allow the system to maintain a large M···Q distance. It is true that in doing this the square planar conformation around gold is distorted, but this might be more energetically favoured than having the Q atom get too close to M (due to steric factors). Perhaps a better ligand system would be one where the quinoline was in a more fixed position where the M-$N_{(quin)}$ bond would not have the same degree of freedom.

Discussion of parameter Beta: ρ(M···Q) (au) vs β (Å^3)**

Overall the β parameter (defined in Figure 4.13) was the best predictor of the ρ(M···Q) value, as β increased, ρ(M···Q) increased in a directly proportional manner. Correlation coefficients: 0.978, Au(L1); 0.999, Au(L2); 0.998, Pd(L1); 0.999, Pd(L2); 0.999, Pt(L1); 0.999, Pt(L2). When this parameter was considered we were able to see a trend where the ρ(M···Q) value increased as the orbital overlap between the valence shell of Q and the electron occupancy of the ($5p_z$ for Pd^{2+}, $6p_z$ of Au(III) and Pt^{2+}) orbital of M increased (**Appendix B**). The strong correlation between parameter β and the ρ(M···Q) value suggests that the β parameter is a very effective way to probe the strength of the M···Q interaction. This is an expected result because β is essentially a simplified model that describes the volume of overlap between two spheres separated by the M···Q distance and having radii equal to the van der Waals radius of M and atom Q. This parameter effectively accounts for the overlap of the valance shells of the atoms, which is the basis for chemical bonding (Figure 4.13). This consideration is important because, even though the M···Q distance is a minimum in the $[Au(L1)(8\text{-H-Quin})]^+$ structure, the degree of orbital overlap (and thus bond strength) is much less when compared to an Q atom of larger atomic radii in the series, such as iodine in the $[Au(L1)(8\text{-I-Quin})]^+$ structure. This is naturally the case, given how much larger the van der Waals radius of iodine is when compared to hydrogen (H: 1.2 Å, I: 1.98). This suggests that there is greater orbital overlap occurring in the elements of larger atomic radii and thus a stronger interaction occurs, despite the M···Q distance increasing at the same time.

The discrepancy between interaction distance and bond strength is highlighted by the structures RAHTEA[154] and BUQXUI,[155] which show that the length of a Pd^{2+}—Cl bond can be as large as 2.537 Å (RAHTEA[154]) and the length of a Pd^{2+}—H bond can be as small as

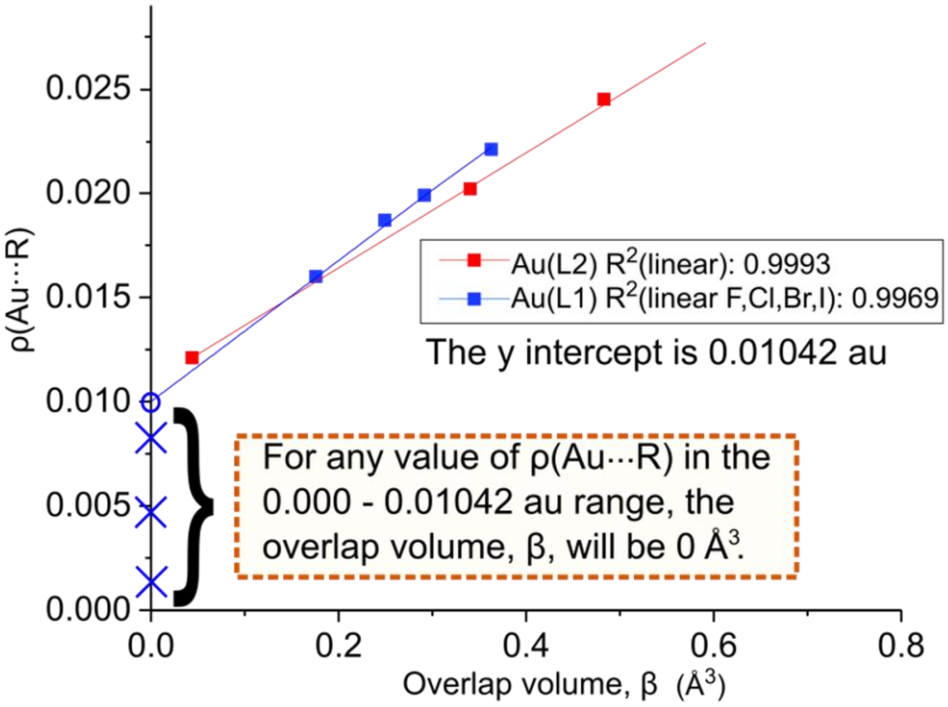


Figure 4.19. An annotated graph of the relationship between the β and ρ(Au···Q) parameters.

1.565 Å (BUQXUI[155]). This simple comparison shows that absolute M···Q distance alone is not a reliable metric to consider when determining the strength of a potential bonding integration. Consequently, we need to use information specific to the physical and chemical properties of the interacting atoms in order to properly quantify the characteristics of the M···Q nteraction. For this reason, factors such as the Laplacian of the electron density of the bond critical point and β were considered in the analysis. It is interesting to note that in all cases, β was a positive value, indicating that some degree of orbital overlap occurred for all of the compounds in the series.

The graph of ρ(M···Q) vs β for the Au(L1) series (Figure 4.19) exhibits an outlier where $[Au(L1)(8\text{-H-Quin})]^+$ did not conform to the linear trend of the remaining Au(L1) structures. The reason for this is that it is not possible to quantify negative orbital overlap, because no such physical parameter exists. According to calculations from the linear part of the series, any ρ(M···Q) value in the range of 0.000 to 0.0104 au should all have β values of 0, thus explaining why points with a coordinate value in this region are unreliable.

Torsion angle *d* (°) vs M-N(Quin) distance (Å)

When the torsion angle *d* for the quinoline-based ligand increases in magnitude, the structural strain increases because the quinoline ring is forced to move in closer to the

mesityl ring (L1 series) or the cyclohexyl ring (L2 series of compounds). This should result in the structure distorting to accommodate the increased structural strain. In particular, the M—$N_{(quin)}$ bond distance should increase in a similar way to what has been discussed for the ρ(M···Q) vs M—N(quin) distance and M···R vs M—N(quin) relationships. However, this trend is only seen for the M(L1) series of complexes and not for the M(L2) series. (Correlation coefficients: –0.8850, Au(L1); 0.276, Au(L2); –0.976, Pd(L1); –0.888, Pd(L2); –0.933, Pt(L1); 0.346, Pt(L2).) This is likely because π-stacking interactions occur in the L1 complex series but not in the L2 series (see Figure 4.6). The torsion angle *d* in the L1 compound series varies according to the M—$N_{(Quin)}$ distance in order to maintain a constant distance between the quinoline and the π-interacting mesityl group. If this distance was not maintained, the π-stacking would stop contributing to the stability of the structure and thus a large energy penalty of would need to be paid, which is thermodynamically unfavourable. (For example, this energy penalty would be 12.3 kJ mol^{-1} for $[Au(L1)(8\text{-H-Quin})]^+$; Figure 4.11.)

Thus, because of the unfavourable thermodynamics associated with breaking the M—$N_{(Quin)}$ bond, the torsion angle correlates with changes in the M—$N_{(Quin)}$ distance in the M(L1) series. For the M(L2) series, π-stacking interactions do not occur and so the quinoline co-ligand is positioned orthogonal to the MN_4 plane and parallel to the M—$N_{(pyridyl)}$ bond

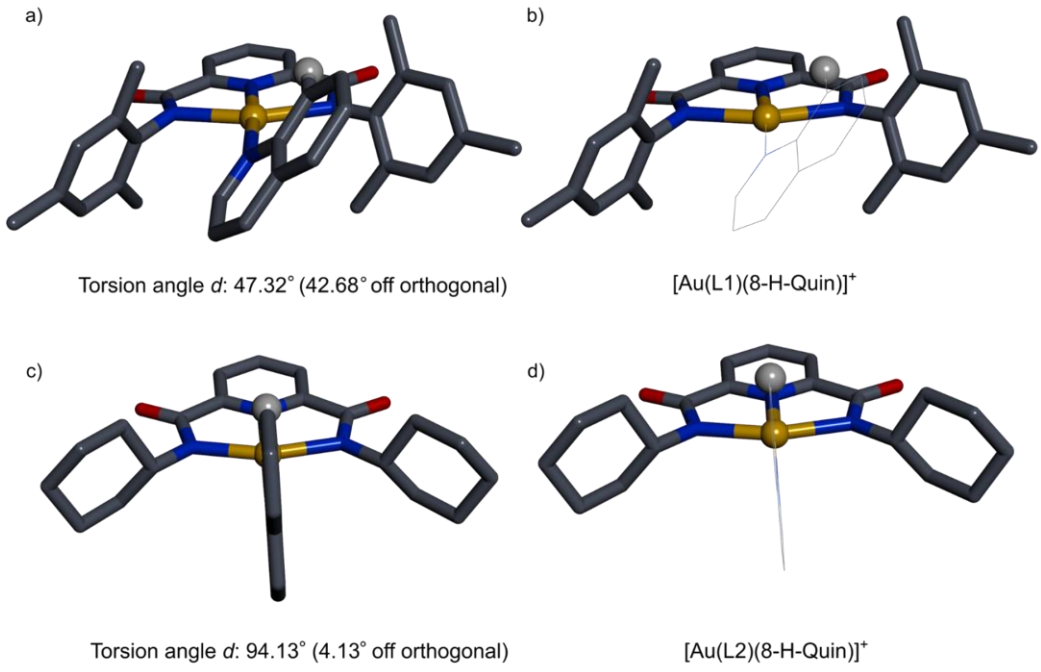


Figure 4.20. Diagram showing the variation in the orientation of the quinoline substituent. This has been quantified by examining torsion angle *d* for the conformers of the Au(L1) and Au(L2) series. Similar quinoline orientation trends are seen for the Pd(II) and Pt(II) congeners. For Parts b) and d), the quinoline group has been displayed as wire for visibility. All hydrogen atoms have been omitted for visibility, with the exception of hydrogen atoms that interact with the metal. Note that when torsion angle *d* = 90°, the plane of the quinoline will be orthogonal to the AuN_4 square plane.

(corresponding to a torsion angle *d* value of ~90°). This is in contrast to the L1 series, where the quinoline is at an off-orthogonal angle relative to the MN_4 plane (Figure 4.20). Therefore, for the M(L2) series, changes in the size of atom Q only seem to increase the M—$N_{(Quin)}$ distance while the torsion angle remains approximately constant, with the quinoline group orthogonal to the MN_4 plane. This explains why the correlation is observed for the M(L1) series only and not the M(L2) series.

4.3.5.2 AIMAll analysis of d^8 metal chelates

The structures that were used for AIM analysis had their geometries fully optimized using Gaussian 09W. The resultant AIM calculations were used identify bond critical points in the structures, with calculations being performed to give the electron density and the Laplacian of the electron density at the bond critical points. In this Section, the electron density of various bond critical points and the resultant classification of the interaction type will be discussed.

There are many examples of nominally 5- and 6-coordinate Au(III), Pt^{2+} and Pd^{2+} ions in the literature (Au[123, 143-146], Pt[147-150], Pd[149, 151-153]; see Figure 4.22 for examples). The majority of the Au(III) complexes were 4 coordinate (approximately square planar geometry, where all 4 interactions had sufficient electron density to be considered as dative covalent bonds). However there were two instances of compounds from the Au(III) cyclohexyl ligand series (L2) that exhibited a 5-coordinate geometry (these structures have been denoted by ** in Table 4.9). The AIM calculations clearly suggested that the M···Q interactions in these two compounds are covalent bonds with the compound exhibiting a distorted 5-coordinate geometry around the Au(III) metal centre. The results of the AIMAll analysis for all investigated complexes have been summarised in the Table 4.9.

As a way to test the suitability of the AIM method for our series of structures, a preliminary AIM analysis was performed on the compound shown in Figure 4.21. The compound that was used was a part of the polyatomic substituent series (**Appendix B**). The results of the AIM analysis showed that the bond critical point of the interaction between the methoxy oxygen and the gold center had a predicted electron density of approximately 33% of a formal dative covalent bond (Figure 4.21). The enhanced electron density between the Au and O in this structure is remarkable and the bond strength is far greater in magnitude than typical electrostatic interactions. This indicates that it could be possible for a similar interaction to have an interaction strength close to that of a formal bond and thus the formation of pseudo square pyramidal or pseudo octahedral Au(III), Pt(II) or Pd(II)

complexes could be possible. This result prompted a full investigation on the compounds and the results for the monoatomic series are given in Tables 4.9–4.11.

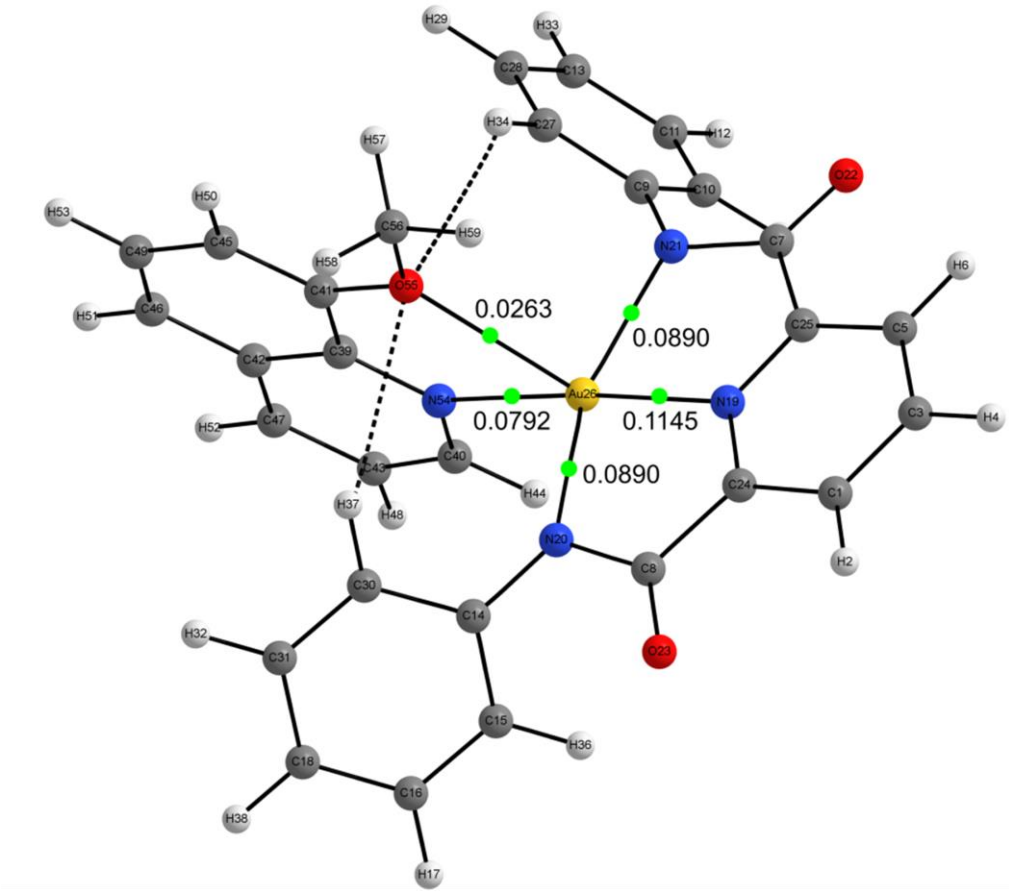


Figure 4.21. Image showing the output of an electron density analysis (AIM method; AIMAII software package) for [Au(Phen)(8-[OMe]-Quin)]$^{+}$. The green dots denote selected bond critical points while the number (in atomic units, au) gives a measure of the predicted electron density of the BCP along the interaction.

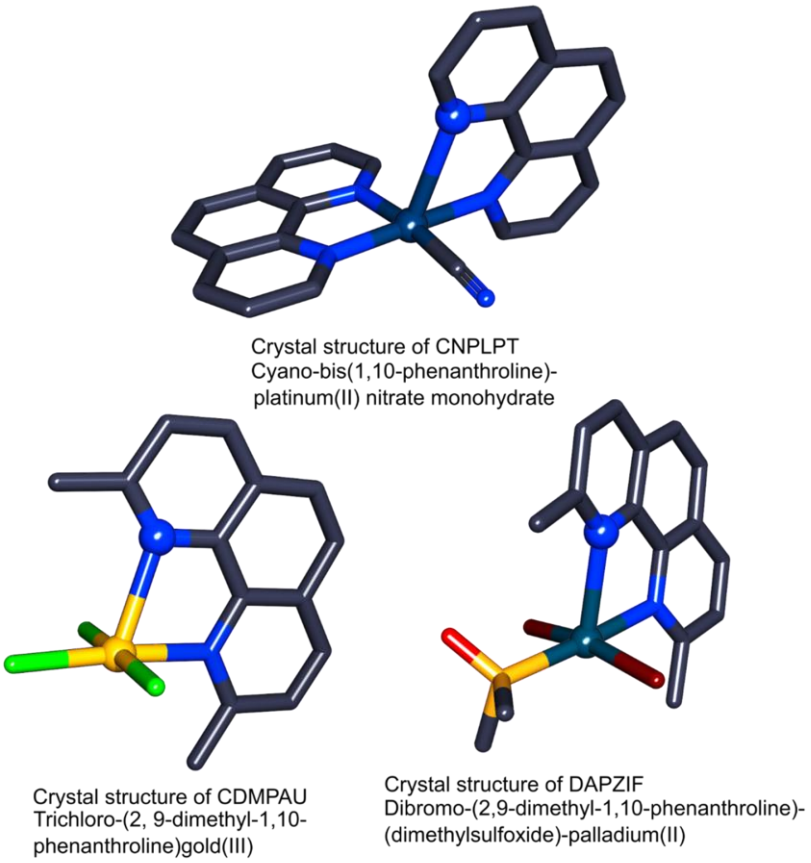


Figure 4.22. Selected examples from the literature of nominally 5-coordinate Au(III), Pt(II) and Pd(II) crystal structures. Hydrogen atoms have been excluded for visibility. The key question here is whether the axial M—N interaction behaves merely as an electrostatic interaction enforced by geometrical constraints of the phenanthroline ligand, or if sufficient electron density resides at a bond critical point for the interaction to be treated as a dative covalent bond. Structures are re-drawn from CSD codes: CNPLPT, CDMPAU and DAPZIF.

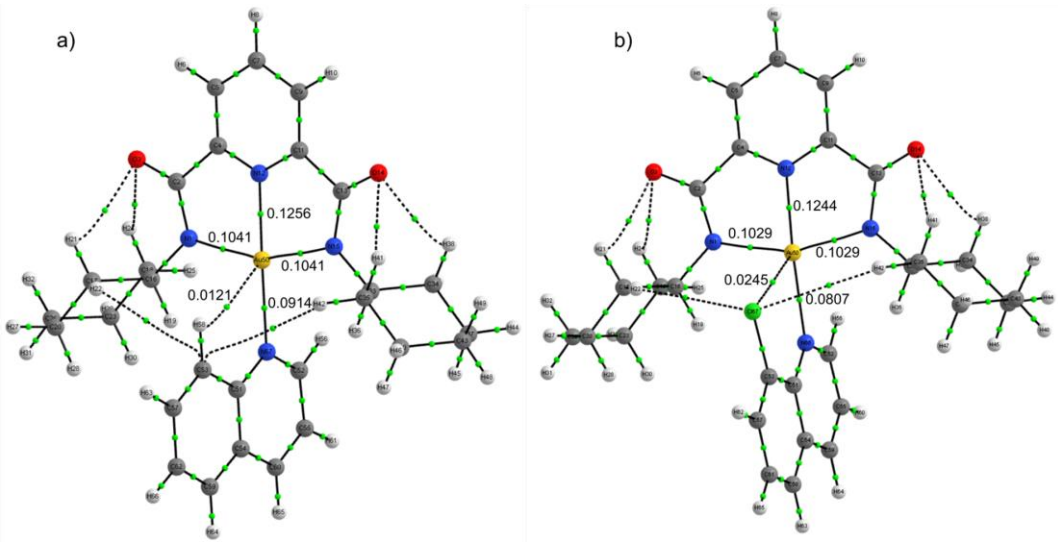


Figure 4.23. Examples of the output of AIM analysis on structures a) $[Au(L2)(8\text{-H-Quin})]^+$ and b) $[Au(L2)(8\text{-Cl-Quin})]^+$. Bond critical points are rendered as green spheres, with ρ data labels displayed over selected bond critical points.

Table 4.9. Selected electronic parameters for the monoatomic compound series (Au(III) complexes) that were obtained from AIMAII analysis of the DFT-calculated electron density. Two sample structures from the series have been given in Figure 4.22.

Compound	ρ(Au(III)···Q) (au)	Au(III)···Q (Å)	Bond character (%)* (BORSUY)
$[Au(L1)(8\text{-H-Quin})]^+$	0.0000	2.809	0.00
$[Au(L1)(8\text{-F-Quin})]^+$	0.0160	2.858	12.15
$[Au(L1)(8\text{-Cl-Quin})]^+$	0.0187	3.100	14.20
$[Au(L1)(8\text{-Br-Quin})]^+$	0.0199	3.179	15.11
$[Au(L1)(8\text{-I-Quin})]^+$	0.0221	3.276	16.78
$[Au(L2)(8\text{-H-Quin})]^+$	0.0121	2.717	9.19
$[Au(L2)(8\text{-F-Quin})]^+$	0.0202	2.749	15.34
$[Au(L2)(8\text{-Cl-Quin})]^+$	0.0245	2.976	18.60
$[Au(L2)(8\text{-Br-Quin})]^+$	0.0256	3.059	19.44**
$[Au(L2)(8\text{-I-Quin})]^+$	0.0271	3.173	20.58**

**The results of an AIMAII analysis indicated that the M···Q interactions in these two compounds are covalent bonds with the compound exhibiting distorted 5-coordinate geometry about the gold metal centre. *Bond character (%) calculated as: $\left(\rho(\mathrm{M}-\mathrm{Q})\Big/\rho(\mathrm{M}-\mathrm{O})\right)\times 100.$

ρ(M – O) values were used from the BORSUY structure (Scheme 4.1)

Table 4.10. Selected electronic parameters for the monoatomic compound series (Pd^{2+} complexes) that were obtained from AIMAII analysis of the DFT-calculated electron density.

Compound	$\rho(Pd^{2+}\cdots Q)$ (au)	$Pd^{2+}\cdots Q$ (Å)	Bond character (%)* (BORSUY)
[Pd(L1)(8-H-Quin)]	0.0121	2.708	9.19
[Pd(L1)(8-F-Quin)]	0.0144	2.893	10.93
[Pd(L1)(8-Cl-Quin)]	0.0175	3.093	13.29
[Pd(L1)(8-Br-Quin)]	0.0184	3.176	13.97
[Pd(L1)(8-I-Quin)]	0.0200	3.283	15.19
[Pd(L2)(8-H-Quin)]	0.0133	2.646	10.10
[Pd(L2)(8-F-Quin)]	0.0162	2.831	12.30
[Pd(L2)(8-Cl-Quin)]	0.0195	3.032	14.81
[Pd(L2)(8-Br-Quin)]	0.0209	3.104	15.87

[Pd(L2)(8-I-Quin)]	0.0232	3.197	17.62

*Bond character (%) calculated as: $\left(\rho(\mathrm{M}-\mathrm{Q})\Big/\rho(\mathrm{M}-\mathrm{O})\right)\times 100.$

Table 4.11. Selected electronic parameters for the monoatomic compound series (Pt^{2+} complexes) that were obtained from AIMAII analysis of the DFT-calculated electron density.

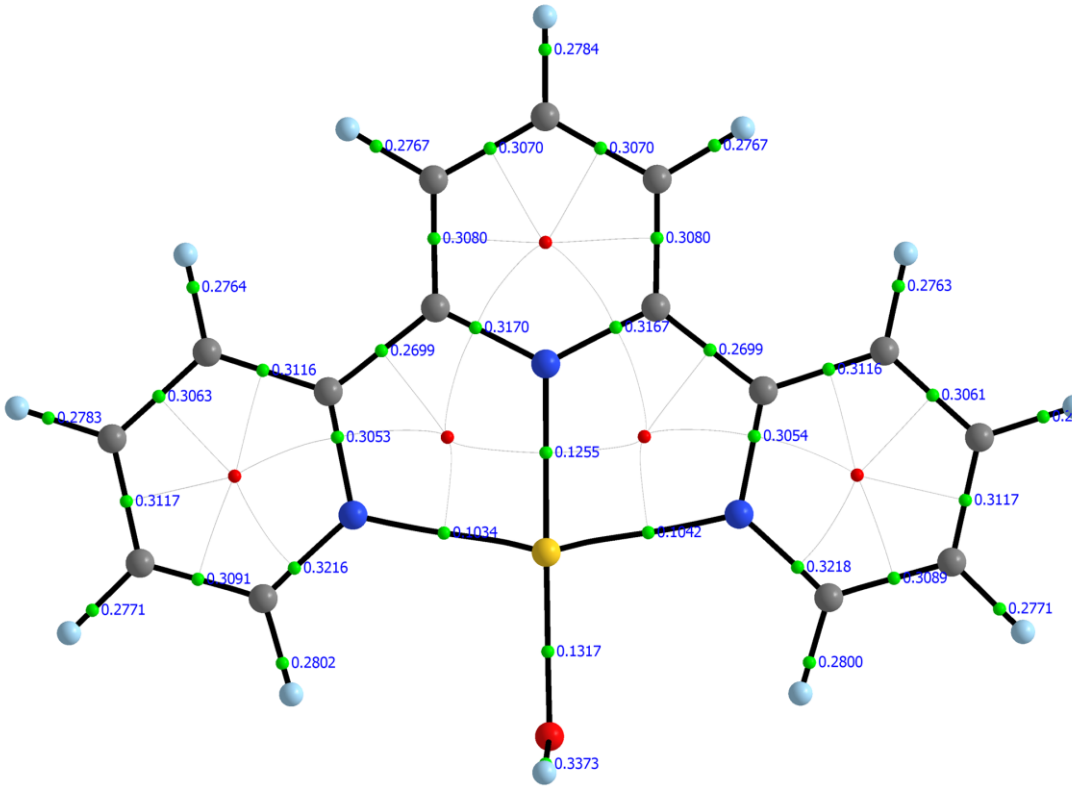
Compound	ρ(Pt^{2+}···Q) (au)	Pt^{2+}···Q (Å)	Bond character (%)* (BORSUY)
[Pt(L1)(8-H-Quin)]	0.0126	2.742	9.57
[Pt(L1)(8-F-Quin)]	0.0144	2.959	10.93
[Pt(L1)(8-Cl-Quin)]	0.0158	3.221	12.00
[Pt(L1)(8-Br-Quin)]	0.0188	3.240	14.27
[Pt(L1)(8-I-Quin)]	0.0203	3.348	15.41
[Pt(L2)(8-H-Quin)]	0.0156	2.658	11.85
[Pt(L2)(8-F-Quin)]	0.0175	2.886	13.29
[Pt(L2)(8-Cl-Quin)]	0.0205	3.087	15.57
[Pt(L2)(8-Br-Quin)]	0.0217	3.163	16.48
[Pt(L2)(8-I-Quin)]	0.0222	3.297	16.86

*Bond character (%) calculated as: $\left(\rho(\mathrm{M}-\mathrm{Q})\Big/\rho(\mathrm{M}-\mathrm{O})\right)\times 100.$

Tables 4.9–4.11 show that that as the M···Q distance increases, the electron density at the M···Q bond critical point increases, making the M···Q interaction stronger. This trend reflects the increased overlap volume between the interacting M and Q atoms (as discussed above). At the same time, the M—$N_{(quin)}$ bond distance is increasing and the electron density of the M—$N_{(quin)}$ bond critical point is decreasing. The structure seems to be tending towards a distorted trigonal bipyramidal 5-coordination state, where the axial ligand donors are two of the amide nitrogen atoms and the equatorial ligand donors consist of the quinoline nitrogen atom, the pyridine nitrogen atom, and atom Q (Figure 4.16).

It is, however, noteworthy that an analysis of the electron density of a bond critical point is not enough to fully characterize and understand the nature of the interaction. For this

reason, the *Laplacian of the electron density* of selected bond critical points in each of the structures was calculated. The results of this analysis have been presented in Table 4.12, and an example of the output of the AIM analysis has been shown in Figure 4.24 and Scheme 4.1.



Scheme 4.1. The output of an AIM analysis performed on the structure of $[Au(terpy)(OH)]^{2+}$, CSD code: BORSUY. Bond critical points are rendered as green spheres, with ρ data labels displayed over selected bond critical points This structure was used to provide a suitable reference electron density for a substantially more covalent M-O coordination bond, enabling estimates of the % covalent character to be made in Tables 4.9-4.11.

Table 4.12. Table showing the Laplacian of the electron density ($\nabla^2\rho$) at the bond critical point of the M···Q interaction for each of the molecules in the monoatomic compound series.

Compound	$\nabla^2\rho$(M···Q) (au)	Compound	$\nabla^2\rho$(M···Q) (au)
[Au(L1)(8-F-Quin)]$^+$	0.0659	Pd(L2)(8-F-Quin)]	0.0605
[Au(L1)(8-Cl-Quin)]$^+$	0.0655	[Pd(L2)(8-Cl-Quin)]	0.0676
[Au(L1)(8-Br-Quin)]$^+$	0.0610	[Pd(L2)(8-Br-Quin)]	0.0633
[Au(L1)(8-I-Quin)]$^+$	0.0541	[Pd(L2)(8-I-Quin)]	0.0559
[Au(L1)(8-H-Quin)]$^+$	0.0000	[Pd(L2)(8-H-Quin)]	0.0405
[Au(L2)(8-F-Quin)]$^+$	0.0862	[Pt(L1)(8-F-Quin)]	0.0551
[Au(L2)(8-Cl-Quin)]$^+$	0.0833	[Pt(L1)(8-Cl-Quin)]	0.0536
[Au(L2)(8-Br-Quin)]$^+$	0.0760	[Pt(L1)(8-Br-Quin)]	0.0562
[Au(L2)(8-I-Quin)]$^+$	0.0641	[Pt(L1)(8-I-Quin)]	0.0484
[Au(L2)(8-H-Quin)]$^+$	0.0416	[Pt(L1)(8-H-Quin)]	0.0409
[Pd(L1)(8-F-Quin)]	0.0524	[Pt(L2)(8-F-Quin)]	0.0739
[Pd(L1)(8-Cl-Quin)]	0.0592	[Pt(L2)(8-Cl-Quin)]	0.0699
[Pd(L1)(8-Br-Quin)]	0.0544	[Pt(L2)(8-Br-Quin)]	0.0648
[Pd(L1)(8-I-Quin)]	0.0467	[Pt(L2)(8-I-Quin)]	0.0528
[Pd(L1)(8-H-Quin)]	0.0377	[Pt(L2)(8-H-Quin)]	0.0545
		CDMPAU	0.1510

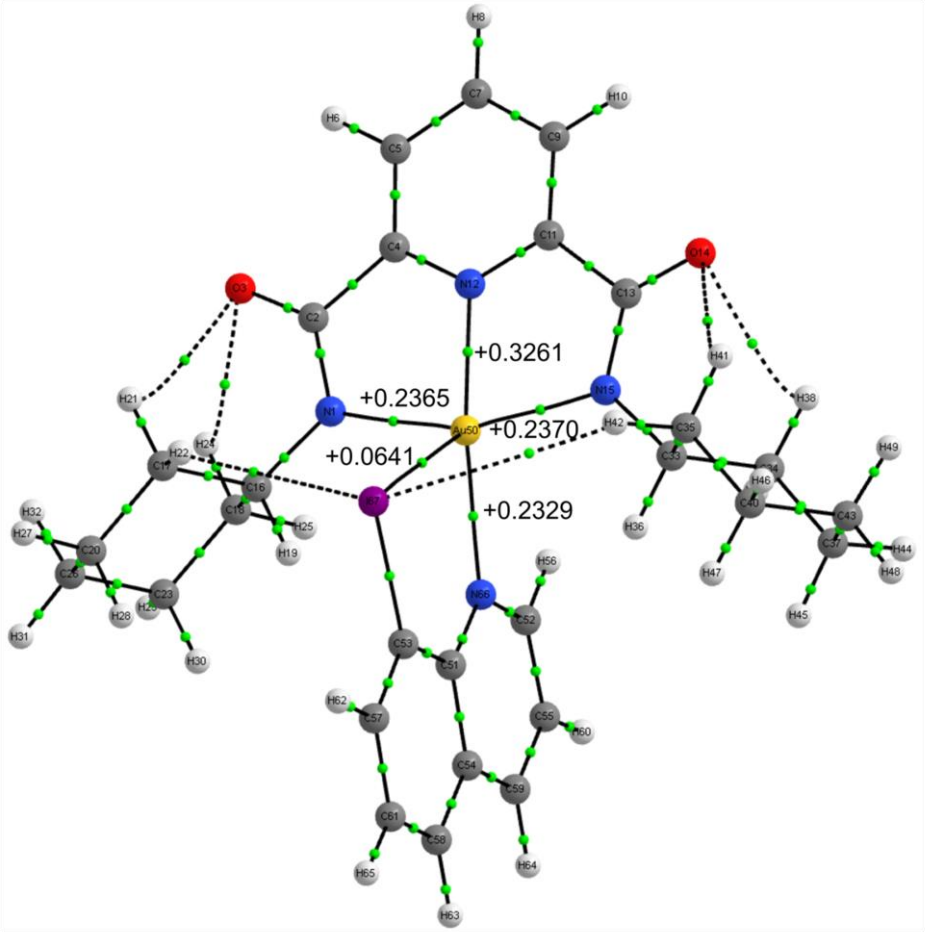


Figure 4.24. Example of the output of an AIM analysis on the $[Au(L2)(8\text{-I-Quin})]^+$ structure. Bond critical points are rendered as green spheres, with $\nabla^2\rho$ data labels displayed over selected bond critical points. All of the $\nabla^2\rho$ values are positive, showing that the bonds are ionic in nature.

For the compounds that were studied (Table 4.12), all of the M···Q interactions were ionic in nature. This is because at the bond critical points for each M···Q interaction, the Laplacian of the electron density ($\nabla^2\rho$) was greater than zero, clearly meeting the criteria for an ionic interaction.[24]

In a given M(Lx) series, the M(Lx)(8-H-Quin) compound shows a weak ionic interaction between the metal and hydrogen atoms (evidenced by the small, positive $\nabla^2\rho$ value). The ionic character of the M···Q interaction continues to increase for the M(Lx)(8-F-Quin) and M(Lx)(8-Cl-Quin) complexes. In all cases, the M(Lx)(8-Cl-Quin) structure exhibits the greatest ionic character of the M···Q interaction, with the only exception being for the Pt(L2) series, where the Pt(L2)(8-F-Quin) structure has a more positive ($\nabla^2\rho$) value for M···Q , and thus the interaction has a greater degree of ionic character. There is a noticeable decrease

in ionic character for the M···Br and M···I interactions in the M(Lx)(8-Br-Quin) and M(Lx)(8-I-Quin) structures. This shows that the interaction becomes increasingly more covalent in nature. An explanation for this could be that the Cl or F–containing structures (M(Lx)(8-F/Cl-Quin)) exhibit a maximally ionic (M···Q) interaction and the Br and I structures (M(Lx)(8-Br/I-Quin)) exhibit a more covalent interaction due to the side-on interaction that occurs between the $6p_z$ orbital of the metal ($5p_z$ in the case of Pd^{2+}) and the 4s and 4p orbitals of Br or the 5s and 5p orbitals of I. Bromine and iodine are particularly effective at transferring electron density to the empty $6p_z/5p_z$ orbital of the metal because of the diffuse nature of their orbitals, in particular their 4s and 5s orbitals. This interaction has been illustrated in Figure 4.25.

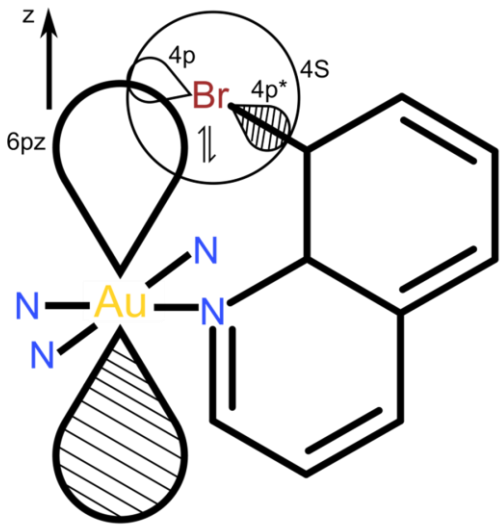


Figure 4.25. Diagram illustrating the nature of the side-on M···Br interaction in the $Au(Lx)(8\text{-}Br\text{-}Quin)]^+$ structure. Electron density is transferred from the diffuse 4s orbital of Br into the $6p_z$ orbital of Au(III).

The M···Q interactions in the series of compounds studied in Table 4.12 are significantly different to those of nominally 5-coordinate 1,10-phenanthroline derivatives (Figure 4.22). In the case of CDMPAU, a 5-coordinate Au(III) 1,10-phenanthroline compound, the M···Q interaction is very ionic ($\nabla^2\rho$ = +1.51 a.u.) because the lone pair of the upper 1,10-phenanthroline nitrogen atom is positioned so that it is orientated directly into the $6p_z$ orbital of the metal. This is the main difference between the systems, because the M···R interaction in the literature structure is purely ionic in nature, while the M···R interaction in the quinoline-based structures in this study, while still ionic, have a significant amount of covalent character. This is readily apparent for the bromine and iodine-containing structures from

Table 4.12. The key interaction relevant to the literature structure (CDMPAU) has been illustrated in Figure 4.26. In addition, a direct DFT and AIM-based comparison has been presented in Section 4.3.5.3.

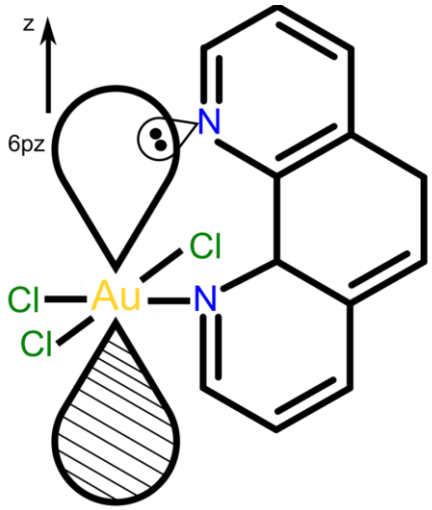


Figure 4.26. Diagram illustrating the ionic Au···N interaction that is present in the CDMPAU structure. The 1,10-phenanthroline nitrogen is positioned so that the lone pair on the nitrogen is orientated into the $6p_z$ orbital of Au(III).

4.3.5.3 Literature comparison

CDMPAU, (trichloro-(2,9-dimethyl-1,10-phenanthroline)Au(III)), a nominally 5-coordinate Au(III) structure, was analysed in the same way as all of the other structures in this study. The DFT calculations were performed at the HSEH1PBE/6-311G(d,p) level of theory. The SARC ZORA basis set was also used. The DFT calculation yielded an optimized structure with slightly different bond lengths to the crystal structure as illustrated below in Figure 4.27. The analysis of trichloro-(2,9-dimethyl-1,10-phenanthroline)Au(III) seems to confirm that *partially 5-coordinate Au(III) complexes are possible*. Based on the magnitude of the electron density at the BCP of the Au···$N_{(axial)}$ interaction (0.0371 a.u.), which is close to 50% of the value of the electron density at the BCP of the equatorial Au···$N_{(phenanthroline)}$ interaction (0.0812 a.u.), it is possible to conclude for CDMPAU that the axial donor···Au(III) interaction amounts to a partial dative covalent bond. As delineated above, we find that this unexpected phenomenon may be explained by the vacant $6p_z$ atomic orbital of Au(III) accepting significant σ-electron density from the interacting donor atom.

Table 4.13. Comparison of bond lengths of the crystal vs the DFT-calculated structure of CDMPAU. Information on the key bond critical points is also provided in the table.

Bond	ρ(Au(III)···X) (a.u.) (DFT)	Au(III)···X distance (Å) (DFT)	Au(III)···X distance (Å) (Crystal structure)
Au1—Cl3	0.0684	2.456	2.267
Au1—Cl2	0.0529	2.585	2.275
Au1—Cl4	0.0529	2.585	2.285
Au1—N20	0.0371	2.617	2.584
Au1—N19	0.0812	2.224	2.093

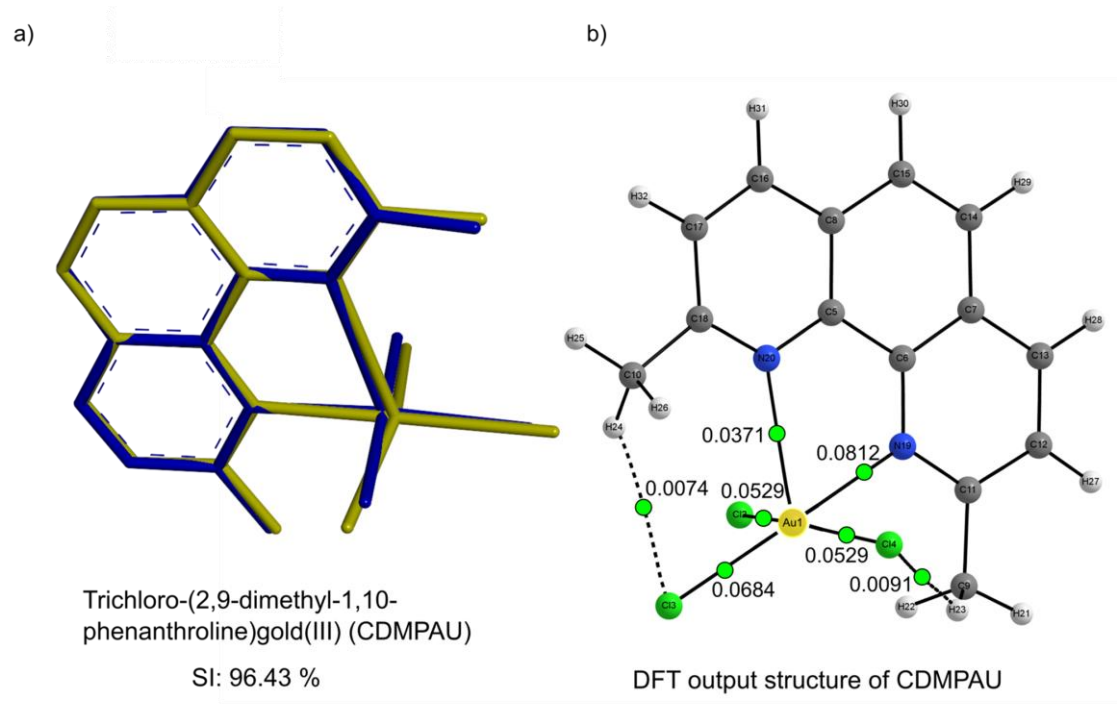


Figure 4.27. (a) Overlay of the DFT-calculated and crystal structure of CDMPAU. SI: 96.43%. Hydrogen atoms have been excluded for visibility. (b) DFT-calculated structure of CDMPAU with selected results of the AIM analysis. Selected bond critical points have been shown as green dots and their corresponding ρ values have been provided in Table 4.9.

4.4 Conclusions

In this Chapter, it was confirmed (by X-ray crystallography) that the ligands we studied in Chapter 3 were suitable chelating agents for Au(III) and Pd^{2+} metal cations. Further, the shape of the tridentate pincer ligand was suited to the uptake of a quinoline co-ligand at the fourth coordination site on the metal center, placing the quinoline ligand within the "arms" of the pincer ligand.

A CSD analysis was conducted and a number of compounds of interest were extracted for further analysis. From this information, the range of possible axially-interacting atoms was established. Crystal structures for *N,N'*-bis(2,4,6-trimethylphenyl)-2,6-pyridinecarboxamidato(quinoline)Au(III) and a *N,N'*-bis(2,4,6-trimethylphenyl)-2,6-pyridinecarboxamidato-(quinoline)palladium(II) were obtained. Both of the compounds were fully characterized and studied. Derivatives of these two structures were investigated further using state-of-the-art computational methods in order to gain insight into the nature of the binding and electrostatic interactions that occur between the metal cation and key ligand atoms in the molecule. It was established that *partially* 5-coordinate Pt^{2+}, Pd^{2+} and Au(III) structures are possible according to our DFT calculations; specific examination of related literature structures containing 1,10-phenanthroline (as opposed to quinoline) as a co-ligand appear to confirm the notion that a partial 5-coordinate state is possible, especially for Au(III).

However, it is noteworthy that this study has not established if 5-coordination is possible in structures that do not have a 1,10-phenanthroline-type ligand. Even though 5- or 6-coordinate complexes were not observed in any of the crystal structures that were obtained in this dissertation, two structures within this class of complexes have been identified through computational work as having the potential to exhibit *partial* 5-coordination, specifically $[Au(L2)(8\text{-Br-Quin})]^+$ and $[Au(L2)(8\text{-I-Quin})]^+$. Going forward, synthesizing and characterizing $[Au(L2)(8\text{-Br-Quin})]^+$ and $[Au(L2)(8\text{-I-Quin})]^+$ would be vital for any future studies on this topic, particularly as a way of addressing this fundamental question.

The most energetically-favoured conformers of Au(Lx)Quin system were investigated and reported upon. 2D conformational analysis was used to probe the differences between the Au(L1) and Au(L2) complexes. It was discovered that the nature of the aliphatic or aromatic rings in ligands L1 and L2, had a significant impact on the conformation of the complex and strength of the M···Q interaction. This was due to π-bonding (that was exclusively observed in complexes of L1) which occurred between the aromatic ring and the quinoline substituent.

Computational analysis of the structural and electronic parameters of a series of Au(III), Pd(II) and Pt(II) complexes was performed. Strong linear trends were found between the

following pairs of structural parameters: (a) 6s orbital occupancy vs M···Q distance, (b) β vs ρM···Q, and (c) ρM···Q vs $6p_z$ orbital occupancy. A theoretically-derived parameter, β, correlated to the DFT-calculated degree of orbital overlap. These computational results suggest that 5-coordinate Au(III) structures are possible, specifically in the ([Au(L2)(8-Br-Quin)]$^+$ and [Au(L2)(8-I-Quin)]$^+$ structures. The computational results also suggest that the ionic axial bond in the 5 coordinate species forms because of how electron density is forced from the p and S orbitals of the interacting atom (Q), into the $6p_z$ orbital of Au(III). This interaction (bond) was shown to be ionic in nature, with increasing covalent character as the orbital size of Q increases past a certain threshold. The structural and electronic properties of certain theoretical structures were compared and contrasted to specific 5-coordinate Au, Pt and Pd 1,10-phenanthroline-containing structures found in the literature. It was concluded that the 1,10-phenanthroline-containing structures are not directly comparable to the theoretical series of complexes that were the central focus of this dissertation (Table 4.5). This is because the mode of binding in the 1,10-phenanthroline-containing structures occurs through a nitrogen lone pair in the ligand. The M···Q interactions in the 1,10-phenanthroline-containing compound seem to be purely ionic in nature, in contrast to those from quinoline as the co-ligand, according to the Laplacian of the electron density of the bond critical points.

4.6 Notes and References

11. K. J. Akerman, A. M. Fagenson, V. Cyril, M. Taylor, M. T. Muller, M. P. Akerman and O. Q. Munro, Journal of the American Chemical Society, 2014, 136, 5670-5682.

12. M. W. Johnson, A. G. DiPasquale, R. G. Bergman and F. D. Toste, Organometallics, 2014, 33, 4169-4172.

24. F. Jensen, Introduction to computational chemistry, John Wiley & Sons, 2017.

31. P. Fuentealba, H. Preuss, H. Stoll and L. Von Szentpály, Chemical Physics Letters, 1982, 89, 418-422.

35. N. Godbout, D. R. Salahub, J. Andzelm and E. Wimmer, Canadian Journal of Chemistry, 1992, 70, 560-571.

42. F. Jensen, West Sussex, England: John Wiley & Sons Ltd, 30-34.

53. M. Gao, Q. Li, H.-B. Li, W. Li and J. Cheng, RSC Advances, 2015, 5, 12488-12497.

62. AIMAll (Version 17.11.14), Todd A. Keith, TK Gristmill Software, Overland Park KS, USA, 2017 (aim.tkgristmill.com)

63. E. D. Glendening, A. E. Reed, J. E. Carpenter, F. Weinhold. NBO Version 3.1

68. Q.-Q. Wang, R. A. Begum, V. W. Day and K. Bowman-James, Journal of the American Chemical Society, 2013, 135, 17193-17199.

100. M. J. Frisch, G. W. Trucks, H. B. Schlegel, G. E. Scuseria, M. A. Robb, J. R. Cheeseman, G. Scalmani, V. Barone, B. Mennucci, G. A. Petersson, H. Nakatsuji, M. Caricato, X. Li, H. P. Hratchian, A. F. Izmaylov, J. Bloino, G. Zheng, J. L. Sonnenberg, M. Hada, M. Ehara, K. Toyota, R. Fukuda, J. Hasegawa, M. Ishida, T. Nakajima, Y. Honda, O. Kitao, H. Nakai, T. Vreven, J. A. Montgomery, Jr., J. E. Peralta, F. Ogliaro, M. Bearpark, J. J. Heyd, E. Brothers, K. N. Kudin, V. N. Staroverov, R. Kobayashi, J. Normand, K. Raghavachari, A. Rendell, J. C. Burant, S. S. Iyengar, J. Tomasi, M. Cossi, N. Rega, J. M. Millam, M. Klene, J. E. Knox, J. B. Cross, V. Bakken, C. Adamo, J. Jaramillo, R. Gomperts, R. E. Stratmann, O. Yazyev, A. J. Austin, R. Cammi, C. Pomelli, J. W. Ochterski, R. L. Martin, K. Morokuma, V. G. Zakrzewski, G. A. Voth, P. Salvador, J. J. Dannenberg, S. Dapprich, A. D. Daniels, Ö. Farkas, J. B. Foresman, J. V. Ortiz, J. Cioslowski, and D. J. Fox, Gaussian 09 (Gaussian, Inc., Wallingford CT, 2009).

106. P. R. Rablen, S. A. Pearlman and D. A. Miller, Journal of the American Chemical Society, 1999, 121, 227-237.

112. Munro, O. Q., Akerman, K. J., & Akerman, P. U.S. Patent No. 9,346,832. Washington, DC: U.S. Patent and Trademark Office. 2016.

113. R. Elder and J. Watkins, Inorganic Chemistry, 1986, 25, 223-226.

114. K. Suntharalingam, D. Gupta, S. Miguel, J. Pablo, B. Lippert and R. Vilar, Chemistry-A European Journal, 2010, 16, 3613-3616.

115. M. P. Suh, I. S. Kim, B. Y. Shim, D. Hong and T.-S. Yoon, Inorganic Chemistry, 1996, 35, 3595-3598.

116. S. M. Godfrey, N. Ho, C. A. McAuliffe and R. G. Pritchard, Angewandte Chemie International Edition, 1996, 35, 2344-2346.

117. R. Corbo, T. P. Pell, B. D. Stringer, C. F. Hogan, D. J. Wilson, P. J. Barnard and J. L. Dutton, Journal of the American Chemical Society, 2014, 136, 12415-12421.

118. E. Makotchenko, E. Bykova, E. Y. Semitut, Y. V. Shubin, P. Snytnikov and P. Plyusnin, Journal of Structural Chemistry, 2011, 52, 924-929.

119. E. Rabinovich, I. Goldberg and Z. Gross, Chemistry-A European Journal, 2011, 17, 12294-12301.

120. S. O. Sommerer, C. E. MacBeth, A. J. Jircitano and K. A. Abboud, Acta Crystallographica Section C: Crystal Structure Communications, 1997, 53, 1551-1553.

121. E. W. Wong, A. Miura, M. D. Wright, Q. He, C. J. Walsby, S. Shimizu, N. Kobayashi and D. B. Leznoff, Chemistry-A European Journal, 2012, 18, 12404-12410.

122. T. Roth, H. Wadepohl and L. H. Gade, European Journal of Inorganic Chemistry, 2016, 2016, 1184-1191.

123. W. T. Robinson and E. Sinn, Journal of the Chemical Society, Dalton Transactions, 1975, 726-731.

124. C. J. O'Connor and E. Sinn, Inorganic Chemistry, 1978, 17, 2067-2071.

125. S. Karmakar, S. Chatterjee, K. Purkait and A. Mukherjee, Dalton Transactions, 2016, 45, 11710-11722.

126. K. V. Luzyanin, M. Haukka, Y. A. Izotova, V. Y. Kukushkin and A. Pombeiro, Acta Crystallographica Section E: Structure Reports Online, 2005, 61, m1765-m1767.

127. L. R. Gray, D. J. Gulliver, W. Levason and M. Webster, Journal of the Chemical Society, Dalton Transactions, 1983, 133-141.

128. R. Corbo, G. F. Ryan, M. A. Haghighatbin, C. F. Hogan, D. J. Wilson, M. D. Hulett, P. J. Barnard and J. L. Dutton, Inorganic chemistry, 2016, 55, 2830-2839.

129. R. Dennington, T. Keith and J. Millam, Semichem Inc., Shawnee Mission, KS, 2009.

130. M. Frisch, G. Trucks, H. B. Schlegel, G. Scuseria, M. Robb, J. Cheeseman, G. Scalmani, V. Barone, B. Mennucci and G. Petersson, Journal, 2009.

131. D. A. Pantazis, X.-Y. Chen, C. R. Landis and F. Neese, Journal of Chemical Theory and Computation, 2008, 4, 908-919.

132. M. J. Frisch, J. A. Pople and J. S. Binkley, The Journal of Chemical Physics, 1984, 80, 3265-3269.

133. T. A. Keith, TK Gristmill Software, Overland Park KS, USA, 2013.

134. A. Reed and F. Weinhold, Chem. Phys, 1983, 78, 4066-4073.

135. M. O. Sinnokrot, E. F. Valeev and C. D. Sherrill, Journal of the American Chemical Society, 2002, 124, 10887-10893.

136. Weisstein, Eric W. "Making MathWorld." The Mathematica Journal 10, 474-488, 2007

137. A. Bondi, The Journal of physical chemistry, 1964, 68, 441-451.

138. S. Batsanov, Zh. Fiz. Khim, 2000, 74, 1273-1276.

139. T. L. Brown, Chemistry: the central science, Pearson Education, 2009.

140. R. G. Parr and R. G. Pearson, Journal of the American Chemical Society, 1983, 105, 7512-7516.

141. S. Batsanov, Inorganic Materials, 2001, 37, 871-885.

142. R. G. Pearson, Proceedings of the National Academy of Sciences, 1986, 83, 8440-8441.

143. G. Marangoni, B. Pitteri, V. Bertolasi, G. Gilli and V. Ferretti, Journal of the Chemical Society, Dalton Transactions, 1986, 1941-1944.

144. J. Vicente, M. T. Chicote, M. D. Bermúdez, P. G. Jones, C. Fittschen and G. M. Sheldrick, Journal of the Chemical Society, Dalton Transactions, 1986, 2361-2366.

145. C.-W. Chan, W.-T. Wong and C.-M. Che, Inorganic Chemistry, 1994, 33, 1266-1272.

146. Z. D. Hudson, C. D. Sanghvi, M. A. Rhine, J. J. Ng, S. D. Bunge, K. I. Hardcastle, M. R. Saadein, C. E. MacBeth and J. F. Eichler, Dalton Transactions, 2009, 7473-7480.

147. S. Chatterjee, J. A. Krause, K. Madduma-Liyanage and W. B. Connick, Inorganic chemistry, 2012, 51, 4572-4587.

148. E. W. Ainscough, A. M. Brodie, A. K. Burrell, A. Derwahl, G. B. Jameson and S. K. Taylor, Polyhedron, 2004, 23, 1159-1168.

149. L. Maresca and G. Natile, Comments on Inorganic Chemistry, 1993, 14, 349-366.

150. F. P. Fanizzi, L. Maresca, C. Pacifico, G. Natile, M. Lanfranchi and A. Tiripicchio, European Journal of Inorganic Chemistry, 1999, 1999, 1351-1358.

151. M. Rimoldi, F. Ragaini, E. Gallo, F. Ferretti, P. Macchi and N. Casati, Dalton Transactions, 2012, 41, 3648-3658.

152. R. Garrone, A. M. Romano, R. Santi and R. Millini, Organometallics, 1998, 17, 4519-4522.

153. S. Pratihar, J. Marek and S. Roy, Inorganica Chimica Acta, 2011, 372, 362-366.

154. I. D. Hills and G. C. Fu, Journal of the American Chemical Society, 2004, 126, 13178-13179.

155. A. Seyboldt, B. Wucher, S. Hohnstein, K. Eichele, F. Rominger, K. W. Törnroos and D. Kunz, Organometallics, 2015, 34, 2717-2725.

CHAPTER 5

Conclusions and Future Work

5.1 Summary and Conclusions

Four compounds were synthesized for this dissertation, three of which are novel compounds. Two of the compounds synthesized were ligands, and two were metal chelates of one of the ligands (Figure 5.1). The ligands in question contained a pyridine-2,6-dicarboxamide backbone and were prepared by reacting 1 mole equivalent of pyridine-2,6-dicarbonyl dichloride with 2 mole equivalents of 2,4,6-trimethylaniline or cyclohexanamine to yield the desired bis(amides) H_2L1 and H_2L2, respectively. It was shown that the synthetic design proposed in **Chapter 1** was suitable and good yields of high purity product were obtained. In order for metal complexation to occur, amide N-H protons were deprotonated, resulting in an anionic ligand that was capable of metal binding. The ligands were fully characterized and studied with the intention of evaluating their potential for binding to various metal cations. The reaction of doubly-deprotonated H_2L1 with $[AuCl_4]^-$ in the presence of quinoline afforded a Au(III) chelate of the pincer ligand with quinoline as a co-ligand and an overall +1 charge. The cation was isolated as a PF_6^- salt: [Au(L1)(Quinoline)][PF_6]. The same reaction with anhydrous $PdCl_2$ afforded the palladium(II) chelate with an overall neutral charge: Pd(L1)(Quinoline). Figure 5.1 below shows all of the compounds that were synthesized for this dissertation.

Through use of single X-ray diffraction, the solid-state structures of all suitably crystalline compounds (free ligands and metal chelates) were determined. The Au(III) ion of Au(L1)(Quinoline)][PF_6] exhibited the expected square planar coordination geometry due to the d^8 electron configuration of the metal. Pd(L1)(Quinoline) exhibited similar structural features to that of the Au(III) ion, despite the significantly larger ionic radius of Pd(II). This was an expected result because both structures are isoelectronic and their coordination chemistry is largely governed by the geometrical constraints of the pincer ligand. In the case of the crystal structures of the free ligands, it was found that H_2L2 exhibited strong intermolecular hydrogen bonding, and consequently formed a one-dimensional chain of H-bonded dimers both in the solid state and in solution (as detected by ^{1}H NMR spectroscopy). In the X-ray structure of H_2L1, which lacked intermolecular H-bonding, the two C=O bond lengths were 1.223 and

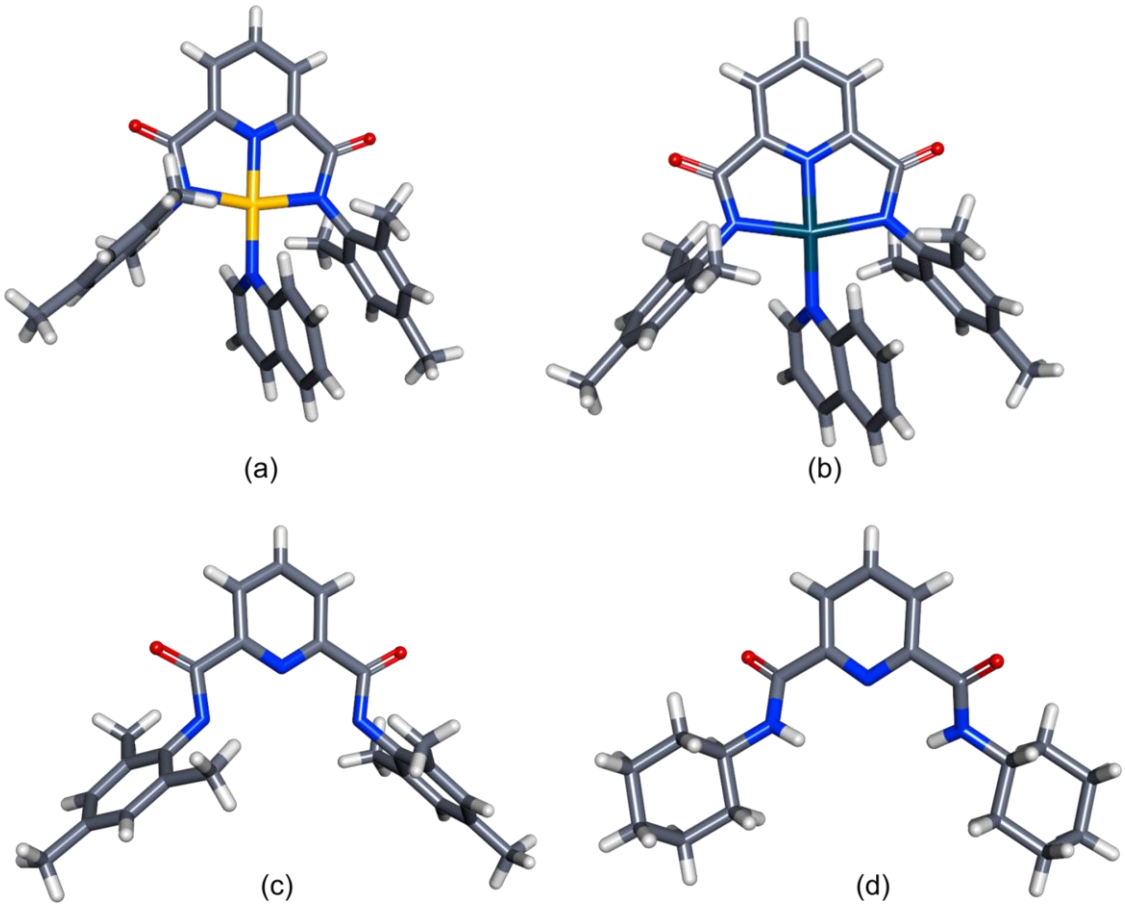


Figure 5.1. Diagram showing the compounds that have been synthesised during this dissertation. (a) *N,N'*-bis(2,4,6-trimethylphenyl)-2,6-pyridinecarboxamidato(quinoline)Au(III), (b) *N,N'*-bis(2,4,6-trimethylphenyl)-2,6-pyridinecarboxamidato(quinoline)palladium(II), (c) *N*,*N*'-Bis(2,4,6-trimethylphenyl)-2,6-pyridinedicarboxamide (H_2L1) and (d) *N*,*N*'-Bis(cyclohexyl)-2,6-pyridinedicarboxamide (H_2L2).

1.220 Å; the C—$N_{(amide)}$ bond lengths were 1.341 and 1.343 Å. The bond lengths of H_2L2 were similar: C=O, 1.241 and 1.237 Å; C–$N_{(amide)}$, 1.337 and 1.322 Å. All four crystal structures are novel.

All of the compounds that were reported on in this study, were studied using spectroscopic methods, which included ^{1}H NMR, ^{13}C NMR, FTIR, UV-visible spectroscopy and high resolution mass spectroscopy.

Analysis of pincer compounds based on the pyridine bis(amide) framework relevant to this study in the Cambridge Crystallographic Database (CSD) revealed that many ligands and complexes

structurally similar to those based on H_2L1 and H_2L2 exist. The analysis found that the overwhelmingly favoured conformation has an *endo*|*endo* orientation/rotation for the pair of amide N–H groups, such that this class of pincer ligands may be considered to be pre-organized for metal ion chelation.

DFT simulations were performed in order to predict structural features, conformational energy profiles and molecular orbital configurations of selected compounds. This was ultimately done so that the theoretical data could be compared with empirically derived data (^{1}H NMR, FTIR and crystal structure data). It was found that the DFT-calculated structures and conformations of the free ligands matched the experimentally derived data. In particular, the simulations clearly suggest that although the system is conformationally flexible (several low barriers to dihedral angle rotation), there is a strong thermodynamic preference of at least 30 kJ mol^{-1} for *endo*|*endo* over *endo*|*exo* or *exo*|*exo* conformations, the latter being particularly unfavorable for the free ligands (ΔE > 100 kJ mol^{-1}).

The one-dimensional H-bonded chain that was observed for H_2L2 was a key area that was explored in this dissertation. The presence of NH···O dimerization and higher oligomerization in the solid state was confirmed through crystal structure data, while dimerization (early-onset oligomerization) in the liquid state was confirmed through a variable-concentration ^{1}H NMR study. The hydrogen bonding chains cause the C_2 symmetry of H_2L2 to be overridden by the symmetry of the supramolecular one-dimensional chain. According to the calculated ΔG, the chain self-assembly was spontaneous. This dimerization was not predicted by the DFT calculations because packing effects are not taken into account for the simulations that are performed *in vacuo*. The crystal structures of H_2L1 and H_2L2 are in good agreement with the DFT calculated structures.

The main structural differences between ligands H_2L1 and H_2L2 are due to the presence of aliphatic ring groups in H_2L2 and aromatic rings in H_2L1. Based on molecular orbital simulations (specifically HOMO–LUMO gap data), it was determined that ligand H_2L2 is harder than ligand H_2L1, and will thus preferentially bind to harder metal cations. The 3-D potential energy surfaces for ligands H_2L1 and H_2L2 were calculated. This conformational data was then linked to the results of a dynamic ^{1}H NMR study, which showed that at 213.15 K only one N–H conformer of H_2L2 was populated (global minimum with *endo*|*endo* N–H groups) and that at 243.15 K and higher temperatures *endo*|*endo*, *endo*|*exo* and *exo*|*exo* conformations are all populated.

2D conformer profiles of certain Au(III) complexes were calculated and used to establish how the two deprotonated pincer ligands H_2L1 and H_2L2 affect the structural stability and the relative positioning of atoms in the metal chelates. It was found that π-stacking interactions occur for metal complexes of L1 and the strengths of the interactions are consistent with experimentally derived values from the literature.[135]

A correlation table was produced from theoretically derived DFT and AIM data. The data were used to establish a trend between the structures as the quinoline substituent (and thus Q group) was varied. The data were used to select the two potential candidates that could exhibit 5-coordinate binding to specific metal cations (*N,N′*-bis(2,4,6-trimethylphenyl)-2,6-pyridinecarboxamidato(8-bromo-quinoline)Au(III) and *N,N′*-bis(2,4,6-trimethylphenyl)-2,6-pyridinecarboxamidato(8-iodo-quinoline)Au(III)). The DFT and AIM computational methods were also used to validate previously reported 1,10-phenanthroline-containing structures where apparent 5-coordination was observed.[143, 145, 146] It was concluded that the 1,10-phenanthroline-containing structures are not directly comparable to the theoretical complexes that were studied (Chapter 4). This is because the mode of binding in the 1,10-phenanthroline-containing structures occurs through a nitrogen lone pair in the ligand.

Computational analysis of the structural and electronic parameters of a series of Au(III), Pd(II) and Pt(II) complexes was performed. In the experiments on our pincer ligands coordinated to the target metal ion, wherein a quinoline co-ligand was bound orthogonal to the plane of the pincer chelate (as in the X-ray structures), the substituent atom (Q) at position 8 on the quinoline ring is positioned in space above the metal ion (M) residing in the plane of the pincer chelate. This design allowed us to directly test the effect of varying the identity of Q (H, F, Cl, Br, I) on the M···R interaction.

Strong linear trends were found between the following pairs of structural parameters: 6s orbital occupancy vs M···Q distance, β vs ρ(M···Q), and ρ(M···Q) vs $6p_z$ orbital occupancy, where β is the atom-atom overlap volume and ρ the electron density at the bond critical point (BCP). The trigonometrically-derived parameter β (which is based on atom van der Waals radii) was strongly correlated to the DFT-calculated degree of orbital overlap, as gauged by the electron density at the M···Q BCP. The computational results also suggested that the mainly ionic axial interaction in the *partially* 5-coordinate species forms because of how electron density is forced from the p- and s-orbitals of the interacting atom (Q) into the vacant $6p_z$ orbital of Au(III). This

interaction was shown to be ionic in nature for Q = H, with increasing covalent character as the orbital size of Q increases past a certain threshold (Q = Br, I).

5.2 Future work and unanswered questions

It would be useful to test the complex *N,N'*-bis(2,4,6-trimethylphenyl)-2,6-pyridine-carboxamidato(quinoline)Au(III) for anti-cancer and anti-bacterial activity. The complex was not designed with a specific medicinal application in mind *a priori*, but given the manner in which quinoline binds to Au(III), as elucidated in this work, it is possible that the Au(III) pincer compound could bind to DNA bases such as adenine and guanine in a similar fashion. Such compounds could exhibit useful medicinal properties or at least contribute to what is known about this particular series of compounds. The key strategy going forward would be to use water-soluble aromatic amines to form water-soluble pincer chelates of Au(III) to enable the study of their DNA binding and cytotoxicity in biological media.

It is of vital importance that ^{13}C DNMR data is obtained for **2**, so that the conclusions made using the ^{1}H DNMR data can be fully supported by experimental evidence. Such an analysis was not performed due to the limited capabilities of the NMR unit at the University of the Witwatersrand.

Another area of interest would be to synthesize and characterize the computationally-investigated structures that could potentially exhibit true 5-coordinate Au(III): (*N,N'*-bis(2,4,6-trimethylphenyl)-2,6-pyridinecarboxamidato(8-bromo-quinoline)Au(III) and *N,N'*-bis(2,4,6-trimethylphenyl)-2,6-pyridinecarboxamidato(8-iodo-quinoline)Au(III)). This would be a vital experimental test of the *in silico* (DFT) work reported in this dissertation and will confirm if 5-cooridination is indeed possible in these structures. Ultimately, experimental data for the envisaged complexes will serve to further validate the results that were obtained by AIM and DFT methods.

Another area for future work would be to establish the thermodynamic metal-binding characteristics of ligands based on H_2L1 and H_2L2. This study could be performed on metal cations that are theoretically suited to binding the chelating agents H_2L1 and H_2L2 (based on the relative and absolute hardness/softness of the ligands and metal cations). Because current binding predications are based on HSAB theory, adding some experimentally derived data would be useful for validating our DFT-calculated predictions. This information could also be used to probe the fundamentals of HSAB theory in relation to metal–ligand binding. Since most

thermodynamic metal-binding studies are conducted in water by potentiometry, the use of water-soluble derivatives of H_2L1 and H_2L2 would be recommended. However given that complexed forms of ligand **1** (the ligand predicted to bind less favourably to Au(III)) were obtained, it is unclear how applicable and accurate the predictions are. More experimental evidence is needed to fully support these claims.

One-dimensional hydrogen bonding in H_2L2 was observed in only two NMR solvents (DMSO-d_6 for high temperature, and $CDCl_3$ for low temperature). This was mainly due to time constraints, which limited a thorough analysis using a variety of solvents. Further research on this topic is important because certain solvents have been known to affect the nature of one-dimensional chain assembly, and may compete for H-bonding sites.[106] Finally, it would be of interest to perform additional 3D conformational analysis simulations because a number of dihedral angle scans were not performed given the limited time and current computational resources available to us. Scans of interest include:

- Performing the same dihedral angle scan that was performed on the ligand H_2L2 (Chapter 3, Figure 3.15), but with H_2L1. This study was not conducted because of limited resources and the fact that we wanted the full set of PES maps for H_2L2 to delineate the experimental available dynamic ^{1}H NMR data for the system.
- Perform a dihedral scan of the HN—CH torsion for H_2L2 so that the DFT-derived data can be compared to the DNMR data though use of the Karplus equation.[156]
- A reverse rotamer scan should be performed to check for partial dependence on the scan direction of the 2D conformational analysis of $[Au(L1)(8\text{-H-Quin})]^+$ (Chapter 4, Figure 4.11). We suspect that the true symmetry axis is at d = 180°, but that the maximum is offset by 24° due to an inherent deficiency in the nonlinear minimization algorithm near the maximum, which fails to locate the correct turning point as a result of insufficient strain dissipation in the forward scan direction.
- There is possibly also a 7° offset in the energy profile of the rotamer analysis of $[Au(Phen)(8\text{-H-Quin})]^+$ (Chapter 4, Figure 4.11). Again, a reverse scan should be performed and the data points averaged to get the trajectory-independent conformational energy profile.

5.3 References and notes

135. M. O. Sinnokrot, E. F. Valeev and C. D. Sherrill, *Journal of the American Chemical Society*, 2002, **124**, 10887-10893.

143. G. Marangoni, B. Pitteri, V. Bertolasi, G. Gilli and V. Ferretti, *Journal of the Chemical Society, Dalton Transactions*, 1986, 1941-1944.

145. C.-W. Chan, W.-T. Wong and C.-M. Che, *Inorganic Chemistry*, 1994, **33**, 1266-1272.

146. Z. D. Hudson, C. D. Sanghvi, M. A. Rhine, J. J. Ng, S. D. Bunge, K. I. Hardcastle, M. R. Saadein, C. E. MacBeth and J. F. Eichler, *Dalton Transactions*, 2009, 7473-7480.

106. P. R. Rablen, S. A. Pearlman and D. A. Miller, *Journal of the American Chemical Society*, 1999, **121**, 227-237.

156. C. Haasnoot, F. A. de Leeuw and C. Altona, *Tetrahedron*, 1980, **36**, 2783-2792.

CHAPTER 6

Compiled Reference List

1. M. Georgy, V. Boucard, O. Debleds, C. Dal Zotto and J.-M. Campagne, *Tetrahedron*, 2009, **65**, 1758-1766.
2. A. Hoffmann-Röder and N. Krause, *Organic letters*, 2001, **3**, 2537-2538.
3. A. S. K. Hashmi, L. Schwarz, J. H. Choi and T. M. Frost, *Angewandte Chemie International Edition*, 2000, **39**, 2285-2288.
4. K. M.-C. Wong, L.-L. Hung, W. H. Lam, N. Zhu and V. W.-W. Yam, *Journal of the American Chemical Society*, 2007, **129**, 4350-4365.
5. M. C. Tang, D. P. K. Tsang, M. M. Y. Chan, K. M. C. Wong and V. W. W. Yam, *Angewandte Chemie*, 2013, **125**, 464-467.
6. S. L. Lai, L. Wang, C. Yang, M. Y. Chan, X. Guan, C. C. Kwok and C. M. Che, *Advanced Functional Materials*, 2014, **24**, 4655-4665.
7. C. M. Lemon, D. C. Powers, P. J. Brothers and D. G. Nocera, *Inorganic chemistry*, 2017, **56**, 10991-10997.
8. L. H. Einhorn, *Journal of clinical oncology*, 1990, **8**, 1777-1781.
9. R. D. Teo, H. B. Gray, P. Lim, J. Termini, E. Domeshek and Z. Gross, *Chemical Communications*, 2014, **50**, 13789-13792.
10. C. T. Lum, R. W.-Y. Sun, T. Zou and C.-M. Che, *Chemical Science*, 2014, **5**, 1579-1584.
11. K. J. Akerman, A. M. Fagenson, V. Cyril, M. Taylor, M. T. Muller, M. P. Akerman and O. Q. Munro, *Journal of the American Chemical Society*, 2014, **136**, 5670-5682.
12. M. W. Johnson, A. G. DiPasquale, R. G. Bergman and F. D. Toste, *Organometallics*, 2014, **33**, 4169-4172.
13. M. P. Akerman, O. Q. Munro, M. Mongane, J. A. Staden, W. I. Rae, C. J. Bester, B. Marjanovic-Painter, Z. Szucs and J. R. Zeevaart, *Journal of Labelled Compounds and Radiopharmaceuticals*, 2013, **56**, 530-535.
14. L. Messori, G. Marcon, A. Innocenti, E. Gallori, M. Franchi and P. Orioli, *Bioinorganic chemistry and applications*, 2005, **3**, 239-253.
15. T. Zou, C. T. Lum, C.-N. Lok, J.-J. Zhang and C.-M. Che, *Chemical Society Reviews*, 2015, **44**, 8786-8801.
16. C. K. Mirabelli, R. K. Johnson, C. M. Sung, L. Faucette, K. Muirhead and S. T. Crooke, *Cancer research*, 1985, **45**, 32-39.
17. L. Messori, F. Abbate, G. Marcon, P. Orioli, M. Fontani, E. Mini, T. Mazzei, S. Carotti, T. O'Connell and P. Zanello, *Journal of Medicinal Chemistry*, 2000, **43**, 3541-3548.
18. C. F. Shaw, *Chemical reviews*, 1999, **99**, 2589-2600.
19. K. Tepperman, Y. Zhang, P. W. Roy, R. Floyd, Z. Zhao, J. G. Dorsey and R. Elder, *Metal-based drugs*, 1994, **1**, 433-443.
20. G. S. Firestein, W. N. Kelley and R. C. Budd, *Kelley's textbook of rheumatology*, Elsevier Health Sciences, 2012.
21. R. W.-Y. Sun and C.-M. Che, *Coordination Chemistry Reviews*, 2009, **253**, 1682-1691.
22. C. R. Wilson, A. M. Fagenson, W. Ruangpradit, M. T. Muller and O. Q. Munro, *Inorganic chemistry*, 2013, **52**, 7889-7906.
23. C. Gabbiani, A. Casini, L. Messori, A. Guerri, M. A. Cinellu, G. Minghetti, M. Corsini, C. Rosani, P. Zanello and M. Arca, *Inorganic chemistry*, 2008, **47**, 2368-2379.
24. F. Jensen, *Introduction to computational chemistry*, John Wiley & Sons, 2017.
25. J. C. Cuevas and E. Scheer, *Molecular electronics: an introduction to theory and experiment*, World Scientific, 2010.
26. J. C. Slater, *Physical Review*, 1951, **81**, 385.

27. P. Hohenberg and W. Kohn, *Physical review*, 1964, **136**, B864.
28. W. Kohn and L. J. Sham, *Physical review*, 1965, **140**, A1133.
29. N. M. A. Web, "The Nobel Prize in Chemistry 1998" Nobelprize.org. , http://www.nobelprize.org/nobel_prizes/chemistry/laureates/1998/).
30. F. Jensen, *Wiley Interdisciplinary Reviews: Computational Molecular Science*, 2013, **3**, 273-295.
31. P. Fuentealba, H. Preuss, H. Stoll and L. Von Szentpály, *Chemical Physics Letters*, 1982, **89**, 418-422.
32. T. H. Dunning Jr. and P. J. Hay, in Modern Theoretical Chemistry, Ed. H. F. Schaefer III, Vol. 3 (Plenum, New York, 1977) 1-28.
33. A. McLean and G. Chandler, *The Journal of Chemical Physics*, 1980, **72**, 5639-5648.
34. R. Krishnan, J. S. Binkley, R. Seeger and J. A. Pople, *The Journal of Chemical Physics*, 1980, **72**, 650-654.
35. N. Godbout, D. R. Salahub, J. Andzelm and E. Wimmer, *Canadian Journal of Chemistry*, 1992, **70**, 560-571.
36. C. Sosa, J. Andzelm, B. C. Elkin, E. Wimmer, K. D. Dobbs and D. A. Dixon, *The Journal of Physical Chemistry*, 1992, **96**, 6630-6636.
37. J. Heyd, G. E. Scuseria and M. Ernzerhof, *The Journal of chemical physics*, 2003, **118**, 8207-8215.
38. J. Heyd and G. E. Scuseria, *The Journal of chemical physics*, 2004, **121**, 1187-1192.
39. J. Heyd and G. E. Scuseria, *The Journal of chemical physics*, 2004, **120**, 7274-7280.
40. J. Heyd, J. E. Peralta, G. E. Scuseria and R. L. Martin, *The Journal of chemical physics*, 2005, **123**, 174101.
41. R. F. Bader, *Atoms in molecules*, Wiley Online Library, 1990.
42. F. Jensen, *West Sussex, England: John Wiley & Sons Ltd*, 30-34.
43. J. Poater, M. Duran, M. Sola and B. Silvi, *Chemical reviews*, 2005, **105**, 3911-3947.
44. J. Poater, M. Solà and F. M. Bickelhaupt, *Chemistry-A European Journal*, 2006, **12**, 2889-2895.
45. C. F. Matta, J. Hernández-Trujillo, T. H. Tang and R. F. Bader, *Chemistry-A European Journal*, 2003, **9**, 1940-1951.
46. U. Koch and P. L. Popelier, *The Journal of Physical Chemistry*, 1995, **99**, 9747-9754.
47. S. Grabowski, *Journal of Molecular Structure*, 2001, **562**, 137-143.
48. C. J. Smallwood and M. A. McAllister, *Journal of the American Chemical Society*, 1997, **119**, 11277-11281.
49. S. J. Grabowski, *Tetrahedron*, 1998, **54**, 10153-10160.
50. S. Grabowski, *Journal of Molecular Structure*, 2000, **552**, 153-157.
51. D. Quiñonero, C. Garau, C. Rotger, A. Frontera, P. Ballester, A. Costa and P. M. Deyà, *Angewandte Chemie*, 2002, **114**, 3539-3542.
52. L. Koskinen, S. Jääskeläinen, E. Kalenius, P. Hirva and M. Haukka, *Crystal Growth & Design*, 2014, **14**, 1989-1997.
53. M. Gao, Q. Li, H.-B. Li, W. Li and J. Cheng, *RSC Advances*, 2015, **5**, 12488-12497.
54. W. Nakanishi, S. Hayashi and K. Narahara, *The Journal of Physical Chemistry A*, 2008, **112**, 13593-13599.
55. A. N. Chernyshev, M. V. Chernysheva, P. Hirva, V. Y. Kukushkin and M. Haukka, *Dalton Transactions*, 2015, **44**, 14523-14531.
56. S. Jääskeläinen, L. Koskinen, M. Kultamaa, M. Haukka and P. Hirva, *Solid State Sciences*, 2017, **67**, 37-45.
57. A. Shimada, T. Yaita, H. Narita, S. Tachimori and K. Okuno, *Solvent extraction and ion exchange*, 2004, **22**, 147-161.
58. O. V. Dolomanov, L. J. Bourhis, R. J. Gildea, J. A. Howard and H. Puschmann, *Journal of Applied Crystallography*, 2009, **42**, 339-341.
59. G. M. Sheldrick, *Acta Crystallographica Section C: Structural Chemistry*, 2015, **71**, 3-8.
60. M. Bruker AXS Inc., Wisconsin, USA, 2012.
61. Mestrelab Research, 2014.

62. T. A. K. AIMAll (Version 17.11.14), TK Gristmill Software, Overland Park KS, USA, 2017 (aim.tkgristmill.com).
63. A. E. R. E. D. Glendening, J. E. Carpenter, F. Weinhold. NBO Version 3.1.
64. F. Czerny, P. Döhlert, M. Weidauer, E. Irran and S. Enthaler, *Inorganica Chimica Acta*, 2015, **425**, 118-123.
65. J.-C. Wasilke, G. Wu, X. Bu, G. Kehr and G. Erker, *Organometallics*, 2005, **24**, 4289-4297.
66. O. Baldovino-Pantaleón, S. Hernández-Ortega and D. Morales-Morales, *Advanced Synthesis & Catalysis*, 2006, **348**, 236-242.
67. W. Ye, M. Zhao, W. Du, Q. Jiang, K. Wu, P. Wu and Z. Yu, *Chemistry-A European Journal*, 2011, **17**, 4737-4741.
68. Q.-Q. Wang, R. A. Begum, V. W. Day and K. Bowman-James, *Journal of the American Chemical Society*, 2013, **135**, 17193-17199.
69. K. Ghosh, S. Kumar, R. Kumar and U. P. Singh, *Journal of Organometallic Chemistry*, 2014, **750**, 169-175.
70. P. J. Donoghue, J. Tehranchi, C. J. Cramer, R. Sarangi, E. I. Solomon and W. B. Tolman, *Journal of the American Chemical Society*, 2011, **133**, 17602-17605.
71. D. Huang, O. V. Makhlynets, L. L. Tan, S. C. Lee, E. V. Rybak-Akimova and R. H. Holm, *Inorganic Chemistry*, 2011, **50**, 10070-10081.
72. B. Bertrand and A. Casini, *Dalton Transactions*, 2014, **43**, 4209-4219.
73. Y. Gartia, P. Ramidi, D. E. Jones, S. Pulla and A. Ghosh, *Catalysis letters*, 2014, **144**, 507-515.
74. M. W. Johnson, A. G. DiPasquale, R. G. Bergman and F. D. Toste, *Organometallics*, 2014, **33**, 4169-4172.
75. M. Ray, D. Ghosh, Z. Shirin and R. Mukherjee, *Inorganic chemistry*, 1997, **36**, 3568-3572.
76. A. K. Singh, V. Balamurugan and R. Mukherjee, *Inorganic chemistry*, 2003, **42**, 6497-6502.
77. L. Fan, B. M. Foxman and O. V. Ozerov, *Organometallics*, 2004, **23**, 326-328.
78. J. Lapka, A. Paulenova, L. Zakharov, M. Y. Alyapyshev and V. Babain, *IOP Conference Series: Materials Science and Engineering*, 2010, **9**, 012029.
79. D. Dhar, G. M. Yee, A. D. Spaeth, D. W. Boyce, H. Zhang, B. Dereli, C. J. Cramer and W. B. Tolman, *Journal of the American Chemical Society*, 2016, **138**, 356-368.
80. T. Hirao, T. Moriuchi, T. Ishikawa, K. Nishimura, S. Mikami, Y. Ohshiro and I. Ikeda, *Journal of Molecular Catalysis A: Chemical*, 1996, **113**, 117-130.
81. S. L. Barnholtz, J. D. Lydon, G. Huang, M. Venkatesh, C. L. Barnes, A. R. Ketring and S. S. Jurisson, *Inorganic Chemistry*, 2001, **40**, 972-976.
82. R. V. Parish, B. P. Howe, J. P. Wright, J. Mack, R. G. Pritchard, R. G. Buckley, A. M. Elsome and S. P. Fricker, *Inorganic chemistry*, 1996, **35**, 1659-1666.
83. Todd C. Harrop, Laurie A. Tyler, Marilyn M. Olmstead and Pradip K. Mascharak, *European Journal of Inorganic Chemistry*, 2003, **2003**, 475-481.
84. C. Wallenhorst, K. V. Axenov, J. S. Samec, R. Fröhlich and G. Erker, *Zeitschrift für Naturforschung B*, 2007, **62**, 783-790.
85. M.A. Fox, J.K. Whitesell, Organische Chemie: Grundlagen, Mechanismen, Bioorganische Anwendungen. Spektrum Akad. Verlag,1995.
86. M. F. Graham J. Tizzard, Philip A. Gale, Mark E, 2016, DOI: 10.5517/ccdc.csd.cc1ljmnd.
87. A. Galanti, O. Kotova, S. Blasco, C. J. Johnson, R. D. Peacock, S. Mills, J. J. Boland, M. Albrecht and T. Gunnlaugsson, *Chemistry-a European journal*, 2016, **22**, 9709-9723.
88. W. Juan, H. Peng, H. Chao and Z. Bixue, *Chinese Journal of Applied Chemistry*, 2014, **32**, 284-291.
89. S.-K. Ko, S. K. Kim, A. Share, V. M. Lynch, J. Park, W. Namkung, W. Van Rossom, N. Busschaert, P. A. Gale and J. L. Sessler, *Nature chemistry*, 2014, **6**, 885.

90. N. W. Alcock, P. Moore, C. J. Reader and S. M. Roe, *Journal of the Chemical Society, Dalton Transactions*, 1988, 2959-2963.
91. B. Jia, Z.-Q. Hu, X.-T. Deng, C.-X. Cheng and S.-M. Shi, *Acta Crystallographica Section E: Structure Reports Online*, 2006, **62**, o4902-o4903.
92. M. G. Fisher, P. A. Gale and M. E. Light, *New Journal of Chemistry*, 2007, **31**, 1583-1584.
93. E. A. Katayev, G. D. Pantos, M. D. Reshetova, V. N. Khrustalev, V. M. Lynch, Y. A. Ustynyuk and J. L. Sessler, *Angewandte Chemie International Edition*, 2005, **44**, 7386-7390.
94. J. M. Baumes, I. Murgu, R. D. Connell, W. J. Culligan, A. G. Oliver and B. D. Smith, *Supramolecular Chemistry*, 2012, **24**, 14-22.
95. A. Casnati, N. Della Ca, M. Fontanella, F. Sansone, F. Ugozzoli, R. Ungaro, K. Liger and J. F. Dozol, *European journal of organic chemistry*, 2005, **2005**, 2338-2348.
96. J. C. Burley, *Acta Crystallographica Section B: Structural Science*, 2005, **61**, 710-716.
97. N. Adams, H. J. Arts, P. D. Bolton, D. Cowell, S. R. Dubberley, N. Friederichs, C. M. Grant, M. Kranenburg, A. J. Sealey and B. Wang, *Organometallics*, 2006, **25**, 3888-3903.
98. J. Zhang, S. Liu, A. Li, H. Ye and Z. Li, *New Journal of Chemistry*, 2016, **40**, 7027-7033.
99. M. a. P. Brandi-Blanco, D. Choquesillo-Lazarte, C. G. García-Collado, J. M. a. González-Pérez, A. Castiñeiras and J. Niclós-Gutiérrez, *Inorganic Chemistry Communications*, 2005, **8**, 231-234.
100. G. W. T. M. J. Frisch, H. B. Schlegel, G. E. Scuseria, M. A. Robb, J. R. Cheeseman, G. Scalmani, V. Barone, G. A. Petersson, H. Nakatsuji, X. Li, M. Caricato, A. Marenich, J. Bloino, B. G. Janesko, R. Gomperts, B. Mennucci, H. P. Hratchian, J. V. Ortiz, A. F. Izmaylov, J. L. Sonnenberg, D. Williams-Young, F. Ding, F. Lipparini, F. Egidi, J. Goings, B. Peng, A. Petrone, T. Henderson, D. Ranasinghe, V. G. Zakrzewski, J. Gao, N. Rega, G. Zheng, W. Liang, M. Hada, M. Ehara, K. Toyota, R. Fukuda, J. Hasegawa, M. Ishida, T. Nakajima, Y. Honda, O. Kitao, H. Nakai, T. Vreven, K. Throssell, J. A. Montgomery, Jr., J. E. Peralta, F. Ogliaro, M. Bearpark, J. J. Heyd, E. Brothers, K. N. Kudin, V. N. Staroverov, T. Keith, R. Kobayashi, J. Normand, K. Raghavachari, A. Rendell, J. C. Burant, S. S. Iyengar, J. Tomasi, M. Cossi, J. M. Millam, M. Klene, C. Adamo, R. Cammi, J. W. Ochterski, R. L. Martin, K. Morokuma, O. Farkas, J. B. Foresman, and D. J. Fox, Gaussian, Inc., Wallingford CT, 2016., *Gaussian, Inc., Wallingford CT, 2016.*, 2016.
101. O. Baldovino-Pantaleón, S. Hernández-Ortega and D. Morales-Morales, *Advanced Synthesis & Catalysis*, 2006, **348**, 236-242.
102. O. Baldovino-Pantaleón, S. Hernández-Ortega and D. Morales-Morales, *Inorganic Chemistry Communications*, 2005, **8**, 955-959.
103. C. Gunanathan and D. Milstein, *Chemical reviews*, 2014, **114**, 12024-12087.
104. R. G. Pearson, *Inorganic chemistry*, 1988, **27**, 734-740.
105. O. Q. Munro, S. D. Joubert and C. D. Grimmer, *Chemistry-A European Journal*, 2006, **12**, 7987-7999.
106. P. R. Rablen, S. A. Pearlman and D. A. Miller, *Journal of the American Chemical Society*, 1999, **121**, 227-237.
107. R. E. Carter and J. Sandstrom, *The Journal of Physical Chemistry*, 1972, **76**, 642-647.
108. T. Drakenberg, K. I. Dahlqvist and S. Forsen, *The Journal of Physical Chemistry*, 1972, **76**, 2178-2183.
109. C. R. Kemnitz and M. J. Loewen, *Journal of the American Chemical Society*, 2007, **129**, 2521-2528.
110. Y. K. Kang and H. S. Park, *Journal of Molecular Structure: THEOCHEM*, 2004, **676**, 171-176.

111. H. Zhang, J. Lee, A. D. Lammer, X. Chi, J. T. Brewster, V. M. Lynch, H. Li, Z. Zhang and J. L. Sessler, *Journal of the American Chemical Society*, 2016, **138**, 4573-4579.
112. O. Q. Munro, K. J. Akerman and P. Akerman, *Journal*, 2016.
113. R. Elder and J. Watkins, *Inorganic Chemistry*, 1986, **25**, 223-226.
114. K. Suntharalingam, D. Gupta, S. Miguel, J. Pablo, B. Lippert and R. Vilar, *Chemistry-A European Journal*, 2010, **16**, 3613-3616.
115. M. P. Suh, I. S. Kim, B. Y. Shim, D. Hong and T.-S. Yoon, *Inorganic Chemistry*, 1996, **35**, 3595-3598.
116. S. M. Godfrey, N. Ho, C. A. McAuliffe and R. G. Pritchard, *Angewandte Chemie International Edition*, 1996, **35**, 2344-2346.
117. R. Corbo, T. P. Pell, B. D. Stringer, C. F. Hogan, D. J. Wilson, P. J. Barnard and J. L. Dutton, *Journal of the American Chemical Society*, 2014, **136**, 12415-12421.
118. E. Makotchenko, E. Bykova, E. Y. Semitut, Y. V. Shubin, P. Snytnikov and P. Plyusnin, *Journal of Structural Chemistry*, 2011, **52**, 924-929.
119. E. Rabinovich, I. Goldberg and Z. Gross, *Chemistry-A European Journal*, 2011, **17**, 12294-12301.
120. S. O. Sommerer, C. E. MacBeth, A. J. Jircitano and K. A. Abboud, *Acta Crystallographica Section C: Crystal Structure Communications*, 1997, **53**, 1551-1553.
121. E. W. Wong, A. Miura, M. D. Wright, Q. He, C. J. Walsby, S. Shimizu, N. Kobayashi and D. B. Leznoff, *Chemistry-A European Journal*, 2012, **18**, 12404-12410.
122. T. Roth, H. Wadepohl and L. H. Gade, *European Journal of Inorganic Chemistry*, 2016, **2016**, 1184-1191.
123. W. T. Robinson and E. Sinn, *Journal of the Chemical Society, Dalton Transactions*, 1975, 726-731.
124. C. J. O'Connor and E. Sinn, *Inorganic Chemistry*, 1978, **17**, 2067-2071.
125. S. Karmakar, S. Chatterjee, K. Purkait and A. Mukherjee, *Dalton Transactions*, 2016, **45**, 11710-11722.
126. K. V. Luzyanin, M. Haukka, Y. A. Izotova, V. Y. Kukushkin and A. Pombeiro, *Acta Crystallographica Section E: Structure Reports Online*, 2005, **61**, m1765-m1767.
127. L. R. Gray, D. J. Gulliver, W. Levason and M. Webster, *Journal of the Chemical Society, Dalton Transactions*, 1983, 133-141.
128. R. Corbo, G. F. Ryan, M. A. Haghighatbin, C. F. Hogan, D. J. Wilson, M. D. Hulett, P. J. Barnard and J. L. Dutton, *Inorganic chemistry*, 2016, **55**, 2830-2839.
129. R. Dennington, T. Keith and J. Millam, *Semichem Inc., Shawnee Mission, KS*, 2009.
130. M. Frisch, G. Trucks, H. B. Schlegel, G. Scuseria, M. Robb, J. Cheeseman, G. Scalmani, V. Barone, B. Mennucci and G. Petersson, *Journal*, 2009.
131. D. A. Pantazis, X.-Y. Chen, C. R. Landis and F. Neese, *Journal of chemical theory and computation*, 2008, **4**, 908-919.
132. M. J. Frisch, J. A. Pople and J. S. Binkley, *The Journal of chemical physics*, 1984, **80**, 3265-3269.
133. T. A. Keith, *TK Gristmill Software, Overland Park KS, USA*, 2013.
134. A. Reed and F. Weinhold, *Chem. Phys*, 1983, **78**, 4066-4073.
135. M. O. Sinnokrot, E. F. Valeev and C. D. Sherrill, *Journal of the American Chemical Society*, 2002, **124**, 10887-10893.
136. E. W. Weisstein, 2007.
137. A. Bondi, *The Journal of physical chemistry*, 1964, **68**, 441-451.
138. S. Batsanov, *Zh. Fiz. Khim*, 2000, **74**, 1273-1276.
139. T. L. Brown, *Chemistry: the central science*, Pearson Education, 2009.
140. R. G. Parr and R. G. Pearson, *Journal of the American Chemical Society*, 1983, **105**, 7512-7516.
141. S. Batsanov, *Inorganic materials*, 2001, **37**, 871-885.
142. R. G. Pearson, *Proceedings of the National Academy of Sciences*, 1986, **83**, 8440-8441.

143. G. Marangoni, B. Pitteri, V. Bertolasi, G. Gilli and V. Ferretti, *Journal of the Chemical Society, Dalton Transactions*, 1986, 1941-1944.
144. J. Vicente, M. T. Chicote, M. D. Bermúdez, P. G. Jones, C. Fittschen and G. M. Sheldrick, *Journal of the Chemical Society, Dalton Transactions*, 1986, 2361-2366.
145. C.-W. Chan, W.-T. Wong and C.-M. Che, *Inorganic Chemistry*, 1994, **33**, 1266-1272.
146. Z. D. Hudson, C. D. Sanghvi, M. A. Rhine, J. J. Ng, S. D. Bunge, K. I. Hardcastle, M. R. Saadein, C. E. MacBeth and J. F. Eichler, *Dalton Transactions*, 2009, 7473-7480.
147. S. Chatterjee, J. A. Krause, K. Madduma-Liyanage and W. B. Connick, *Inorganic chemistry*, 2012, **51**, 4572-4587.
148. E. W. Ainscough, A. M. Brodie, A. K. Burrell, A. Derwahl, G. B. Jameson and S. K. Taylor, *Polyhedron*, 2004, **23**, 1159-1168.
149. L. Maresca and G. Natile, *Comments on Inorganic Chemistry*, 1993, **14**, 349-366.
150. F. P. Fanizzi, L. Maresca, C. Pacifico, G. Natile, M. Lanfranchi and A. Tiripicchio, *European journal of inorganic chemistry*, 1999, **1999**, 1351-1358.
151. M. Rimoldi, F. Ragaini, E. Gallo, F. Ferretti, P. Macchi and N. Casati, *Dalton transactions*, 2012, **41**, 3648-3658.
152. R. Garrone, A. M. Romano, R. Santi and R. Millini, *Organometallics*, 1998, **17**, 4519-4522.
153. S. Pratihar, J. Marek and S. Roy, *Inorganica Chimica Acta*, 2011, **372**, 362-366.
154. I. D. Hills and G. C. Fu, *Journal of the American Chemical Society*, 2004, **126**, 13178-13179.
155. A. Seyboldt, B. Wucher, S. Hohnstein, K. Eichele, F. Rominger, K. W. Törnroos and D. Kunz, *Organometallics*, 2015, **34**, 2717-2725.
156. C. Haasnoot, F. A. de Leeuw and C. Altona, *Tetrahedron*, 1980, **36**, 2783-2792.